THE IMPORTANCE OF THE ENTROPY INEQUALITY ON NUMERICAL SIMULATIONS USING REDUCED METHANE-AIR REACTION MECHANISMS

A Thesis

by

NATHAN HARLAN JONES

Submitted to the Office of Graduate Studies of
Texas A&M University
in partial fulfillment of the requirements for the degree of

MASTER OF SCIENCE

August 2012

Major Subject: Aerospace Engineering

THE IMPORTANCE OF THE ENTROPY INEQUALITY ON NUMERICAL SIMULATIONS USING REDUCED METHANE-AIR REACTION MECHANISMS

A Thesis

by

NATHAN HARLAN JONES

Submitted to the Office of Graduate Studies of
Texas A&M University
in partial fulfillment of the requirements for the degree of

MASTER OF SCIENCE

Approved by:

Chair of Committee,	Paul G. A. Cizmas
Committee Members,	Adonios Karpetis
	John Slattery
	Joseph Pasciak
Head of Department,	Dimitris C. Lagoudas

August 2012

Major Subject: Aerospace Engineering

ABSTRACT

The Importance of the Entropy Inequality on Numerical Simulations using Reduced Methane-Air Reaction Mechanisms. (August 2012)

Nathan Harlan Jones, B.S., Texas A&M University

Chair of Advisory Committee: Dr. Paul G. A. Cizmas

Many reaction mechanisms have been developed over the past few decades to predict flame characteristics. A detailed reaction mechanism can predict flame characteristics well, but at a high computational cost. The reason for reducing reaction mechanisms is to reduce the computational time needed to simulate a problem. The focus of this work is on the validity of reduced methane-air combustion mechanisms, particularly pertaining to satisfying the entropy inequality. While much of this work involves a two-step reaction mechanism developed by Dr. Charles Westbrook and Dr. Frederick Dryer, some consideration is given to the four-step and three-step mechanisms of Dr. Norbert Peters. These mechanisms are used to simulate the Flame A experiment from Sandia National Laboratories. The two-step mechanism of Westbrook and Dryer is found to generate results that violate the entropy inequality. Modifications are made to the two-step mechanism simulation in an effort to reduce these violations. Two new mechanisms, Mech 1 and Mech 2, are developed from the original two-step reaction mechanism by modifying the empirical data constants in the Arrhenius reaction form. The reaction exponents are set to the stoichiometric coefficients of the reaction, and the concentrations computed from a one-dimensional flame simulation are matched by changing the Arrhenius parameters. The new mechanisms match experimental data more closely than the original two-step mechanism

and result in a significant reduction in entropy inequality violations. The solution from Mech 1 had only 9 cells that violated the entropy inequality, while the original two-step mechanism of Westbrook and Dryer had 22,016 cells that violated the entropy inequality. The solution from Mech 2 did not have entropy inequality violations. The method used herein for developing the new mechanisms can be applied to more complex reaction mechanisms.

To Tara Lynn

ACKNOWLEDGMENTS

To begin, I would like to thank my advisor Dr. Paul Cizmas. Without his guidance the past two years I could not have accomplished the work in this thesis. He spends hours stretched between many graduate students, but his desire to make each and every one of us a better engineer is sincere. I would also like to thank my committee members, Drs. John Slattery, Adonios Karpetis, and Joseph Pasiack. The many discussions with Dr. Slattery aided me in the understanding needed to go forth with my research and accomplish goals previously thought unobtainable. Dr. Karpetis spent time helping me understand the problem from Sandia National Laboratory that I numerically simulated countless times.

I would also like to thank my family and friends, but most of all my loving wife Tara. She provided comfort at home, even with the varying states that I would come home in after a long day at the office. Without her love and hard work I could not have accomplished my goals these past few years. I would like to thank my parents for believing in me enough to help with funding my education here at Texas A&M. I know my time here has been a financial strain on my family, but I also believe that my time here has been priceless, and my parents understood that even when I didn't many years ago.

I must also thank my colleagues that have been extremely supportive during my time at A&M. As an undergaduate I met three amazing friends, Stephen Oehler, Danielle Fitch, and Jon Ellens. Stephen, Danielle and I went on to pursue our masters degree together. I would like to thank Stephen and Danielle for the countless lunch endeavors for a small retreat from our studies.

Last, but certainly not least, I must thank the colleagues that I have shared an office with while pursing my masters degree, Neil Matula and Brian Freno. I would

like to specifically thank Neil for willingly listening to my research problems and genuinely trying to help me find an answer.

TABLE OF CONTENTS

Page

CHAPTER Page

CHAPTER Page

LIST OF TABLES

LIST OF FIGURES

FIGURE Page

FIGURE Page

FIGURE Page

FIGURE Page

FIGURE Page

NOMENCLATURE

Roman Letters

A_r	Pre-exponentional factor
c_i	Concentration of species i
c_p	Specific heat capacity at constant pressure
$[CH_4]$	Concentration of CH_4
d_B	Mass transfer driving force
$\overline{\overline{D}}$	Rate of deformation tensor
D_{ij}	Binary diffusion coefficient
$D_{T,i}$	Soret thermal diffusion coefficient
E	Total energy
E_r	Activation energy
$\vec{F}$	external body forces
F_i^c	Diffusion flux for one-dimensional equations in HCT
F^ϵ	Enthalpy lost by diffusion
$\vec{g}$	Gravitational acceleration
h	Enthalpy
h_i^0	Enthalpy of formation
$\overline{\overline{I}}$	Identity tensor
$\vec{J}_i$	Diffusive mass flux vector
k_b	Backward rate constant
k_{eff}	Effective thermal conductivity
k_f	Forward rate constant
K_r	Equilibrium constant
m	Mass

M	Molecular weight
M_w	Mean molecular weight
$\mathcal{M}_i$	Symbol denoting species i
p	Pressure
Q	Viscosity term
Δr_j	Width of zone j in one-dimensional HCT simulation
R	Universal gas constant
R_i	Net rate of reaction
$\hat{R}_{i,r}$	Molar rate of creation/destruction of species i in reaction r
S_h	Source term in energy equation
S_i	Source term in species equation
S_i^0	Standard-state entropy
S_L	Flame speed
t	Time
T	Temperature
T^*	Dimensionless temperature
$\vec{v}$	Velocity
X	Mole fraction
δy	Non-dimensional correction term
Y	Mass fraction

Greek Letters

β	Arrhenius temperature exponent
γ	Third body efficiency

Γ	Third body effect
ϵ	Internal energy
ϵ/k_B	Lennard Jones parameter
η_i'	Rate exponent for reactant i
η_i''	Rate exponent for product i
λ	Bulk viscosty
μ	Dynamic viscosity
μ_B	Chemical potential
ν_i'	Stoichiometric coefficient of reactant i
ν_i''	Stoichiometric coefficient of product i
ρ	Density
σ_i	Lennard Jones parameter
$\overline{\overline{\tau}}$	Stress tensor
ϕ	Equivalence ratio
ω_r	Rate of progress or reaction r
$\Omega_{\mu i}$	Dimensionless collision integral

CHAPTER I

INTRODUCTION

1.1 Motivation

1.1.1 Computational Fluid Dynamics

Computational fluid dynamics (CFD) is an approach to analyze fluid flow problems by numerically solving the conservation of mass, momentum and energy equations. Research in aerodynamics using CFD has led to advances in power systems by providing the designer with knowledge of the flow field through turbines and turbo pumps [3]-[6]. CFD offers designers the ability to test many configurations before fabricating the system. This approach saves time and money during the development of a new design. Additionally, the designer can investigate power systems that have been in use for decades and suggest modifications to increase the efficiency and decrease the emissions of the system. These reasons make CFD an attractive tool. This work focuses on CFD of combustive flows, and aims to shed light on reduced reaction mechanisms and how they effect a simulation.

1.1.2 Methane Fuel

In propulsion, methane is an attractive fuel because it is readily available and much easier to store than liquid hydrogen. Many companies are looking into natural gas as a fuel option for space purposes. NASA is currently working on a lunar lander called Morpheus that is powered by a methane-oxygen fueled engine [7]. Methane is the simplest hydrocarbon, and thus, produces the least amount of heat upon combustion,

---

This thesis follows the style of the *Journal of Computational Physics*.

but methane has the best heat release per mass compared to any other hydrocarbon. Behind hydrogen, methane is the best choice as a fuel based on energy densities [8].

Methane is used currently as a fuel for generating electricity in gas turbines. It is also pumped into homes for heating and cooking. Natural gas is composed of mostly methane, and is considered the most environmentally friendly fuel because it releases less carbon dioxide than other hydrocarbons. This interest has motivated the development of reduced mechanisms to predict the flame characteristics of methane-air combustion.

1.1.3 Chemical Reaction Mechanisms

Detailed reaction mechanisms exist that can predict flame characteristics extremely well, but are computationally expensive. The GRI-Mech 3.0 mechanism has 325 reactions, 53 species, and has proven to be a very capable mechanism for simulating methane combustion [9]. The purpose of reducing these mechanisms is to decrease the number of species, and thus, reduce the computational time required for simulation. The reduction process includes neglecting faster reactions, setting steady state approximations for species, and partial equilibrium considerations. This process consistently disregards the second law of thermodynamics (or the entropy inequality). The work herein applies the entropy inequality to the resulting steady flame solutions of these reduced mechanisms, and proves that this consistent neglect of the inequality leads to nonphysical results.

1.2 Reduced Chemical Reaction Mechanisms of Methane Combustion: Literature Review

1.2.1 Five and Six-Step Methane Combustion Mechanisms

Many reduced chemical reaction mechanisms of methane have been developed over the years. This section will quickly highlight a few of these mechanisms and the purpose for which they are derived. The first mechanisms come from Seshadri, who has completed extensive work on the asymptotic structure of methane-air flames. His work is divided into two parts: the structure of lean and near stoichiometric flames [10], [11] and that of rich methane-air flames [12]. Seshadri utilizes a five-step mechanism for his lean and near stoichiometric analysis, and turns to a six-step mechanism for the rich methane-air flames. His research has led to an understanding of the structure of methane-air flames against the entire range of equivalence ratios for which methane burns. Peters also contributed to the understanding of the structure of methane-air flames with his work on stoichiometric flames [13].

1.2.2 Three and Four-Step Methane Combustion Mechanisms

Peters has completed extensive work with the four-step mechanism that he reduced from a skeletal mechanism. The skeletal mechanism can be found in Smooke's compilation of reduced kinetic mechanisms [14]. Additionally, the derivation of the four-step mechanism is outlined in detail in chapter IV. Peters has used the four-step mechanism to analyze stretched laminar methane-air diffusion flames, and reports that the mechanism can accurately predict the flame structure as well as the flammability limits of methane-air diffusion flames. Other authors have utilized Peters' four-step mechanism to conduct research on methane-air combustion. Seshadri has used this mechanism to analyze the asymptotic structure of premixed methane-air flames. The

mechanism predicts flame speeds of mixtures with atmospheric pressure and room temperature that are similar to those reported in experiments, and detailed reaction mechanisms [15]. Work has also been conducted for nonpremixed flames, with the result that the four-step mechanism predicts the laminar flame structure and gives a good prediction of extinction [16]. Peters four-step mechanism can be reduced to a three-step mechanism that is sufficient for high pressures, above 1 atm [13]. This mechanism has also been shown to predict the structure of stoichiometric methane-air flames.

1.2.3 Global and Two-Step Methane Combustion Mechanisms

Westbrook and Dryer have reported a simple method for producing reaction mechanisms for hydrocarbon fuels. The method is to vary certain Arrhenius parameters in the reaction rate equation to match the methane-air flame speed at stoichiometric conditions [1]. They developed this procedure after studying the dependence of flame speed on parameters such as pressure, equivalence ratio, and unburned fuel temperature [17]. Their objective was to find a reaction rate equation that produces the correct flame speed in the limits of flammability of methane-air. They matched the flame speed at an equivalence ratio of one, and then ran simulations in a one-dimensional flame code at different values of equivalence ratio and compared the results with those of a detailed reaction mechanism. Westbrook and Dryer reported four global methane reaction mechanisms. They were able to develop two global mechanisms that predicted the flame speed well. They continued further to show how to add the oxidation of carbon monoxide to produce a two-step mechanism. This two-step mechanism is the focus of much of the work reported in this thesis. Westbrook and Dryer's method is unique because it can be used to create simple reaction mechanisms for any hydrocarbon fuel.

1.3 Novel Aspects of this Thesis

This thesis presents a new approach to developing reduced reaction mechanisms. The work herein focuses on methane-air reaction mechanisms, but the approach can be extended to other hydrocarbon fuels. The procedure uses a detailed reaction mechanism to predict the concentrations of the major species of a laminar flame. These concentrations are then matched by the reduced reaction mechanism as closely as possible. Conditions are set during the matching procedure to ensure the reduced mechanism produces results that satisfy the entropy inequality, therefore abiding by the second law of thermodynamics. To the knowledge of the author, this is the first time a methodology has been presented that develops reduced reaction mechanisms to satisfy the entropy inequality.

CHAPTER II

GOVERNING TRANSPORT EQUATIONS

This chapter provides the governing equations used to model chemically reacting flows. The first part of this chapter reviews the conservation of mass, momentum and energy equations. The second part presents the multicomponent species transport model and the reaction rate equations.

2.1 Equations for Basic Fluid Flow

This section introduces the basic equations for fluid flow, including the continuity, momentum and energy conservation equations.

2.1.1 Continuity Equation

The continuity equation, or mass conservation equation for a basic fluid flow is

$$\frac{\partial \rho}{\partial t} + \nabla \cdot (\rho \vec{v}) = 0, \tag{2.1}$$

where ρ is the density and $\vec{v}$ is the velocity of the fluid. This form of the mass conservation equation is valid for both incompressible and compressible flows [18, sec. 8.2]. This form assumes there are no mass generation source terms.

2.1.2 Momentum Equations

The conservation of momentum equation for general fluid flow is written as

$$\frac{\partial}{\partial t}(\rho \vec{v}) + \nabla \cdot (\rho \vec{v}\vec{v}) = -\nabla p + \nabla \cdot (\overline{\overline{\tau}}) + \rho \vec{g} + \vec{F}, \tag{2.2}$$

where p is the static pressure of the flow, $\overline{\overline{\tau}}$ is the stress tensor, $\vec{g}$ is the gravitational acceleration, and $\vec{F}$ is the external body forces. The stress tensor is defined as

$$\overline{\overline{\tau}} = \mu \left[(\nabla \vec{v} + \nabla \vec{v}^T) - \frac{2}{3} \nabla \cdot \vec{v} \overline{\overline{I}} \right],$$

where μ is the dynamic viscosity and $\overline{\overline{I}}$ is the identity tensor. The dynamic viscosity for combustive flows is computed from kinetic theory. The equation for calculating μ is a summation of contributions from each species and is written as

$$\mu = \sum_i \frac{X_i \mu_i}{\sum_j X_j \phi_{ij}},$$

where X_i is the mole fraction of species i, and ϕ_{ij} is an intermediate quantity defined as

$$\phi_{ij} = \frac{\left[1 + (\frac{\mu_i}{\mu_j})^{\frac{1}{2}} (\frac{M_j}{M_i})^{\frac{1}{4}} \right]^2}{\left[8(1 + \frac{M_i}{M_j}) \right]^{\frac{1}{2}}}.$$

Here, M_i is the molecular weight of species i and μ_i is the dynamic viscosity of species i, computed from [18, sec. 7.3.3]

$$\mu_i = 2.67 \times 10^{-6} \frac{\sqrt{M_i T}}{\sigma_i^2 \Omega_{\mu i}},$$

where T is temperature, σ_i is the collision diameter of species i, in units of Ängstroms, $\Omega_{\mu i}$ is a function of a dimensionless temperature, T^*, and is commonly referred to as the dimensionless collision integral [19, p. 656]. The empirical expression for $\Omega_{\mu i}$ is

$$\Omega_{\mu i} = [A(T^*)^{-B}] + C[e^{-DT^*}] + E[e^{-FT^*}],$$

with

$$T^* = \frac{T}{(\epsilon / k_B)_i},$$

and

$$A = 1.16145 \qquad D = 0.77320$$
$$B = 0.14874 \qquad E = 2.16178,$$
$$C = 0.52487 \qquad F = 2.43787$$

and is only valid for $0.3 \leq T^* \leq 100$ [20, sec. 9.5]. The inputs to the kinetic theory calculation σ_i and $(\epsilon/k_B)_i$ are tabulated for each species in the literature [20, p. B.1], and are referred to as the Lennard Jones parameters. These Lennard Jones parameters have also been tabulated by NASA and are reported in [21, p. 20].

2.1.3 Energy Equation

The energy equation is important when simulating reacting flows because the changes in temperature are significant. The contents of the energy equation are introduced assuming the multicomponent species model is used. The multicomponent model will be introduced later in this chapter, and is used for all simulations conducted in this work.

The conservation of energy equation is written as

$$\frac{\partial}{\partial t}(\rho E) + \nabla \cdot (\vec{v}(\rho E + p)) = \nabla \cdot \left(k_{eff} \nabla T - \sum_i h_i \vec{J_i} + (\overline{\overline{\tau}}_{eff} \cdot \vec{v}) \right) + S_h, \qquad (2.3)$$

where $\vec{J_i}$ is the diffusion mass flux vector of species i, which will be discussed more thoroughly in the multicomponent model section. The term with $\vec{J_i}$ is the energy due to diffusion. k_{eff} is the effective head conductivity, and the term with k_{eff} is the energy due to conduction. The last term in the parenthesis on the right hand side represents the energy due to viscous dissipation. The total energy, E, is computed

from

$$E = h - \frac{p}{\rho} + \frac{v^2}{2},$$

where h is the enthalpy of the flow. The enthalpy is expressed as a sum of the contributions from each species as

$$h = \sum_i Y_i h_i,$$

where Y_i is the mass fraction of species i, and h_i is the enthalpy of each species i, expressed as

$$h_i = \int_{T_{ref}}^{T} c_{p,i} \mathrm{d}T.$$

The reference temperature, T_{ref}, is generally chosen as 298 K. The specific heat capacity, c_p, for each species i is calculated from the piecewise polynomial expression

$$c_p(T) = \alpha_1 + \alpha_2 T + \alpha_3 T^2 + \alpha_4 T^3 + \alpha_5 T^4. \tag{2.4}$$

The coefficients are different for each species and are tabulated in [22], [23]. The polynomial expression is usually split into at least two intervals, generally $300\text{K} \leq T \leq 1000\text{K}$ and $1000\text{K} \leq T \leq 5000\text{K}$. There are many sources where these polynomials can be found, and one should express caution when changing sources. The units must be consistent and some polynomials are not the same basic power law form as (2.4).

The source term of (2.3) is expressed as

$$S_h = -\sum_i \left(\frac{h_i^0}{M_i} + \int_{T_{ref,i}}^{T} c_{p,i} \mathrm{d}T \right) R_i,$$

where R_i is the net rate of production of species i due to each chemical reaction where species i is present. This rate of production term will be covered in more detail in the following section. The enthalpy of formation, h_i^0, is the total change in enthalpy

that accompanies the formation of one mole of species i.

2.2 Reacting Flows Transport Equations

In addition to the basic flow equations of continuity, momentum and energy conservation, species transport equations are necessary for simulating chemically reacting flows. This section presents an overview of the species transport equation, along with the multicomponent model and the empirical reaction rate equations.

2.2.1 Species Transport Equation

The conservation equations are solved for chemical species by predicting the local mass fraction of each species through the solution of a convective-diffusion equation [18, sec. 13.1.1]. The conservation equation is written as

$$\frac{\partial}{\partial t}(\rho Y_i) + \nabla \cdot (\rho \vec{v} Y_i) = -\nabla \vec{J}_i + R_i + S_i, \tag{2.5}$$

where S_i is a source term used for user-defined sources, such as adding energy to the flow to increase temperature. A common use for this source term is for ignition. For N species, (2.5) will be solved for $N-1$ unknowns. The sum of the mass fractions, Y_i, must be equal to one, therefore, the Nth species mass fraction will be determined as one minus the sum of the $N-1$ mass fractions. Typically, the Nth species is the one with the largest mass fraction to minimize numerical error [18, sec. 13.1.1]. For this work N_2 is the Nth species, because the oxidizer is air. As mentioned before, the mass diffusion flux vector, $\vec{J}_i$, is determined from the multicomponent species transport model, and will be discussed in detail in the following section.

2.2.2 Multicomponent Species Transport

For diffusion dominated laminar flows, the treatment of the species diffusion in the transport equations becomes important. The Maxwell-Stefan equations are used to obtain the diffusive mass flux vector, which is preferred over computing the multicomponent diffusion coefficients [18, sec. 13.1.1].

After manipulating the Maxwell-Stefan equations, one can write the diffusive mass flux vector as [24, p. 89]

$$\vec{J_i} = -\sum_{j=1}^{N-1} \rho D_{ij} \nabla Y_j - D_{T,i} \frac{\nabla T}{T}. \tag{2.6}$$

Along with the definitions [18, sec. 13.1.1]

$$D_{ij} = [D] = [A]^{-1}[B],$$

$$A_{ii} = -\left(\frac{X_i}{D_{iN}} \frac{M_w}{M_N} + \sum_{\substack{j=1 \\ j \neq i}}^{N} \frac{X_j}{D_{ij}} \frac{M_w}{M_i} \right),$$

$$A_{ij} = X_i \left(\frac{1}{D_{ij}} \frac{M_w}{M_j} - \frac{1}{D_{iN}} \frac{M_w}{M_N} \right),$$

$$B_{ii} = -\left(X_i \frac{M_w}{M_N} + (1 - X_i) \frac{M_w}{M_i} \right),$$

and

$$B_{ij} = X_i \left(\frac{M_w}{M_j} - \frac{M_w}{M_N} \right),$$

where D_{ij} is the binary diffusion coefficient, $[A]$ $[B]$ and $[D]$ are $(N-1)\times(N-1)$ sized matrices, and $[D]$ is a matrix of the generalized Fick's law of diffusion coefficients [18,

sec. 13.1.1]. The mean molecular weight of the mixture, M_w, is a summation of the contributions of each species, and is computed from

$$M_w = \sum_{i=1}^{N} M_i X_i.$$

The species mole fraction, X_i, can be related to the species mass fraction, Y_i, using the mean molecular weight and the molecular weight of each individual species [25, p. 19].

$$X_i = \frac{Y_i M_w}{M_i}.$$

The thermal diffusion coefficient defined as

$$D_{T,i} = -2.59 \times 10^{-7} T^{0.659} \left[\frac{M_i^{0.511} X_i}{\sum_{i=1}^{N} M_i^{0.511} X_i} - Y_i \right] \cdot \left[\frac{\sum_{i=1}^{N} M_i^{0.511} X_i}{\sum_{i=1}^{N} M_i^{0.489} X_i} \right] \tag{2.7}$$

is a form of the Soret Diffusion coefficient that causes heavy molecules to diffuse less rapidly, and light molecules to diffuse more rapidly toward heated surfaces [18, sec. 13.1.1]. This is accomplished by using the molecular weights of the species inside the empirically derived formula. The ratios inside the brackets of (2.7) are what distinguishes the heavy and light molecules and how rapid they diffuse.

In this work the effect of the Soret form of the diffusion coefficient is investigated by running separate simulations with and without the Soret diffusion term. The results are compared by investigating the change in temperature and methane mass fraction throughout the domain. This diffusion calculation is valid for laminar flows, and is sufficient for the work presented in this thesis. The reacting flows simulated here are laminar methane-air flames, therefore, a turbulent diffusion coefficient does not apply.

2.2.3 Reaction Rate Equations

The rate of reaction, R_i, in (2.5) can be computed by using one of three models: laminar finite-rate model, eddy-dissipation model, or the eddy-dissipation-concept model [18, sec. 13.1.1]. In the eddy-dissipation model, the reaction rates are assumed to be controlled by turbulence, so the Arrhenius rate equations can be avoided. This model is cheap computationally, but seldom yields realistic results. The eddy-dissipation-concept model uses detailed Arrhenius chemical kinetics with turbulent flames, but these detailed calculations are computationally expensive [18, sec. 13.1.1]. The laminar finite-rate model is used for this work and discussed in detail throughout this section.

In the laminar finite-rate model the reaction rates are calculated from Arrhenius rate expressions, and the effect of turbulent fluctuations are ignored. This model is exact for laminar flames but is generally not accurate for turbulent flames [18, sec. 13.1.1]. Once again, the laminar model is sufficient for the work in this thesis. The net rate of reaction for each species i is calculated as the sum of the Arrhenius reaction sources for each reaction that the species is present. The net rate of reaction is defined as

$$R_i = M_i \sum_{r=1}^{N_r} \hat{R}_{i,r}, \tag{2.8}$$

where N_R is the number of reactions and $\hat{R}_{i,r}$ is the molar rate of creation/destruction of species i in reaction r, computed from the Arrhenius rate expression. The general expression for the rth reaction is

$$\sum_{i=1}^{N} \nu'_{i,r} \mathcal{M}_i \rightleftharpoons \sum_{i=1}^{N} \nu''_{i,r} \mathcal{M}_i,$$

where

$$N = \text{number of chemical species in the system}$$
$$\nu'_{i,r} = \text{stoichiometric coefficient of reactant } i \text{ in reaction } r$$
$$\nu''_{i,r} = \text{stoichiometric coefficient of product } i \text{ in reaction } r$$
$$\mathcal{M}_i = \text{symbol denoting species } i.$$

The summations go through all the species, but only those with nonzero stoichiometric coefficients will show up on each side of the reaction. This notation is demonstrated by the global methane-oxygen reaction equation

$$\mathrm{CH_4} + 2\ \mathrm{O_2} \rightarrow \mathrm{CO_2} + 2\ \mathrm{H_2O}.$$

For this reaction the variables described above are defined as

$$\mathcal{M}_1 = \mathrm{CH_4} \quad \nu'_{1,1} = 1 \quad \nu''_{1,1} = 0$$
$$\mathcal{M}_2 = \quad \mathrm{O_2} \quad \nu'_{2,1} = 2 \quad \nu''_{2,1} = 0$$
$$\mathcal{M}_3 = \mathrm{CO_2} \quad \nu'_{3,1} = 0 \quad \nu''_{3,1} = 1$$
$$\mathcal{M}_4 = \mathrm{H_2O} \quad \nu'_{4,1} = 0 \quad \nu''_{4,1} = 2.$$

The molar rate of creation/destruction, $\hat{R}_{i,r}$, in (2.8) is computed from

$$\hat{R}_{i,r} = \Gamma \left(\nu''_{i,r} - \nu'_{i,r}\right) \left(k_{f,r} \prod_{j=1}^{N_r} [C_{j,r}]^{\eta'_{j,r}} - k_{b,r} \prod_{j=1}^{N_r} [C_{j,r}]^{\eta''_{j,r}} \right), \tag{2.9}$$

where

N_r = number of chemical species in reaction r

$C_{j,r}$ = molar concentration of each reactant and product species j in reaction r [kgmol/m^3]

$\eta'_{j,r}$ = forward rate exponent for each reactant and product species j in reaction r

$\eta''_{j,r}$ = backward rate exponent for each reactant and product species j in reaction r

$k_{f,r}$ = forward rate constant for reaction r

$k_{b,r}$ = backward rate constant for reaction r.

The variable Γ represents the effect of third bodies on the reaction rate, and is found by summing the contributions from each species, written as

$$\Gamma = \sum_{j}^{N_r} \gamma_{j,r} C_j.$$

For third body reactions each species is given a third body efficiency, $\gamma_{j,r}$ that governs how that species effects the reaction rate. The forward rate constant, $k_{f,r}$, is found using the Arrhenius expression

$$k_{f,r} = A_r T^{\beta_r} \exp -E_r/RT,$$

where

$$A_r = \text{pre-exponential factor [consistent units]}$$

$$\beta_r = \text{temperature exponent}$$

$$E_r = \text{activation energy for the reaction [J/kgmol]}$$

$$R = \text{universal gas constant [J/kgmol-K].}$$

The backward rate is defined as

$$k_{b,r} = \frac{k_{f,r}}{K_r},$$

where K_r is referred to as the equilibrium constant of the rth reaction, calculated from

$$K_r = \exp\left(\frac{\Delta S_r^0}{R} - \frac{\Delta H_r^0}{RT}\right)\left(\frac{p_{atm}}{RT}\right)^{\sum_{r=1}^{N_R}(\nu''_{j,r}-\nu'_{j,r})}. \tag{2.10}$$

The expression inside the exponential function in (2.10) represents the change in Gibbs free energy and can be computed with

$$\frac{\Delta S_r^0}{R} = \sum_{i=1}^{N}\left(\nu''_{i,r} - \nu'_{i,r}\right)\frac{S_i^0}{R},$$

and

$$\frac{\Delta H_r^0}{R} = \sum_{i=1}^{N}\left(\nu''_{i,r} - \nu'_{i,r}\right)\frac{h_i^0}{R},$$

where S_i^0 and h_i^0 are the standard-state entropy and standard state enthalpy.

2.3 Summary

The conservation of mass (2.1), momentum (2.2) and energy (2.3) equations have been presented. Additionally, the species conservation equation (2.5) and the reaction rate equations required to simulate chemically reacting flow have also been introduced. The multicomponent model is used to calculate the diffusive mass flux vector. These equations are used to solve the laminar methane-air flames simulated in the work herein.

CHAPTER III

FLAME SPEED CODES

This chapter presents an overview of two one-dimensional flame codes. These codes solve a one-dimensional steady flame and determine the flame speed of the mixture. The first code presented is purely a one-dimensional code used for calculating flame speed called HCT. The second code is Cantera which has many capabilities, including calculating the flame speed of a one-dimensional propagating flame.

3.1 HCT

HCT is a flame code developed at Lawrence Livermore Laboratory that calculates time-dependent phenomena involving one dimensional hydrodynamics, transport and detailed chemical kinetics [26, p. 1]. The following sections introduce the governing equations and solution technique used by HCT.

3.1.1 Governing Equations

The governing equations used by HCT are the species conservation equation, a momentum conservation equation, the energy conservation equation and an equation governing the change in node positioning. The following section describes the discretization of the governing equations.

The species conservation equation is [26, p. 9]

$$\frac{D}{Dt}C_i = -C_i\frac{\partial}{\partial x}v + \sum_k R_{i,k} - \frac{\partial}{\partial x}F_i^c, \tag{3.1}$$

with

$$\frac{D}{Dt} = \frac{\partial}{\partial t} + v\frac{\partial}{\partial x},$$

where c_i is the concentration of species i, v is the velocity, $R_{i,k}$ is the rate of production of species i due to reaction k, and F_i^c is the diffusion flux of species i. The diffusion flux is written as

$$F_i^c = -\rho D_i \frac{\partial}{\partial x}\left(\frac{C_i}{\rho}\right),$$

where ρ is the density and D_i is the diffusion coefficient of species i. The momentum conservation equation is written as [26, p. 9]

$$\frac{D}{Dt}v = -\frac{1}{\rho}\frac{\partial}{\partial x}(p + Q), \tag{3.2}$$

where p is pressure and Q is a viscosity term that can be real or artificial and is found not to be important for the purposes of this work [26, p. 6]. The viscosity term Q is given by

$$Q = -\lambda\frac{\partial}{\partial x}v,$$

with

$$\lambda = -\frac{2}{3}\mu,$$

where μ is the shear viscosity.

The conservation of energy is written for the internal energy ε as [26, p. 10]

$$\frac{D}{Dt}\varepsilon = [\varepsilon + (p + Q)]\frac{\partial}{\partial x}v - \frac{\partial}{\partial x}F^{\varepsilon}, \tag{3.3}$$

where F^{ε} is the enthalpy lost by diffusion. The equation for F^{ε} is written as

$$F^{\varepsilon} = \sum_{i} h_i F_i^c - \alpha^T c_p \frac{\partial}{\partial x} T,$$

where T is the temperature, α^T is the thermal diffusion coefficient and c_p is the specific heat capacity at constant pressure. The equation governing the change in the width of each cell (or zone) is defined as [26, p. 8]

$$\frac{\Delta r}{\Delta r'} = 1 - \Delta t \frac{\partial}{\partial x} v', \tag{3.4}$$

where Δr is the width of the zone and the primed quantities are evaluated at the next time-step.

3.1.2 One-Dimensional Discretized Equations

In the HCT manual [26, pp. 3-7] the difference equations, instead of the differential equations, are introduced to describe the solution process. The cells, or zones, are described by their thickness Δr_j. Imagine the domain is a line that is discretized by points. The length between these points is Δr_j, as shown in Fig. 1. For this

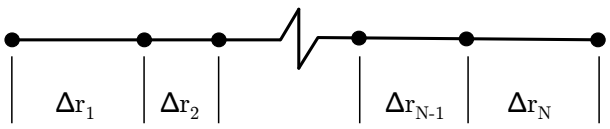

Figure 1. Computational grid: Δr_j is the width of zone j

representation, the velocity of the boundary between zone j and $j-1$ is denoted as $v_{j-1/2}$. The concentrations of each species i in zone j is $C_{i,j}$. The state of zone j at

time t is known if $c_{i,j}$, T_j, Δr_j and $v_{j-1/2}$ are all known. With these definitions, the following equations can be formulated. In the following, primed quantities denote the quantity is evaluated at the next time $t + \Delta t$, and quantities that are evaluated at the current time are left without superscripts.

The conservation of species yields the difference equation [26, p. 4]

$$C'_{i,j} - \frac{\Delta r_j}{\Delta r'_j} C_{i,j} = \sum_k \Delta t R'_{i,j,k} - \frac{\Delta t}{\Delta r'_j}(F^{c'}_{i,j+1/2} - F^{c'}_{i,j-1/2}), \tag{3.5}$$

where $R'_{i,j,k}$ is the effect of reaction k on species i in zone j. This term has the Arrhenius expression described on page 14. $F^{c'}_{i,j-1/2}$ is the diffusion flux of species i through zone boundary $j - 1/2$, and is given by

$$F^{c'}_{i,j-1/2} = -(\rho D_i)_{j-1/2} \frac{1}{\Delta r'_{j-1/2}} \left(\frac{C'_{i,j}}{\rho_j} - \frac{C'_{i,j-1}}{\rho'_{j-1}} \right).$$

The boundary-centered value $\Delta r'_{j-1/2}$ is given by

$$\Delta r'_{j-1/2} = \frac{1}{2} \left[\Delta r'_{j-1} + \Delta r'_j \right],$$

and $(\rho D_i)_{j-1/2}$ is given by

$$(\rho D_i)_{j-1/2} = \frac{1}{2} \left[(\rho D_i)_{j-1} + (\rho D_i)_j \right].$$

D_i has a simple power law dependence on the total species concentration C_{tot} and T [26, p. 5], defined as

$$D_i = D_i^0 T^\alpha C_{tot}^\beta.$$

The second difference equation introduced is Newton's second law written for the boundary velocities as [26, p. 5]

$$m_{j-1/2}(v'_{j-1/2} - v_{j-1/2}) = -\Delta t \left[(p + Q)'_{j+1} - (p + Q)'_j \right]. \tag{3.6}$$

$m_{j-1/2}$ is the average of the masses in zone j and $j-1$, written as

$$m_{j-1/2} = \frac{1}{2}\left[\Delta r_{j-1}\sum_i M_i C_{i,j-1} + \Delta r_j \sum_i M_i C_{i,j}\right].$$

p_j is the pressure in zone j and is found using the ideal gas law, resulting in

$$p_j = \sum_i C_{i,j} RT.$$

Q_j is a viscosity term that can be either real or artificial, and is found to not be important for the purposes of this work. Refer to the HCT manual [26, p. 6] for further explanation.

The third equation is the conservation of energy for each zone, written as [26, p. 6]

$$\left[\Delta r'_j \epsilon'_j - \Delta r_j \epsilon_j\right] + (p+Q)'_j[\Delta r'_j - \Delta r_j] = -\Delta t\left[F^{\epsilon'}_{j+1/2} - F^{\epsilon'}_{j-1/2}\right]. \tag{3.7}$$

ϵ_j is the internal energy in zone j, and is found by summing the contributions from the energies of each species ε_i, defined as

$$\epsilon_j = \sum_i C_{i,j}\varepsilon_i.$$

HCT uses fifth-order polynomial fits in T to the JANAF data [27] for c_p^i [26, p. 7]. This polynomial is similar to the formulation on page 9. The internal energy for each species is computed as

$$\varepsilon_i = \Delta H_0^i + \int_{T_0} c_p^i \mathrm{d}T - RT,$$

where ΔH_0^i is the enthalpy at T_0. The second term on the left hand side of (3.7) represents the PdV work, while the right side represents the enthalpy lost by diffusion [26, p. 7]. This diffusion term has two contributions, the enthalpy carried by species

diffusion and the thermal conduction contribution [26, p. 7]. These contributions are split up into

$$F^{\epsilon'}_{j-1/2} = F^{T'}_{j-1/2} + F^{H'}_{j-1/2},$$

with

$$F^{T'}_{j-1/2} = -(\alpha^T c_p)_{j-1/2} \frac{1}{\Delta r'_{j-1/2}} (T'_j - T'_{j-1}),$$

$$(\alpha^T c_p)_{j-1/2} = \frac{1}{2}\left[(\alpha^T c_p)_{j-1} + (\alpha^T c_p)_j\right],$$

$$c_p = \sum_i C_i c^i_p,$$

$$F^{H'}_{j-1/2} = \sum_i h'_{i,j-1/2} F^{c'}_{i,j-1/2},$$

and

$$h'_{i,j-1/2} = \frac{1}{2}(h'_{i,j-1} + h'_{i,j}).$$

The thermal diffusion coefficient α^T is also given as power law dependence similar to D_i.

The final equation needed determines the change in the location of the nodes, Δr_j, and is written as [26, p. 8]

$$\Delta r'_j = \Delta r_j + \Delta t \left(v'_{j+1/2} - v'_{j-1/2}\right). \tag{3.8}$$

3.1.3 Solution Technique

For N species there are $N + 3$ equations to solve: N species conservation equations (3.5), Newton's second law (3.6), the energy equation (3.7), and the equation for the grid spacing (3.8). The unknowns are the species concentrations $c_{i,j}$, the temperature of each zone T_j, the zone spacing Δr_j and the boundary velocity $v_{j-1/2}$. The solution technique utilizes a general vector form.

For each zone j define a vector $\vec{x}_j$ with $N+3$ components. The first N components are the species concentrations $c_{i,j}$, followed by T_j, Δr_j and $v_{j-1/2}$. For the equations let us define for each zone a vector $\vec{f}_j$. The first N components of $\vec{f}_j$ are the species conservation equations, followed by the energy equation, the grid spacing equation and Newton's second law. The right hand sides of each equation are subtracted from the left sides, and the equations are written in vector notation as

$$\vec{f}'_j = 0. \tag{3.9}$$

Each component of $\vec{f}'_j$ is a function of $\vec{x}'_j$, as well as the neighboring zones $j - 1$ and $j + 1$. Therefore, (3.9) can be written as

$$\vec{f}'_j(\vec{x}'_{j-1}, \vec{x}'_j, \vec{x}'_{j+1}) = 0.$$

This is solved using a modified Newton's iteration scheme. The relative correction $\delta\vec{y}_j$ is defined as

$$\delta\vec{y}_j = \frac{\delta\vec{x}_j}{\vec{x}_j}.$$

The relative correction is solved for in the modified Newton scheme. The advantage

to this method is that $\vec{y}_j$ is a dimensionless number, and can be expressed as

$$\vec{y}_j = \ln(\vec{x}_j),$$

such that

$$\delta\vec{x}_j \frac{\delta}{\delta\vec{x}_j}\vec{f}_i = \left[\frac{\delta\vec{x}_j}{\vec{x}_j}\right]\left[\vec{x}_j \frac{\delta}{\delta\vec{x}_j}\vec{f}_i\right] = \delta\vec{y}_j \frac{\delta}{\delta\vec{y}_j}\vec{f}_i.$$

This formulation makes the derivative $\delta\vec{f}_i/\delta\vec{y}_j$ a dimensionless multiple of the actual function, and leads to simplifications in coding. Equation (3.9) becomes

$$\vec{f}_j^n + \delta\vec{y}_{j-1}^n \frac{\delta}{\delta\vec{y}_{j-1}}\vec{f}_j^n + \delta\vec{y}_j^n \frac{\delta}{\delta\vec{y}_j}\vec{f}_j^n + \delta\vec{y}_{j+1}^n \frac{\delta}{\delta\vec{y}_{j+1}}\vec{f}_j^n = 0. \tag{3.10}$$

This expression can be written as a tridiagonal matrix equation for a vector whose components are also vectors [26, p. 12]. Define $\underline{X}$ to be a vector whose first $N+3$ components are $\vec{x}_1$, the next $N+3$ are $\vec{x}_2$, and so on until the last zone resulting in

$$\{X\} = \begin{Bmatrix} \vec{x}_1 \\ \vec{x}_2 \\ \vdots \\ \vec{x}_L \end{Bmatrix},$$

Constructing $\delta\underline{Y}$ and $\underline{F}$ similarly, yields the matrix form of (3.9)

$$\underline{F'} = 0.$$

Additionally, (3.10) turns into

$$[T^n]\{\delta Y^n\} = \{F^n\}, \tag{3.11}$$

where

$$[T^n] = \begin{bmatrix} A_1 & B_1 & & & & & \\ C_2 & A_2 & B_2 & & & & \\ & C_3 & A_3 & B_3 & & & \\ & & \ddots & \ddots & \ddots & & \\ & & & \ddots & \ddots & \ddots & \\ & & & & \ddots & \ddots & B_{L-1} \\ & & & & & C_L & A_L \end{bmatrix},$$

$$\{\delta Y^n\} = \begin{Bmatrix} \delta\vec{y}_1 \\ \delta\vec{y}_2 \\ \vdots \\ \delta\vec{y}_L \end{Bmatrix},$$

and

$$\{F^n\} = \begin{Bmatrix} \vec{f}_1 \\ \vec{f}_2 \\ \vdots \\ \vec{f}_L \end{Bmatrix}.$$

This matrix equation is solved using a Gaussian elimination technique in the form of LU decomposition. The L matrix is block lower triangular, while the U matrix is unit upper triangular, with

$$T = LU,$$

$$L = \begin{bmatrix} D_1 & & & & \\ C_2 & D_2 & & & \\ & C_3 & D_3 & & \\ & & \ddots & \ddots & \\ & & & & \end{bmatrix},$$

$$U = \begin{bmatrix} 1 & E_1 & & & \\ & 2 & E_2 & & \\ & & 3 & E_3 & \\ & & & \ddots & \ddots \\ & & & & \end{bmatrix}.$$

3.2 Cantera

Cantera uses object-oriented software tools for problems involving chemical kinetics, thermodynamics and transport processes [28]. This program is freely available and can be used with Python, Matlab, FORTRAN and C++. The documentation for Cantera is still evolving, and at this point there is not an all inclusive manual.

The Cantera package comes with demonstrations and example codes. These examples show how to solve a one dimensional propagating flame and compute the flame speed. This is the only feature of this code that has been utilized. An example of the Python script used for the flame speed calculation is included in Appendix B.

3.3 Summary

Two flames codes have been presented: HCT and Cantera. The governing equations for HCT have been described in detail. These equations include the species conserva-

tion equation (3.1), momentum conservation (3.2), conservation of energy (3.3) and the equation governing the change in the width of each zone (3.4). The discretization of each of the equations has been shown, and the solution technique has been covered. A sample of the code used in Cantera is contained in Appendix B. Both of these codes are used in the work herein to computed the flame speed of a one-dimensional propagating methan-air flame.

CHAPTER IV

ENTROPY INEQUALITY

The differential entropy inequality is the local form of the second law of thermodynamics. This form of the entropy inequality contains four terms, each of which is discussed in detail. The first term takes into account the entropy increase due to viscosity, the second term represents the entropy created from diffusion, the third term represents the entropy increase due to chemical reactions, and the final term represents the entropy increase due to heat transfer.

The differential entropy inequality is written as [29, pp. 436-465]

$$-\mathrm{tr}\left[\left(\overline{\overline{\tau}}+p\overline{\overline{I}}\right)\cdot\nabla\vec{v}\right]+cRT\sum_{B=1}^{N-1}\vec{J}_B\cdot\left(\frac{\vec{d}_B}{\rho_B}-\frac{\vec{d}_N}{\rho_N}\right)+\sum_{B=1}^{N-1}(\mu_B-\mu_N)r_B+\frac{1}{T}\vec{\epsilon}\cdot\nabla T\leq 0, \tag{4.1}$$

where N is the number of species in the mixture. The parameters of the entropy inequality are briefly discussed in the following sections. The entropy inequality is numerically implemented in a user-defined function (UDF) that is used to check converged solutions in FLUENT for entropy inequality violations. For the work herein, the UDF is used to check steady laminar methane-air flames for entropy violations.

4.1 First Term

This section discusses the first term on the left hand side of (4.1). This term takes into account the entropy increase in the domain from shear stress. The first term is

written as

$$-tr\left[\left(\overline{\overline{\tau}}+p\overline{\overline{I}}\right)\cdot\nabla\vec{v}\right], \tag{4.2}$$

where $\overline{\overline{I}}$ is the identity matrix, $\vec{v}$ is the velocity, p is the thermodynamic pressure and $\overline{\overline{\tau}}$ is the stress tensor. For a Newtonian fluid, the stress tensor is defined as

$$\overline{\overline{\tau}}=\left(-p+\lambda(\nabla\cdot\vec{v})\right)\overline{\overline{I}}+2\mu\overline{\overline{D}}, \tag{4.3}$$

with

$$\lambda=-\frac{2}{3}\mu, \tag{4.4}$$

and

$$\overline{\overline{D}}=\frac{1}{2}\left[\nabla\vec{v}+(\nabla\vec{v})^{T}\right], \tag{4.5}$$

where λ is the bulk viscosity, μ is the shear viscosity and $\overline{\overline{D}}$ is the rate of deformation tensor. Substituting (4.3), (4.4) and (4.5) into (4.2) leads to [30, p. 99]

$$-tr\left[\left(\mu[\nabla\vec{v}++(\nabla\vec{v})^{T}]-\frac{2}{3}\mu(\nabla\cdot\vec{v})\overline{\overline{I}}\right)\cdot\nabla\vec{v}\right].$$

4.2 Second Term

This section discusses the second term of the left hand side of (4.1). The second term represents the entropy created from the diffusion of species and is written as

$$cRT\sum_{B=1}^{N-1}\vec{J}_{B}\cdot\left(\frac{\vec{d}_{B}}{\rho_{B}}-\frac{\vec{d}_{N}}{\rho_{N}}\right), \tag{4.6}$$

where T is the temperature, R is the universal gas constant, c is the total molar density and $\vec{J}_i$ is the diffusive mass flux vector of species i. The diffusive mass flux vector was introduced on page 11. The total molar density c is computed by summing

the contributions from each species, resulting in

$$c = \sum_{i=1}^{N} \frac{\rho_i}{M_i},$$

where ρ_i is the density of species i, and M_i is the molecular weight of species i. $\vec{d_i}$ in (4.6) is defined as [29, p. 458]

$$\vec{d_i} = \nabla X_i + \frac{X_i M_i}{RT}\left[\left(\tilde{\mathbf{V}} - \frac{1}{\rho}\right)\nabla P - \vec{f_i} + \sum_{j=1}^{N} Y_j \vec{f_j}\right]. \tag{4.7}$$

Under the assumption that the numerical simulation is isobaric, confirmed by experimental investigation, the first term in the brackets can be neglected. Additionally, the external forces are neglected, assuming the effect of gravity on the system is negligibly small and affects all species the same. These simplifications lead to [30, p. 103]

$$\vec{d_i} = \nabla X_i.$$

FLUENT only allows the user access to the gradient of the mass fraction, ∇Y_i, as opposed to the mole fraction, ∇X_i. Therefore, the UDF must calculate the mass fraction from the mole fraction using [25, p. 19]

$$X_i = \frac{Y_i}{W_i \sum_{j=1}^{N} \frac{Y_j}{W_j}}.$$

Taking the gradient of both sides leads to

$$\nabla X_i = \frac{\nabla Y_i}{W_i \sum_{j=1}^{N} \frac{Y_j}{W_j}} - \frac{Y_i}{\left(W_i \sum_{j=1}^{N} \frac{Y_j}{W_j}\right)^2} W_i \sum_{j=1}^{N} \frac{\nabla Y_j}{W_j}.$$

4.3 Third Term

This section discusses the third term,

$$\sum_{B=1}^{N-1}(\mu_B - \mu_N)r_B,$$

of the left hand side of (4.1). This term represents the increase in entropy due to the chemical reactions and can be re-written as [29, p. 465]

$$RT\sum_{r=1}^{K}\sum_{i=1}^{N}\ln\left(\frac{1}{K_r}[\gamma_i X_i]^{\nu_{i,r}}\right)\frac{r_{N,r}}{M_N\nu_{N,r}},$$

where R is the universal gas constant, T is the temperature, K_r is the equilibrium constant for reaction r, γ_i is the activity coefficient for species i, and $\nu_{i,r}$ is the overall stoichiometric coefficient for each species i in reaction r.

Previous work has investigated the activity coefficient and determined that the coefficient should be set to one [30, p. 107]. Therefore, in the work herein the activity coefficient is set to unity. The overall stoichiometric coefficient is defined as the stoichiometric coefficient of the species in the products minus the coefficient of the species in the reactants

$$\nu_{i,r} = \nu''_{i,r} - \nu'_{i,r},$$

where $'$ represents the reactant and $''$ represents the product of species i in reaction r.

The equilibrium constant for each reaction must be defined as a function of temperature. The constant can be related to the standard heat of reaction ΔH^o by [30, p. 106], [31, p. 508]

$$\frac{d(\ln K)}{dT} = \frac{\Delta H^o}{RT^2}. \tag{4.8}$$

Assuming the standard heat of reaction is a function of T, (4.8) can be integrated to yield [30, p. 106]

$$\ln K = \int \frac{\Delta H^o}{RT^2} dT + I, \tag{4.9}$$

where I is an integration constant. The expression for ΔH^o is

$$\Delta H^o = \int \Delta C_p^o dT + J, \tag{4.10}$$

where J is also an integration constant. C_p is approximated as the ideal gas specific heat capacity , [31, p. 108]

$$\frac{C_p^{ig}}{R} = A + BT + CT^2 + DT^{-2}. \tag{4.11}$$

Substituting (4.11) and (4.10) into (4.9) and integrating leads to [30, p. 106], [31, p. 508]

$$\ln K = -\frac{J}{RT} + (\Delta A)\ln T + \frac{\Delta B}{2} T + \frac{\Delta C}{6} T^2 + \frac{\Delta D}{2T^2} + I.$$

This derivation is described in more detail in [30, pp. 105-106] and [31, pp. 507-508]. The constants A, B, C and D can be found from tabulated data in the literature [31, p. 109]. The operator Δ is defined as the values of the property of the reactants subtracted from the property of the products for the reaction. The integration constants I and J can be found using the standard values of ΔH_{298} and ΔG_{298} [31, p. 512].

4.4 Fourth Term

This section discusses the fourth term on the left hand side of (4.1)

$$\frac{1}{T} \vec{\epsilon} \cdot \nabla T.$$

This term represents the entropy increase due to heat transfer. The only parameter introduced here is $\vec{\epsilon}$, which can be defined using kinetic theory of dilute gases as [29, p. 449]

$$\vec{\epsilon} = -k\Delta T - cRT \sum_{i=1}^{N} D_{T,i} \frac{\vec{d_i}}{\rho_i},$$

where k is the thermal conductivity, T is the temperature, c is the total molar density, R is the universal gas constant, $D_{T,i}$ is the thermal diffusion coefficient and $\vec{d_i}$ is defined in (4.7). The thermal conductivity and thermal diffusion coefficients are defined on page 12.

4.5 Summary

This chapter has introduced the differential entropy inequality, the local form of the second law of thermodynamics. The approaches to each of the four terms in (4.1) have been discussed. The first term on the left hand side of (4.1) takes into account the entropy increase due to viscosity, the second term represents the entropy created from diffusion, the third term represents the entropy increase due to chemical reactions, and the final term represents the entropy increase due to heat transfer. Each term is described in more detail in [30, pp. 98-111]. The numerical implementation of the entropy inequality has been coded in a UDF that is utilized within FLUENT. The UDF determines if a numerical solution has predicted cells that violate the second law of thermodynamics. For the work herein, the entropy inequality UDF is used to check steady laminar methane-air flames for violations.

CHAPTER V

REDUCED MECHANISMS

This chapter introduces the reduced mechanisms used in this work and the methods used to develop them. The first section presents a brief example of reducing a hydrogen-oxygen mechanism. The example is intended to introduce the reduction process used for the four- and three-step methane combustion mechanisms. The second section introduces four-step and three-step methane combustion mechanisms. The four- and three-step mechanism derivations are discussed. The last section describes the Westbrook and Dryer method of matching flame speed. This method leads to the two-step mechanism that is used in most of the work herein.

5.1 Reduction Process

This section provides an example of how to start with a suitable reaction mechanism and systematically reduce it down to a simple mechanism. The process begins with an eight-reaction hydrogen-oxygen mechanism made up of seven species, shown in Table I.

Steady state assumptions for a species lead to algebraic equations between reactions rates, and each of these equations can be used to eliminate rates in the remaining balance equations for the non-steady state species [32, p. 52] and ω_i is the rate of progress of reaction i. The resulting reduced mechanism depends on the rates chosen to be eliminated. Generally the fastest reactions are chosen for elimination. The

Table I. Hydrogen-Oxygen Combustion Mechanism
Rate Coefficients in the form $k_f = AT^{\beta} \exp(-E_o/RT)$
Units are moles, cubic centimeters, seconds, Kelvins, and calories/mole

	Reaction			A	β	E
1f.	$H + O_2$	$\rightarrow$	$OH + O$	2.000E+14	0.0	16800
1b.	$OH + O$	$\rightarrow$	$H + O_2$	1.575E+13	0.0	690
2f.	$O + H_2$	$\rightarrow$	$OH + H$	1.800E+10	1.0	8826
2b.	$OH + H$	$\rightarrow$	$O + H_2$	8.000E+09	1.0	6760
3f.	$H_2 + OH$	$\rightarrow$	$H_2O + H$	1.170E+09	1.3	3626
3b.	$H_2O + H$	$\rightarrow$	$H_2 + OH$	5.090E+09	1.3	18588
4f.	$OH + OH$	$\rightarrow$	$O + H_2O$	6.000E+08	1.3	0
4b.	$O + H_2O$	$\rightarrow$	$OH + OH$	5.900E+09	1.3	17029
5	$H + O_2 + M$	$\rightarrow$	$HO_2 + M^a$	2.300E+18	-0.8	0
6	$H + HO_2$	$\rightarrow$	$OH + OH$	1.500E+14	0.0	1004
7	$H + HO_2$	$\rightarrow$	$H_2 + O_2$	2.500E+13	0.0	700
8	$OH + HO_2$	$\rightarrow$	$H_2O + O_2$	2.000E+13	0.0	1000

[a] Third body efficiencies: $CH_4 = 6.5$, $H_2O = 6.5$, $CO_2 = 1.5$, $H_2 = 1.0$, $CO = 0.75$, $O_2 = 0.4$, $N_2 = 0.4$ All other species = 1.0
[b] Lindemann form, $k = k_{\infty}/(1 + k_{fall}/[M])$ where $k_{fall} = 0.0063 \exp(-18000/RT)$

algebraic equations for this example are written as [32, p. 52]

$$L([H]) = -\omega_1 + \omega_2 + \omega_3 - \omega_5 - \omega_6 - \omega_7$$

$$L([OH]) = 0 = \omega_1 + \omega_2 - \omega_3 - 2\ \omega_4 + 2\ \omega_6 - \omega_8$$

$$L([O]) = 0 = \omega_1 - \omega_2 + \omega_4$$

$$L([H_2]) = -\omega_2 - \omega_3 + \omega_7$$

$$L([O_2]) = -\omega_1 - \omega_5 + \omega_7 + \omega_8$$

$$L([H_2O]) = \omega_3 + \omega_4 + \omega_8$$

$$L([HO_2]) = 0 = \omega_5 - \omega_6 - \omega_7 - \omega_8$$

where $L([])$ is defined as a linear differential operator which may contain the time derivative as well as convective and diffusive terms [32, p. 52]. The $[s]$ denotes the concentration of species s. The sign convention for the rates is positive if the species is produced and negative if the species is consumed.

A numerical simulation must be conducted with the hydrogen-oxygen mechanism in Table I to determine which species to set to steady state. An order of magnitude analysis is used to determine the species that have the smallest effect on the solution. The species OH, O and HO_2 are set to steady state, indicated by the equations set to zero above. The fastest rates for these species are determined to be ω_2 for O, ω_3 for OH and ω_7 for HO_2 [32, p. 52] and therefore an effort is made to eliminate these reaction rates. The following linear combinations eliminate these reaction rates

$$\begin{aligned}
L([\mathrm{H}]) + \{L([\mathrm{OH}]) + 2L([\mathrm{O}]) - L([\mathrm{HO_2}])\} &= 2\ \omega_1 - 2\ \omega_5 + 2\ \omega_6 \\
L([\mathrm{H_2}]) + \{-L([\mathrm{OH}]) - 2\ L([\mathrm{O}]) + L([\mathrm{HO_2}])\} &= -3\ \omega_1 + \omega_5 - 3\ \omega_6 \\
L([\mathrm{O_2}]) + \{L([\mathrm{HO_2}])\} &= -\omega_1 - \omega_6 \\
L([\mathrm{H_2O}]) + \{L([\mathrm{OH}]) + L([\mathrm{O}])\} &= 2\ \omega_1 + 2\ \omega_6.
\end{aligned}$$

The terms in the brackets are the steady state species and are set to zero. After this simplification, and grouping the terms on the right such that the rates with the same stoichiometric coefficients are added together, the following equations are formed

$$\begin{aligned}
L([\mathrm{H}]) &= 2\ (\omega_1 + \omega_6) - 2\ \omega_5 \\
L([\mathrm{H_2}]) &= -3\ (\omega_1 + \omega_6) + \omega_5 \\
L([\mathrm{O_2}]) &= -(\omega_1 + \omega_6) \\
L([\mathrm{H_2O}]) &= 2\ (\omega_1 + \omega_6).
\end{aligned}$$

These algebraic equations are used to determine the new reaction mechanism. The $L([\mathrm{H}])$ equation has a positive 2 for the first reaction and a negative 2 for the second reaction. This indicates that H is produced in the first reaction with a stoichiometric coefficient of 2, and is consumed in the second reaction with a stoichiometric coefficient of 2. The four equations above lead to the two-step reaction mechanism for hydrogen-

oxygen combustion [32, p. 52]

$$\text{I} \quad 3\ H_2 + O_2 \rightarrow 2\ H + 2\ H_2O$$

$$\text{II} \quad 2\ H + M \rightarrow H_2 + M$$

with the reaction rates defined as

$$\omega_{\text{I}} = \omega_1 + \omega_6$$

$$\omega_{\text{II}} = \omega_5.$$

The M in reaction II comes from the fact that reaction 5 in the skeletal mechanism is a third-body reaction. This example shows the general scheme in reducing reactions mechanisms. The steady state species were identified and used to eliminate the fast reactions, and a mechanism with eight reactions and seven species was reduced to two reactions and four species. This methodology is used to derive the four-step and three-step mechanisms for methane-oxygen combustion in the next sections.

5.2 Four-Step Methane Combustion Mechanism

This section describes the derivation of a four-step methane combustion mechanism, and leads into a three-step mechanism in the next section. The general reduction process has been covered in section 5.1. The only additional step to the development of the four-step mechanism is partial equilibrium approximations.

The four-step mechanism is derived by starting from a suitable skeletal mechanism. Skeletal mechanisms are often derived from a full mechanism, such as the GRI-Mech 3.0 [9], which contains 325 reactions and 53 species. The skeletal mechanism utilized in this derivation is displayed in Table II [14, p. 23]. This mechanism is considered insufficient for rich methane flames because only the C1-chain is present,

but serves as a suitable starting point of this derivation.

After the skeletal mechanism is identified, the next step is to identify the steady state species. To do this a numerical calculation must be carried out to compare the relative orders of magnitude of each species concentration in the mechanism. Peters conducted this investigation and determined that the species OH, O, HO_2, CH_3, CH_2O, CHO, CH_3O and H_2O_2 are less that one percent of the total concentration of the mixture [32, p. 55]. The species OH and O are considered in partial equilibrium for ease in the following calculations, and the remaining six species are set to a steady state for the remainder of the derivation. The partial equilibrium representation of O is found from reaction 2b in Table II, and is written as

$$[\mathrm{O}] = \frac{[\mathrm{H}][\mathrm{OH}]}{[\mathrm{H_2}]K_2}.$$

The partial equilibrium representation of OH is found from reaction 3b in Table II, and is written as [33, p. 21]

$$[\mathrm{OH}] = \frac{[\mathrm{H}][\mathrm{H_2O}]}{[\mathrm{H_2}]K_3}.$$

The first reaction of the four-step mechanism is found by summing the fastest reactions of the C1 chain, reactions 11, 13 ,17 and 22, and the partial equilibrium

Table II. Skeletal Methane-Air Combustion Mechanism
Rate Coefficients in the form $k_f = AT^{\beta} \exp(-E_o/RT)$
Units are moles, cubic centimeters, seconds, Kelvins, and calories/mole

	Reaction			A	β	E
1f.	$H + O_2$	$\rightarrow$	$OH + O$	2.000E+14	0.0	16800
1b.	$OH + O$	$\rightarrow$	$H + O_2$	1.575E+13	0.0	690
2f.	$O + H_2$	$\rightarrow$	$OH + H$	1.800E+10	1.0	8826
2b.	$OH + H$	$\rightarrow$	$O + H_2$	8.000E+09	1.0	6760
3f.	$H_2 + OH$	$\rightarrow$	$H_2O + H$	1.170E+09	1.3	3626
3b.	$H_2O + H$	$\rightarrow$	$H_2 + OH$	5.090E+09	1.3	18588
4f.	$OH + OH$	$\rightarrow$	$O + H_2O$	6.000E+08	1.3	0
4b.	$O + H_2O$	$\rightarrow$	$OH + OH$	5.900E+09	1.3	17029
5	$H + O_2 + M$	$\rightarrow$	$HO_2 + M^a$	2.300E+18	-0.8	0
6	$H + HO_2$	$\rightarrow$	$OH + OH$	1.500E+14	0.0	1004
7	$H + HO_2$	$\rightarrow$	$H_2 + O_2$	2.500E+13	0.0	700
8	$OH + HO_2$	$\rightarrow$	$H_2O + O_2$	2.000E+13	0.0	1000
9f.	$CO + OH$	$\rightarrow$	$CO_2 + H$	1.510E+07	1.3	-758
9b.	$CO_2 + H$	$\rightarrow$	$CO + OH$	1.570E+09	1.3	22337
10f.	$CH_4 + (M)$	$\rightarrow$	$CH_3 + H + (M)^b$	6.300E+14	0.0	104000
10b.	$CH_3 + H + (M)$	$\rightarrow$	$CH_4 + (M)^b$	5.200E+12	0.0	-1310
11f.	$CH_4 + H$	$\rightarrow$	$CH_3 + H_2$	2.200E+04	3.0	8750
11b.	$CH_3 + H_2$	$\rightarrow$	$CH_4 + H$	9.570E+02	3.0	8750
12f.	$CH_4 + OH$	$\rightarrow$	$CH_3 + H_2O$	1.600E+06	2.1	2460
12b.	$CH_3 + H_2O$	$\rightarrow$	$CH_4 + OH$	3.020E+05	2.1	17422
13	$CH_3 + O$	$\rightarrow$	$CH_2O + H$	6.800E+13	0.0	0
14	$CH_2O + H$	$\rightarrow$	$HCO + H_2$	2.500E+13	0.0	3991
15	$CH_2O + OH$	$\rightarrow$	$HCO + H_2O$	3.000E+13	0.0	1195
16	$HCO + H$	$\rightarrow$	$CO + H_2$	4.000E+13	0.0	0
17	$HCO + M$	$\rightarrow$	$CO + H + M$	1.600E+14	0.0	14700
18	$CH_3 + O_2$	$\rightarrow$	$CH_3O + O$	7.000E+12	0.0	25652
19	$CH_3O + H$	$\rightarrow$	$CH_2O + H_2$	2.000E+13	0.0	0
20	$CH_3O + M$	$\rightarrow$	$CH_2O + H + M$	2.400E+13	0.0	28812
21	$HO_2 + HO_2$	$\rightarrow$	$H_2O_2 + O_2$	2.000E+12	0.0	0
22f.	$H_2O_2 + M$	$\rightarrow$	$OH + OH + M$	1.300E+17	0.0	45500
22b.	$OH + OH + M$	$\rightarrow$	$H_2O_2 + M$	9.860E+14	0.0	-5070
23f.	$H_2O_2 + OH$	$\rightarrow$	$H_2O + HO_2$	1.000E+13	0.0	1800
23b.	$H_2O + HO_2$	$\rightarrow$	$H_2O_2 + OH$	2.860E+13	0.0	32790
24	$OH + H + M$	$\rightarrow$	$H_2O + M^a$	2.200E+22	-2.0	0
25	$H + H + M$	$\rightarrow$	$H_2 + M^a$	1.800E+18	-1.0	0

[a] Third body efficiencies: $CH_4 = 6.5$, $H_2O = 6.5$, $CO_2 = 1.5$, $H_2 = 1.0$, CO= 0.75, $O_2 = 0.4$, $N_2 = 0.4$ All other species = 1.0

[b] Lindemann form, $k = k_{\infty}/(1 + k_{fall}/[M])$ where $k_{fall} = 0.0063 \exp(-18000/RT)$

reactions, reactions 2b and 3b [32, p. 55].

$$11 \quad CH_4 + H \rightarrow CH_3 + H_2$$

$$13 \quad CH_3 + O \rightarrow CH_2O + H$$

$$15 \quad CH_2O + H \rightarrow CHO + H_2$$

$$17 \quad HCO + M \rightarrow CO + H + M$$

$$2b \quad OH + H \rightarrow O + H_2$$

$$3b \quad H_2O + H \rightarrow H_2 + OH$$

Summing the six reactions together yields

$$\text{I} \quad CH_4 + 2H + H_2O \rightarrow CO + 4H_2.$$

The water-gas shift reaction can be found by combining reactions 3 and 10 from Table II [32, p. 56].

$$10 \quad CO + OH \rightleftharpoons CO_2 + H$$

$$3 \quad H + H_2O \rightleftharpoons OH + H_2$$

Combining yields

$$\text{II} \quad CO + H_2O \rightleftharpoons CO_2 + H_2.$$

The third reaction in the mechanism comes from reactions 5, 8 and 3b [33].

$$5 \quad O_2 + H + M \rightarrow HO_2 + M$$

$$8 \quad OH + HO_2 \rightarrow H_2O + O_2$$

$$3b \quad H + H_2O \rightarrow OH + H_2$$

Combining these reactions yields

$$\text{III} \quad \mathrm{H} + \mathrm{H} + \mathrm{M} \rightarrow \mathrm{H_2} + \mathrm{M}.$$

Finally, the fourth reaction is a combination of reactions 1, 2 and 3 [32, p. 56].

$$1 \quad \mathrm{O_2} + \mathrm{H} \rightleftharpoons \mathrm{OH} + \mathrm{O}$$

$$2 \quad \mathrm{O} + \mathrm{H_2} \rightleftharpoons \mathrm{OH} + \mathrm{H}$$

$$3 \quad \mathrm{OH} + \mathrm{H_2} \rightleftharpoons \mathrm{H_2O} + \mathrm{H}$$

Combining, with the third reaction taken twice, yields:

$$\text{IV} \quad \mathrm{O_2} + 3\mathrm{H_2} \iff 2\mathrm{H_2O} + 2\mathrm{H}.$$

The rates for these reactions are expressed by the elementary reaction rates as

$$w_{\mathrm{I}} = w_{11}$$

$$w_{\mathrm{II}} = w_9$$

$$w_{\mathrm{III}} = w_5$$

$$w_{\mathrm{IV}} = w_1.$$

These reaction rates can be written in terms of the elementary rate constants, k_i, given in Table II, and the equilibrium constants K_i, as [34, p. 26].

$$\begin{aligned}
w_{\mathrm{I}} &= k_{11}[\mathrm{CH_4}][\mathrm{H}] \\
w_{\mathrm{II}} &= \frac{k_{9f}}{K_3}\frac{[\mathrm{H}]}{[\mathrm{H_2}]}\left\{[\mathrm{CO}][\mathrm{H_2O}] - \frac{1}{K_{II}}[\mathrm{CO_2}][\mathrm{H_2}]\right\} \\
w_{\mathrm{III}} &= k_5[\mathrm{H}][\mathrm{O_2}][\mathrm{M}] \\
w_{\mathrm{IV}} &= k_{1f}\frac{[\mathrm{H}]}{[\mathrm{H_2}]^3}\left\{[\mathrm{O_2}][\mathrm{H_2}]^3 - \frac{1}{K_{IV}}[\mathrm{H}]^2[\mathrm{H_2O}]^2\right\},
\end{aligned}$$

with [33, p. 22]

$$K_2 = 2.23\exp(-1112/T)$$

$$K_3 = 0.216\exp(7658/T)$$

$$K_{\mathrm{II}} = 0.035\exp(3652/T)$$

$$K_{\mathrm{IV}} = 1.48\exp(6133/T).$$

5.3 Three-Step Methane Combustion Mechanism

The four-step mechanism can be reduced to a three-step mechanism by using a steady-state balance for the H-atom concentration. This balance comes from setting $w_{\mathrm{IV}} = w_{\mathrm{I}} + w_{\mathrm{III}}$, and the resulting H concentration is [34, p. 26]

$$[\mathrm{H}] = \frac{K_{IV}^{1/2}[\mathrm{O_2}]^{1/2}[\mathrm{H_2}]^{1/2}}{[\mathrm{H_2O}]}\left[1 - \frac{k_5[\mathrm{M}]}{k_1} - \frac{k_{11}[\mathrm{CH_4}]}{k_1[\mathrm{O_2}]}\right].$$

This steady-state approximation leads to the three-step mechanism:

$$\mathrm{I} \quad \mathrm{CH_4 + O_2 \rightarrow CO + H_2 + H_2O}$$

$$\mathrm{II} \quad \mathrm{CO + H_2O \rightleftharpoons CO_2 + H_2}$$

$$\mathrm{III} \quad \mathrm{O_2 + 2H_2 \rightarrow 2H_2O}.$$

The four and three-step mechanisms have been reduced from the skeletal mechanism shown in Table II. The three-step mechanism is used in the work herein to simulate a non-premixed laminar methane-air flame. The next section introduces the two-step mechanism of Westbrook and Dryer.

5.4 Two-Step Methane Combustion Mechanism

This section introduces Westbrook and Dryer's method for developing a reduced reaction mechanism for hydrocarbon fuels. Westbrook and Dryer's approach is to match the flame speed, S_L, for the hydrocarbon fuel at an equivalence ratio of one. The focus of this work is on mechanisms developed for methane-air combustion. Westbrook and Dryer's method is described for a one-step global reaction and is applied to a two-step mechanism by adding the oxidation of carbon monoxide. The two-step mechanism developed with this method is the basis for most of the work herein.

Westbrook and Dryer's method was applied to various hydrocarbon fuels [1, p. 38], using the global reaction form

$$\hat{R} = AT^{\beta} \exp \frac{E}{RT} [\text{Fuel}]^a [\text{Oxidizer}]^b.$$

This reaction form is a general equation that can be applied to any hydrocarbon fuel. $\hat{R}$ takes the form of the Arrhenius reaction rate, introduced on page **??**. For the global methane-air reaction

$$\text{CH}_4 + 2\ \text{O}_2 \rightarrow \text{CO}_2 + 2\ \text{H}_2\text{O},$$

Westbrook and Dryer kept the activation energy, E, constant and varied the pre-exponential factor, A, and the reaction exponents, a and b, to match the flame speed at an equivalence ratio of one. After matching the flame speed at an equivalence ratio of one, they used HCT to solve for the flame speed at various equivalence ratios. The equivalence ratio is defined as the ratio of the mass of fuel, F, to oxidizer, O, divided by the stoichiometric ratio of mass of fuel to oxidizer

$$\phi = \frac{F/O}{F/O_{st}}.$$

Table III. Global Methane-Air Combustion Mechanisms

	A *	E_a [kcal/mol]	a	b
Set 1	1.3×10^8	48.4	-0.3	1.3
Set 2	6.7×10^{12}	48.4	0.2	1.3
Set 3	1.0×10^{13}	48.4	0.7	0.8
Set 4	2.4×10^{16}	48.4	1.0	1.0

Sets of Arrhenius parameters for the global methane-air reaction from Westbrook and Dryer.
*Consistent units

Thus, an equivalence ratio of one indicates a stoichiometric reaction. The constants used for the thermal and molecular diffusivity terms described on page 21 were determined [1, p. 32] by matching the experimental flame speed at an equivalence ratio of one with a detailed reaction mechanism [2, p. 125]. The mechanisms shown in Table III are plotted in Fig. 2, along with the detailed reaction mechanism.

This method is also used to develop a two-step mechanism for methane-air combustion. The same process is used for the methane oxidation reaction, and the oxidation of carbon monoxide is also modeled. The resulting two-step mechanism is

$$\mathrm{CH_4} + 1.5\ \mathrm{O_2} \rightarrow \mathrm{CO} + 2\ \mathrm{H_2O}$$

$$\mathrm{CO} + 0.5\ \mathrm{O_2} \rightleftharpoons \mathrm{CO_2}.$$

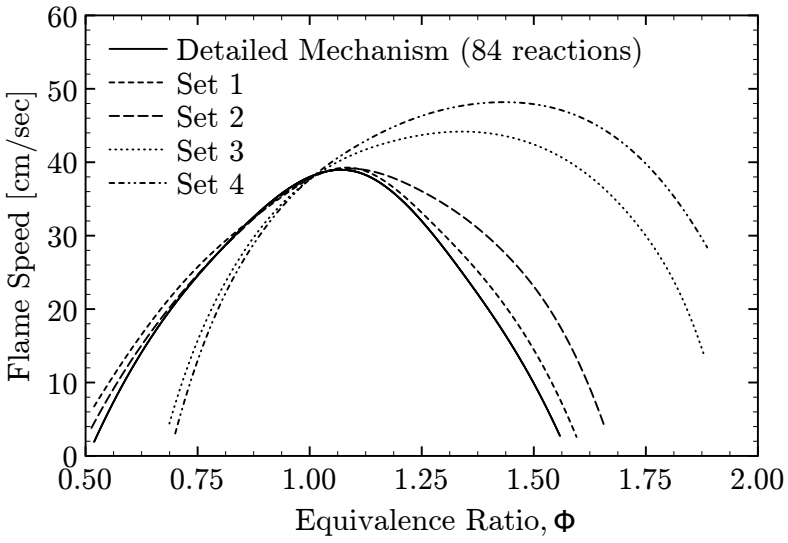

Figure 2. Flame speed vs. equivalence ratio: Detailed reaction mechanism (84 reactions, 26 species) for methane-air combustion, as well as the global reaction mechanism sets [1, p. 36]

5.5 Methane-Air Flame Speed

This section examines the method from Westbrook and Dryer and uses HCT to match results reported in [1, p. 36]. A grid convergence investigation is used to determine the spatial discretization needed to capture the flame speed. The procedure for computing the flame speed from HCT output is discussed, and further details of the computation are included in Appendix A.

5.5.1 Grid Convergence

This section reports the results of a grid convergence analysis of HCT. The grid points are clustered towards the region with the maximum temperature gradient. Clustering takes place at every time-step, thus the grid is constantly adjusting to accommodate the propagating flame front. A grid convergence test is essential to determine the number of zones needed to capture the position of the flame front.

Four grids are used for the grid convergence study, with 25, 50, 75, and 100 zones. Two velocities must be calculated in order to find the flame speed, the lab frame of reference speed and the velocity in the last zone. HCT outputs the flame front position at a time increment specified in the input file. The flame propagation speed in the lab frame of reference can be calculated from subsequent time-steps, by dividing the change in the flame front location by the change in time. The flame speed is found by subtracting the velocity in the last spatial zone from the lab reference speed.

This computation suggests two methods of conducting the grid convergence study. The obvious way is to calculate the flame speed for each grid, shown in Table IV. Alternatively, one can observe the change in the velocity in the last spatial zone. The velocity in the last zone will become constant when the flame front is steadily

propagating. One can plot the velocity in the last spatial zone against the iteration

Table IV. Flame Speed Grid Convergence

Grid Size [zones]	Flame Speed [cm/sec]
25	36.15
50	35.03
75	33.52
100	33.47

number to determine when the solution has reached convergence. This study shows that each grid produces the same velocity in the last zone, 230 cm/sec, at different convergence rates, shown in Fig. 3. The difference in the computed flame speed between 75 and 100 zones is minimal, therefore, this grid convergence investigation suggests that 75 zones are sufficient in capturing the flame speed. The 75 zone grid is used in the next section to reproduce data reported by Westbrook and Dryer [1, p. 36].

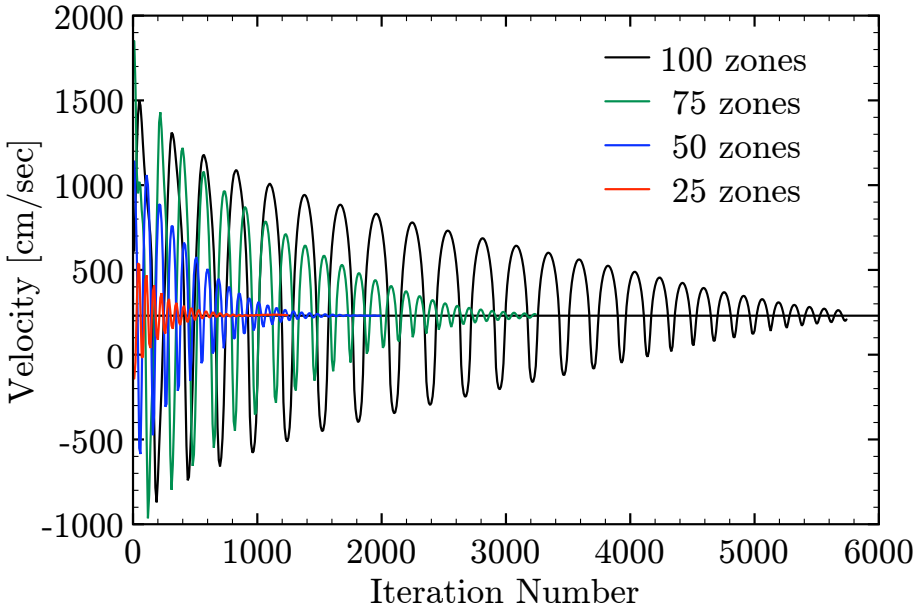

Figure 3. Velocity in the last spatial zone versus iteration number for the 25, 50, 75 and 100 zone grid sizes.

5.5.2 Methane-Air Flame Speed Comparisons

This section presents experimental results to compare with the detailed mechanism (84 reactions, 26 species) reported by Westbrook and Dryer [2, p. 125]. The mechanism is compared with experimentally measured flame speeds and the GRI-3.0 detailed mechanism. Set 3 from Table III is arbitrarily chosen and reproduced using the current version of HCT. The results from the current version of HCT are compared with the results generated by Westbrook and Dryer for set 3 [1, p. 36]. Additionally, a sensitivity analysis is conducted on sets 1, 2 and 3 from Table III. This investigation is used to determine the validity of the development of the two-step mechanism. For the remainder of the chapter the detailed mechanism consisting of 84 reactions and 26 species from Westbrook and Dryer is referred to as WDM.

Experimental methane-air flame speed data have been compiled from many sources to validate WDM. This collection of experimental data includes results obtained using different experimental methods for measuring flame speeds. This should provide for an un-biased set of data. The most popular technique for measuring flame speed is a spherical bomb method [35]-[39]. In this method, the fuel mixture is ignited at the center of a spherical container, and as the flame front propagates outward a high-speed camera can capture the flame propagation speed. Another popular method is a counterflow technique, that uses Doppler velocimetry to measure the flame speed [40]-[43]. This technique involves establishing two symmetrical, planar, nearly adiabatic flames in a counterflow, then the axial velocity of the centerline of the flow is determined from Doppler velocimetry [42]. Figure 4 shows the experimental flame speed data, the results from using WDM in HCT, and the results from the GRI-3.0 mechanism used in Cantera.

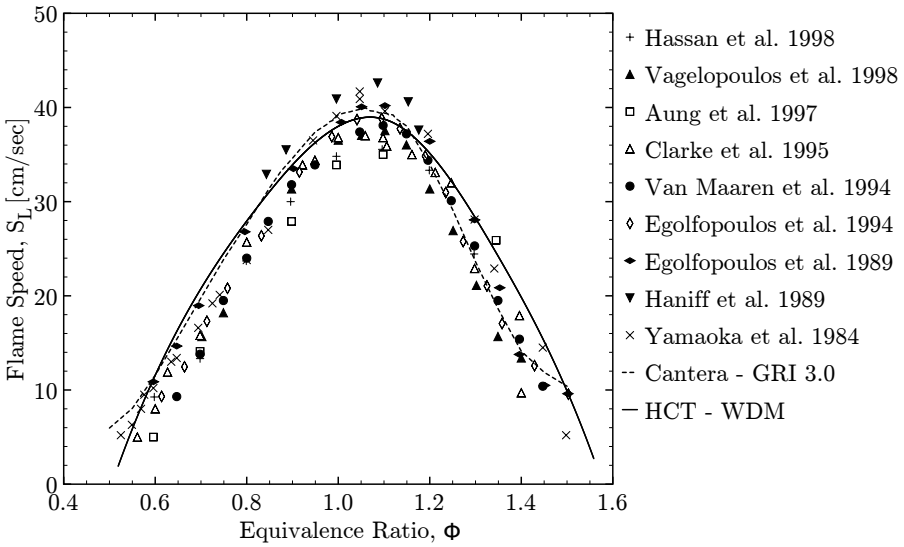

Figure 4. Flame speed vs. equivalence ratio: Experimental flame speed data, along with flame speeds from HCT using GRI-3.0 and Cantera using WDM [2, p. 125].

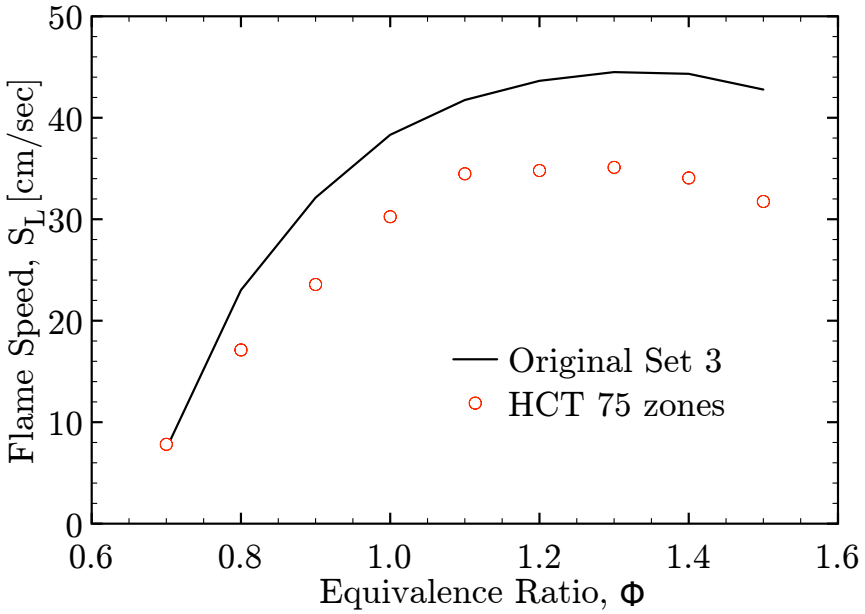

Figure 5. Flame speed vs. equivalence ratio: Flame speeds using set 3 from Westbrook and Dryer with original and updated version of HCT.

Figure 4 shows that the detailed mechanism used in the development of the two-step mechanism is accurately predicting the flame speeds. This study also shows that the GRI-Mech 3.0 mechanism is more accurate for rich methane-air flames.

Figure 5 shows the results from using set 3 with HCT to reproduce the flames speeds reported by Westbrook and Dryer [1, p. 36]. The results from this study indicate that the HCT program is computing different flame speeds than Westbrook and Dryer reported. The HCT code has been modified extensively over the years since set 3 was reported in 1981. These modifications could have easily caused this change in flame speed calculation. The results reported in Fig. 5 show that HCT is producing results that are worse now than there were in 1981.

The reason HCT is still used is because it allows the user to specify each parameter in the Arrhenius rate equation, including the reaction exponents. In Cantera the stoichiometric coefficients are set to the reaction exponents and the values cannot be modified. A sensitivity analysis is conducted using HCT because all the parameters of the reduced methane combustion mechanism can be altered. The sensitivity analysis on sets 1, 2, and 3 [1, p. 36] of the global mechanism from Westbrook and Dryer are displayed in Tables V-VII. The Arrhenius form is written as

$$k = AT^{\beta} \exp\left(-\frac{E}{RT}\right) [\mathrm{CH_4}]^{n_1} [\mathrm{O_2}]^{n_2}.$$

Table V. Set 1 Sensitivity Analysis

Para.	Original	Altered	$\Delta para$	S_L	ΔS_L	Sens. $\frac{\Delta S_L}{\Delta para}$
A	1.30×10^8	1.3130×10^8	1.30×10^6	14.11	0.07	5.38×10^{-8}
		1.28700×10^8	-1.30×10^6	13.97	-0.07	5.38×10^{-8}
E	4.84×10^4	4.8884×10^4	4.84×10^2	NA	NA	NA
		4.8642×10^4	2.42×10^2	13.62	-0.42	-0.0017
		4.8158×10^4	-2.42×10^2	14.46	0.42	-0.0017
		4.7916×10^4	-4.84×10^2	14.89	0.85	-0.0018
n_1	-0.3	-0.3090	-9.00×10^{-3}	16.09	2.05	-227.7778
		-0.3060	-6.00×10^{-3}	15.76	1.72	-286.6667
		-0.3030	-3.00×10^{-3}	15.27	1.23	-410.0000
		-0.2970	3.00×10^{-3}	14.47	0.43	143.3333
		-0.2940	6.00×10^{-3}	14.09	0.05	8.3333
		-0.2910	9.00×10^{-3}	13.73	-0.31	-34.4444
n_2	1.3	1.3130	1.30×10^{-2}	NA	NA	NA
		1.3065	6.50×10^{-3}	13.32	-0.72	-110.7692
		1.2935	-6.50×10^{-3}	15.68	1.64	-252.3077
		1.2870	1.30×10^{-2}	16.58	2.54	-195.3846
β	0	0.1	0.1	20.69	6.65	665.0000
		-0.1	-0.1	NA	NA	NA

$S_L = 14.04$ cm/sec, at $\phi = 1$

Table VI. Set 2 Sensitivity Analysis

Para.	Original	Altered	$\Delta para$	S_L	ΔS_L	Sens. $\frac{\Delta S_L}{\Delta para}$
A	6.70×10^{12}	6.7670×10^{12}	6.70×10^{10}	31.32	0.09	1.34×10^{-12}
		6.6330×10^{12}	-6.70×10^{10}	31.04	-0.19	2.84×10^{-12}
E	4.84×10^4	4.8884×10^4	4.84×10^2	29.36	-1.87	-0.0039
		4.7916×10^4	-4.84×10^2	32.90	1.67	-0.0035
n_1	0.2	0.2020	2.00×10^{-3}	30.68	-0.55	-275.0000
		0.1980	-2.00×10^{-3}	31.45	0.22	-110.0000
n_2	1.3	1.3130	1.30×10^{-2}	27.56	-3.67	-282.3077
		1.2870	-1.30×10^{-3}	34.63	3.40	-261.5385
β	0	0.005	0.005	31.60	0.37	74.0000
		-0.005	-0.005	31.11	-0.12	24.0000

$S_L = 31.23$ cm/sec, at $\phi = 1$

Table VII. Set 3 Sensitivity Analysis

Para.	Original	Altered	$\Delta para$	S_L	ΔS_L	Sens. $\frac{\Delta S_L}{\Delta para}$
A	1.00×10^{13}	1.0200×10^{13}	2.00×10^{11}	30.27	0.02	1.00×10^{-13}
		9.8000×10^{12}	-2.00×10^{11}	29.73	-0.52	2.60×10^{-12}
E	4.84×10^4	4.8884×10^4	4.84×10^2	NA	NA	NA
		4.8642×10^4	2.42×10^2	28.75	-1.50	-0.0062
		4.8158×10^4	-2.42×10^2	30.59	0.34	-0.0014
		4.7916×10^4	-4.84×10^2	31.90	1.65	-0.0034
n_1	0.7	0.7700	7.00×10^{-3}	NA	NA	NA
		0.7035	3.50×10^{-3}	29.13	-1.12	-320.0000
		0.6965	-3.50×10^{-3}	30.69	0.44	-125.7143
		0.6930	-7.00×10^{-3}	31.69	1.44	-205.7143
n_2	0.8	0.8080	8.00×10^{-3}	27.78	-2.47	-308.7500
		0.7920	-8.00×10^{-3}	32.24	1.99	-248.7500
β	0	0.1	0.1	30.95	0.70	70.0000
		-0.1	-0.1	28.63	-1.62	16.2000

$S_L = 30.25$ cm/sec, $\phi = 1$

The flame speed is calculated using the global reaction mechanism in HCT. The sensitivity analysis of the flame speed is conducted by altering the original parameters in the Arrhenius rate by ± one percent. The sensitivity is defined as the change in the flame speed, ΔS_L, divided by the change in the parameter, $\Delta para$. If the code produced an unbounded solution during the simulation, indicated with NA in Tables V-VII, then the parameter was altered by half a percent. The flame speed consistently has the highest sensitivity to the pre-exponential factor A, and the reaction exponents, n_1 and n_2. Therefore, this analysis offers reasoning to the mechanism development method from Westbrook and Dryer. They varied the three parameters that have the highest effect on the flame speed. This made matching the flame speed at a specific equivalence ratio an easier task.

5.6 Summary

The reduction process from a skeletal mechanism to a reduced combustion mechanism has been covered in detail with the hydrogen-oxygen example. The reduction process along with partial equilibrium assumptions has led to the four- and three-step methane combustion mechanisms of Peters. These mechanisms were developed by reducing a skeletal mechanism that consisted of 25 reactions. Another approach introduced is matching the flame speed to develop a reduced mechanism. The methodology from Westbrook and Dryer has been introduce and validated through experimental comparisons and sensitivity analyses. Their work developed the two-step mechanism that is used extensively in the following chapters.

CHAPTER VI

RESULTS

The experimental setup for Flame A is discussed briefly, and the domain and boundary conditions for numerical simulation are presented. The results for the two- and three-step methane combustion mechanism numerical simulations are presented. Results for each mechanism are introduced separately and compared later in the chapter. Modifications are made to the Westbrook and Dryer two-step methane combustion mechanism to form the new mechanisms Mech 1 and Mech 2. The methodology to these modifications is discussed in detail. The results from numerical simulations with the new methane combustion mechanisms are discussed and compared to the results with the two-step methane combustion mechanism from Westbrook and Dryer.

6.1 Problem Statement

The purpose of this section is to introduce the domain and boundary conditions provided from Sandia National Laboratory. Sandia has many combustion experiments that have been made available to the public. This research focuses on a laminar methane-air flame, referred to as Flame A. The results from this experiment are reported at 25, 50, and 100 mm downstream from the end of the fuel tube. These results include temperature and species mass fractions measured from the middle of the flame radially outward. This problem is discussed in detail, and the experimental measurements are shown later in this section in the grid convergence discussion.

6.1.1 Domain

The experimental setup is introduced briefly, and the three-dimensional domain is reduced down to a two-dimensional computational domain. The boundary conditions for the two-dimensional domain are introduced. Three grids are generated for the numerical simulations. These grids are used for a grid convergence investigation. This investigation leads to a final mesh that is used for the remainder of this work.

6.1.1.1 Physical Domain

The Flame A experiment consists of a tube surrounded by a wind tunnel with one square foot cross section. The tube has an inner diameter of 0.304 inches and an outer diameter of 0.375 inches. The tube brings in a pre-mixed methane-air mixture, and the wind tunnel provides a co-flow of air. The pre-mixed fuel is too fuel rich to combust without mixing with the air in the co-flow, and will be defined exactly in the next section. The experimental set-up consists of lasers that are sent through the flame. The laser light collides with the different species in the flame. These species emit different wavelengths of light that can be captured by a fluorescent detector. The technique used in this experiment uses Raman/Rayleigh and Laser-Induced Fluorescence to measure the species in single point fashion [30, p. 85]. The flame was scanned at the three axial locations of 25, 50 and 100 mm downstream from the end of the fuel tube. The data are reported measuring from the center of the flame radially outward, implying an axisymmetric flame. The resolution of the measurement was 500 microns [30, p. 85]. Figure 6 displays the three dimensional domain.

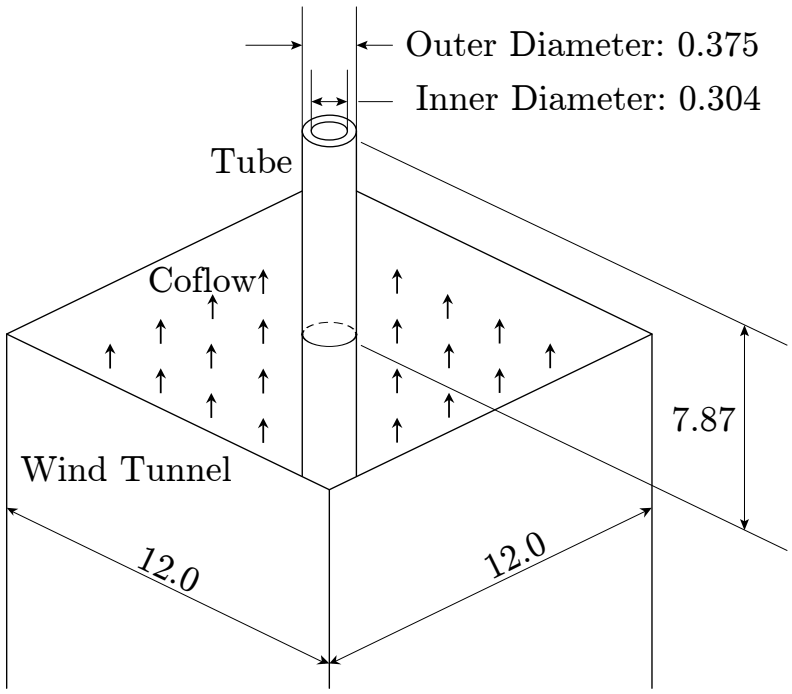

Figure 6. Flame A experimental setup: Units are in inches and figure is not to scale.

The three dimensional domain is simplified by taking a two dimensional slice, shown in Fig. 7. The domain is further simplified by utilizing the symmetry of the problem and forming an axisymmetric axis boundary. This assumption is consistent with the data provide from Sandia, measured from the center radially outward. With these simplifications only half of the domain shown in Fig. 7 is needed for meshing and computation.

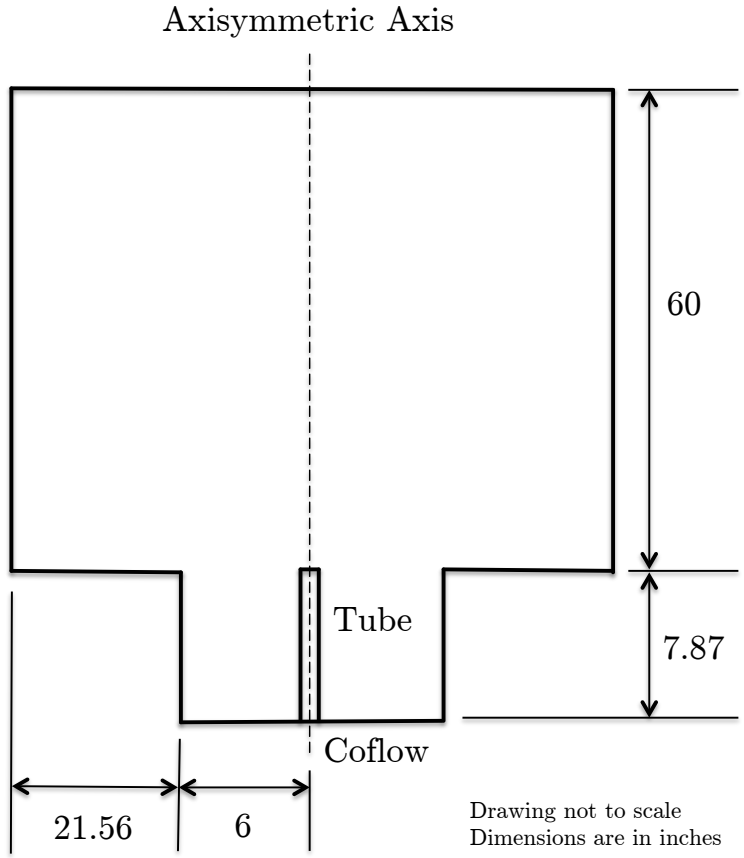

Figure 7. Flame A 2-D: Two dimensional slice of three dimensional domain in Fig. 6.

6.1.1.2 Boundary Conditions

The boundary conditions for the numerical simulation are discussed in this section. These conditions come from the Flame A experiment conducted by Sandia National Laboratories.

The velocities of the flow in the tube and the co-flow are provided from Sandia, and a velocity inlet condition must be specified in the domain. The tube is long enough that the flow can be assumed fully developed, and a bulk velocity of 2.90 m/sec is specified. The wind tunnel around the tube brings a co-flow of ambient air at a velocity of 0.40 m/sec. Both of these velocities are specified in the axial directions, along the axisymmmetric axis. The static temperature at the inlet is also specified at 300 K. The flow comes into the domain as premixed, thus, the mass fractions for both the fuel mixture and the co-flow must be specified at the inlet. The co-flow is ambient air, which has a widely known composition, and the pre-mixed fuel mixture has a composition specified by Sandia. These mass fractions can be seen in Table VIII, along with the velocity inlet conditions.

The wind tunnel ends upstream from the tube, and the domain opens up into a room at ambient conditions. For the boundaries far from the flame, representing the room, static pressure boundary conditions are specified. The static pressure is set to standard atmospheric conditions, and the composition of ambient air is used for the mass fractions. The ambient air boundaries are chosen to limit back-flow into the domain. This phenomena was investigated by Chambers [30, p. 89], and the static pressure boundary condition was found to be sufficient. Table IX shows the outlet pressure boundary conditions for the simulation. The last boundary conditions required for the simulation are the axisymmetric axis boundary and the boundary conditions for the wall of the tube. The axisymmetric axis is along the centerline

Table VIII. Inlet Boundary Conditions

Parameter	Premixed Fuel	Co-Flow
Velocity Mag. [m/s]	2.90	0.40
Static Temp. [K]	300	300
Mass Fraction		
CH_4	0.1527	0.0000
O_2	0.1944	0.2295
CO_2	0.0004	0.0005
CO	0.0000	0.0000
H_2O	0.0066	0.0078
N_2	0.6459	0.7491

of the tube and extends to the outlet of the domain. The tube wall has a no-slip boundary condition and an adiabatic wall condition.

This section has introduced all of the boundary conditions needed to run the simulation. The following section will describe the generation of the computational grid and summarize a grid convergence investigation.

6.1.2 Grid Generation

This section outlines the generation of the computational grid, and the choices made in the process. The grid was created using GAMBIT [44], a program from ANSYS that is used frequently with FLUENT. A grid convergence study is conducted to ensure the solution is independent of the grid size.

The generation of the grid is an important part of this investigation. Where the boundaries are located and the types of boundary conditions have a large impact

Table IX. Outlet Boundary Conditions

Parameter	Outer Domain
Static Pressure [Pa]	101325
Back-flow Total Temperature [K]	300
Back-flow Direction	normal to boundary
Mass Fraction	
CH_4	0.0000
O_2	0.2295
CO_2	0.0005
CO	0.0000
H_2O	0.0078
N_2	0.7491

on the solution. The boundaries for the velocity inlets are upstream of the end of the tube. This is ideal because a boundary layer forms on the inside and outside walls of the tube. If the inlets were at the end of the tube, much more precise inlet conditions would have to be defined in order capture the correct solution. With the inlets farther upstream, the boundary layers develop naturally. The wall y^+ number along both walls of the tube is less than 0.5 [30, p. 96]. Moving these boundaries back and revolving the solution about the axisymmetric axis yields a circular wind tunnel instead of a square wind tunnel. It is assumed that this simplification has little to no effect on the numerical solution because the walls of the wind tunnel are far enough away from the laminar flame. The final geometry to be meshed is the left half of Fig. 7.

The grid was created with a few small zones at the end of the tube, with the

intent of increasing the temperature in these zones to initiate combustion. FLUENT does not allow access to individual cells to increase temperatures, but the zone temperatures can be modified. Most of the domain is an unstructured mesh, with the boundary layers consisting of structured grids. Many regions were created to control the sizing of the mesh. These regions allow for the clustering of smaller cells around the tube, while larger cells are downstream of the tube.

To determine if the laminar methane-air flame solution is grid independent, the simulation is conducted on three grids. The coarse grid contains 106,867 cells, the medium grid contains 167,523 cells and the fine grid contains 319,523 cells. The methane-air flame simulation is conducted using the two-step methane combustion mechanism from Westbrook and Dryer for each mesh size. The solutions for each mesh are compared by plotting the temperature and methane mass fraction versus radial position at 25, 50 and 100 mm downstream from the exit of the tube. Figures 8-13 display the results from the two-step methane combustion mechanism at each axial location, as well as the experimental data from Sandia. The solution changes drastically from the coarse mesh to the medium mesh, but hardly changes at all from the medium mesh to the fine mesh. This indicates the medium mesh is sufficient for this simulation, and is used for the work herein.

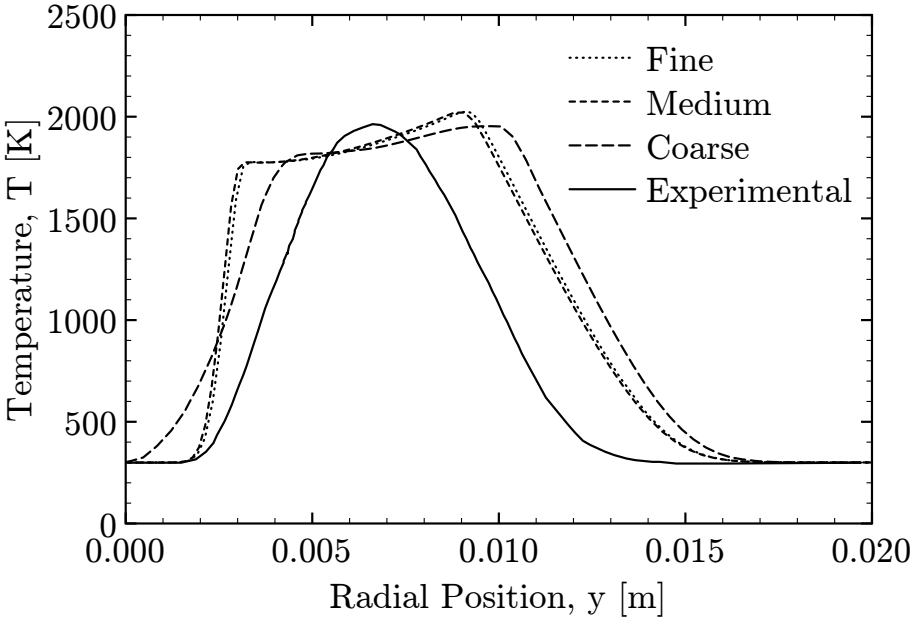

Figure 8. Temperature vs. radius at 25 mm downstream from the burner for the two-step methane combustion mechanism grid convergence study.

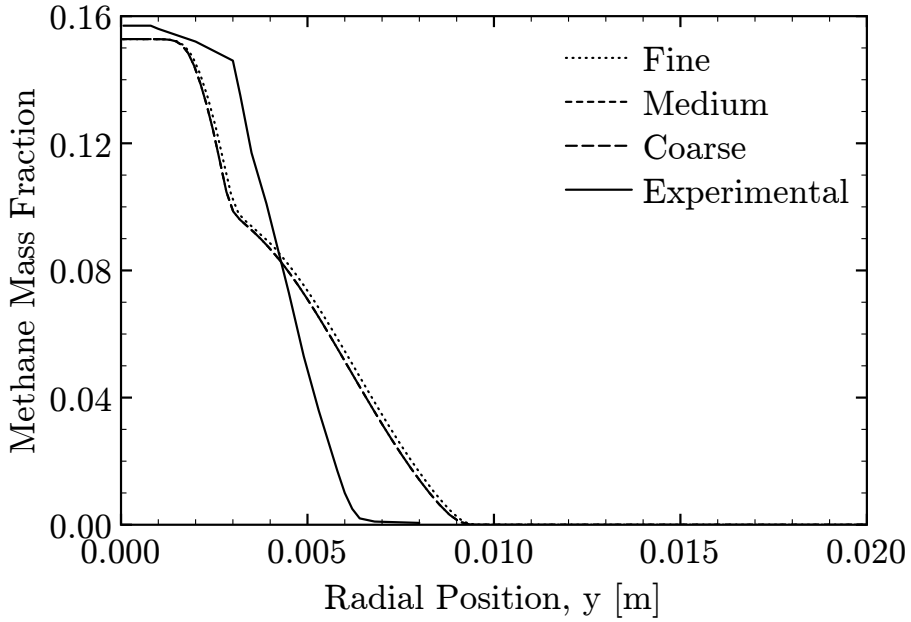

Figure 9. Methane mass fraction vs. radius at 25 mm downstream from the burner for the two-step methane combustion mechanism grid convergence study.

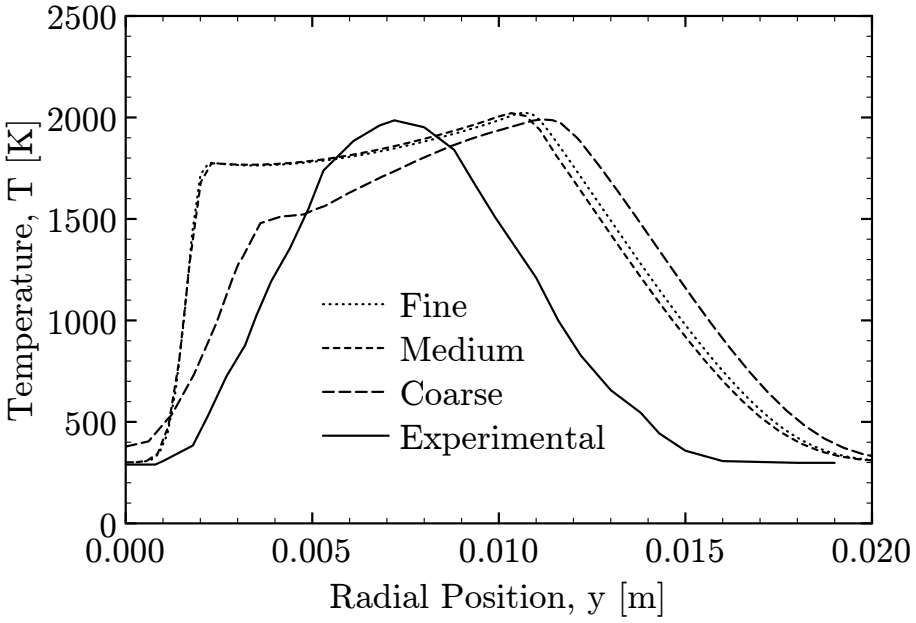

Figure 10. Temperature vs. radius at 50 mm downstream from the burner for the two-step methane combustion mechanism grid convergence study.

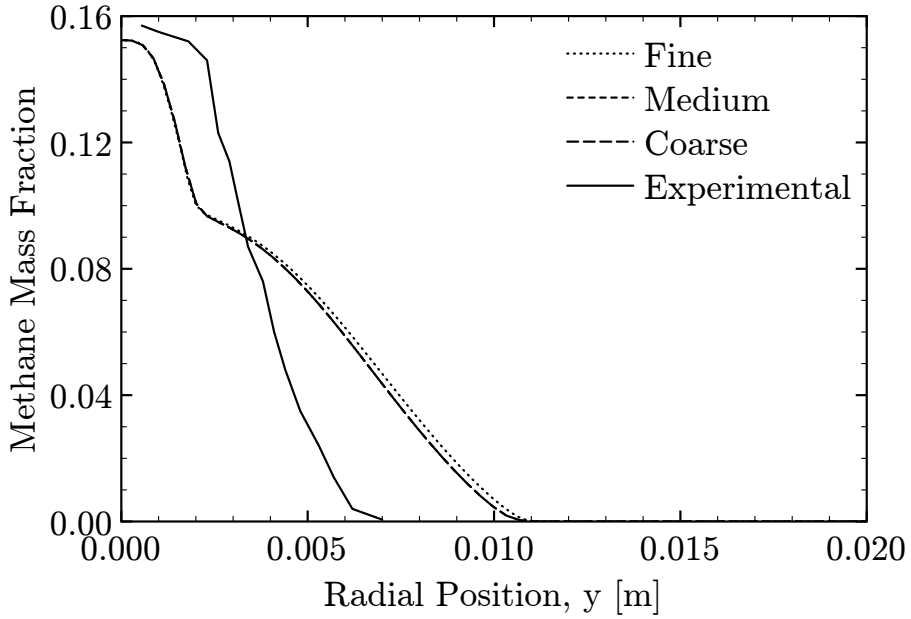

Figure 11. Methane mass fraction vs. radius at 50 mm downstream from the burner for the two-step methane combustion mechanism grid convergence study.

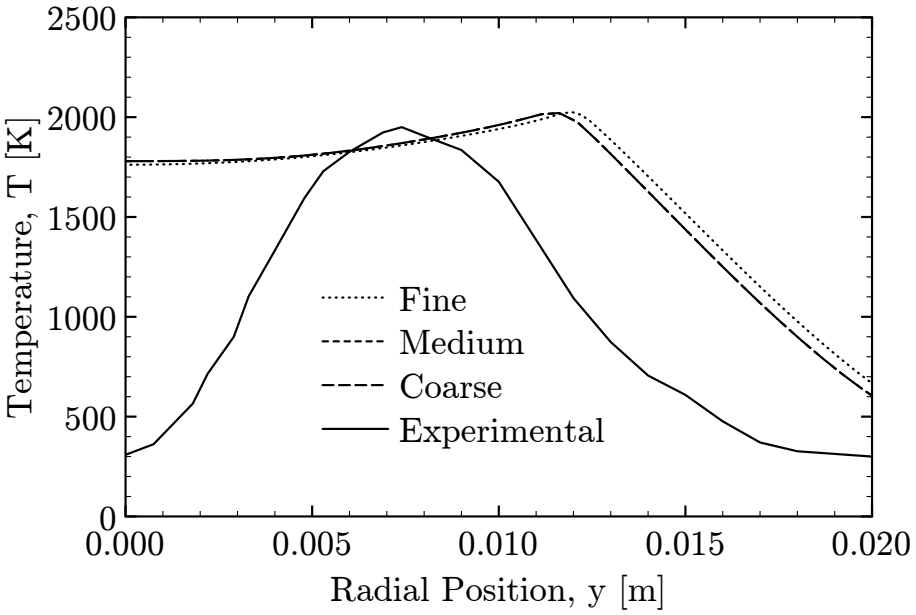

Figure 12. Temperature vs. radius at 100 mm downstream from the burner for the two-step methane combustion mechanism grid convergence study.

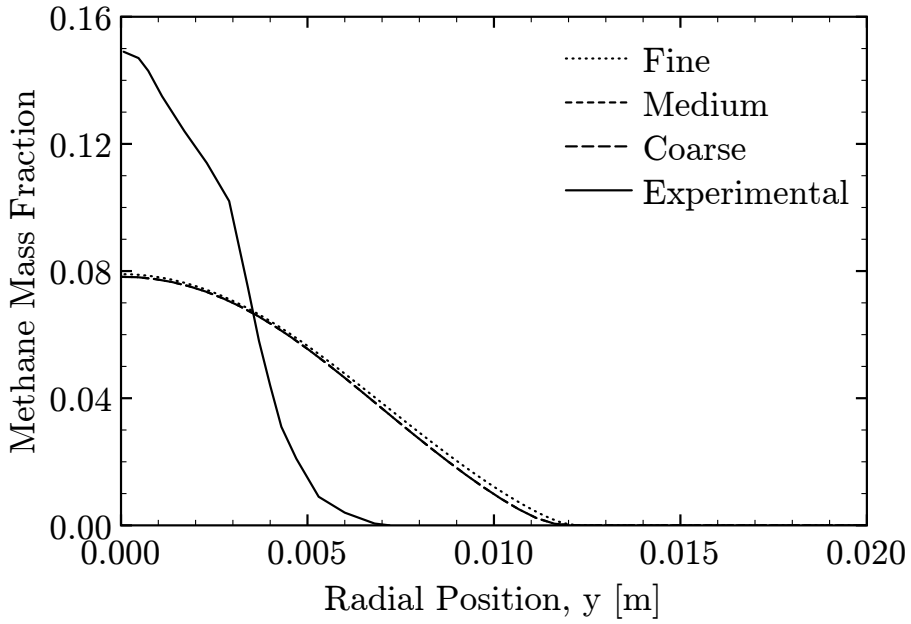

Figure 13. Methane mass fraction vs. radius at 100 mm downstream from the burner for the two-step methane combustion mechanism grid convergence study.

6.2 Simulation with Two-Step Methane Combustion Mechanism

The results from the numerical simulation with the two-step methane combustion mechanism developed by Westbrook and Dryer [1, pp. 37-38] are presented here. The two-step methane combustion mechanism is shown below with the Arrhenius parameters in Table X.

$$CH_4 + 1.5\ O_2 \rightarrow CO + 2\ H_2O$$

$$CO + 0.5\ O_2 \rightleftharpoons CO_2$$

Table X. Two-Step Methane Combustion Mechanism

Reaction	A	E	a	b
1	5.012×10^{11}	48.4	0.70	0.8
2_f	2.239×10^{12}	40.0	0.25	0.5
2_b	5.000×10^{8}	40.0	1.00	–

Arrhenius parameters for Westbrook and Dryer's two-step mechanism, units of E are in J/kmol.

The results presented in this section include the laminar methane-air flame produced using the two-step methane combustion mechanism in FLUENT, the entropy inequality violations discovered in the solution and the effect of the Soret thermal diffusion coefficient on the solution. A numerical simulation with modified boundary conditions is conducted with the two-step methane combustion mechanism, and is compared with the original boundary condition simulation. The purpose of the modified boundary conditions simulation is to compare the result with the three-step methane combustion mechanism simulation, which requires the modified boundary

conditions. This phenomena is discussed in further detail in the three-step methane combustion mechanism section.

6.2.1 Entropy Inequality Violations

This section presents the entropy inequality violations found from the laminar methane-air flame simulation with the two-step methane combustion mechanism. The simulation was conducted in FLUENT, and a user-defined function was used to check the converged solution for entropy inequality violations. Figure 14 shows the laminar methane-air flame produced by the two-step methane combustion mechanism simulation. The maximum temperature for this simulation is limited to 2025 K. The simulation diverges quickly without the temperature limiter. A study on the effect of the temperature limiter on the laminar methane-air flame simulation was conducted by Chambers [30, pp. 112-114]. The 2025 K temperature limiter is used for the work herein because the laminar flame solution resembles the experimental data the closest. The red boxed area in Fig. 14 is the area where the entropy inequality vio-

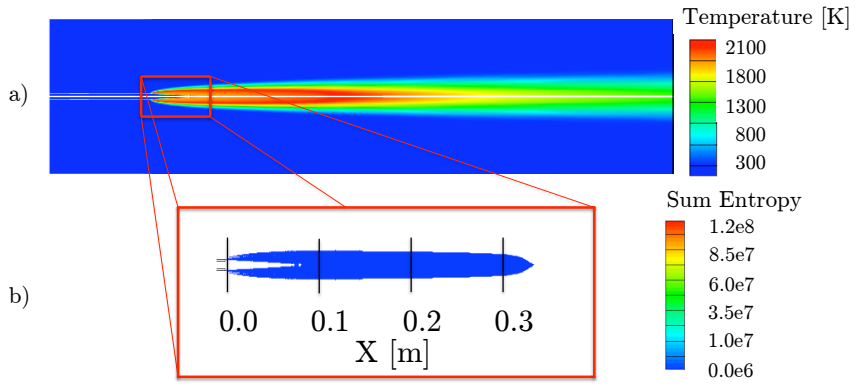

Figure 14. Two-step methane combustion mechanism results: a) temperature contour plot, b) entropy violations, sum of entropy terms that is positive.

lations occur for this simulation. The lowest value on the entropy violation contour plot is zero, therefore anything that shows up on the plot is a cell that violates the inequality. The entropy inequality expression reaches a peak along the axisymmetric centerline boundary. There is also a small region of violations downstream along the axisymmetric axis leading into the outlet. This region is relatively cold compared to the region near the tube. The hot region near the tube and how to reduce this region is the concern of this work.

6.2.2 Effect of Soret Thermal Diffusion Coefficient

The effect of the Soret thermal diffusion coefficient on the entropy inequality violations was investigated and the results are reported in this section. For this investigation two numerical simulations were conducted using the two-step methane combustion mechanism in FLUENT. The first simulation produced a flame using a form of the Soret thermal diffusion coefficient that will cause heavy molecules to diffuse less towards heated surfaces, and light molecules to diffuse more rapidly towards heated surfaces [18, sec. 13.1.1]. The Soret diffusion coefficient used in the first simulation is written as [19]

$$D_{T,i} = -2.59 \times 10^{-7} T^{0.659} \left[\frac{M_{w,i}^{0.511} X_i}{\sum_{i=1}^{n} M_{w,i}^{0.511} X_i} - Y_i \right] \cdot \left[\frac{\sum_{i=1}^{n} M_{w,i}^{0.511} X_i}{\sum_{i=1}^{n} M_{w,i}^{0.489} X_i} \right], \qquad (6.1)$$

where T is the temperature, X_i is the mole fraction of species i, Y_i is the mass fraction of species i, and M_i is the molecular weight of species i. This is the form of the diffusion coefficient introduced on page 12. The second simulation produced a flame with the Soret thermal diffusion coefficient turned off. The two simulations were compared by examining the normalized temperature difference and the absolute methane mass fraction difference throughout the domain. This yields a 50% maximum difference in temperature between the two simulations, which is equivalent to a difference of 1022

K. The methane mass fraction yielded a maximum difference of 0.027. The differences throughout the domain are shown in Fig. 15.

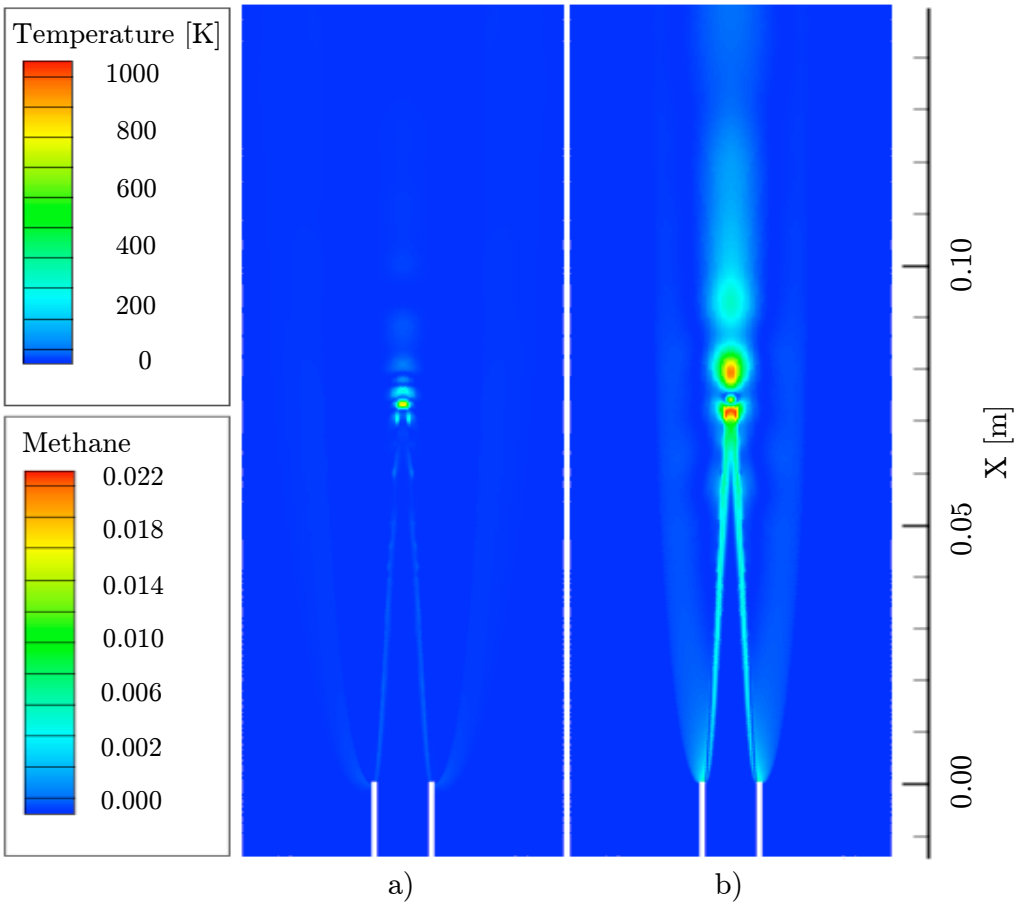

Figure 15. Effect of Soret thermal diffusion coefficient: a) absolute difference in temperature, b) absolute difference in methane mass fraction.

Both simulations violated the entropy inequality. The simulation with the Soret thermal diffusion coefficient turned on yielded 22,016 cells that violated the entropy inequality, and the simulation with the coefficient turned off produced 23,280 cells that violated the entropy inequality. This increase was relatively small compared to the number of cells clustered in the area of the violations. The results indicated however that the Soret thermal diffusion coefficient reduced the number of entropy inequality violations.

6.2.3 Modified Boundary Conditions Simulation

The modified boundary conditions simulation with the two-step methane combustion mechanism was conducted to compare with the three-step methane combustion mechanism simulation. Additionally, this simulation was compared with the original boundary conditions simulation. The modified boundary conditions consists of altering the fuel mixture by replacing the oxygen concentration with nitrogen. The modified inlet boundary conditions are shown in Table XI. The fuel mixture for the modified boundary conditions is referred to as non-premixed, while the fuel mixture with the original boundary conditions is referred to as premixed.

6.2.3.1 Entropy Inequality Violations

The two-step methane combustion mechanism numerical simulation with the non-premixed fuel leads to a significant reduction in the number of cells violating the entropy inequality. The premixed fuel simulation produced 22,016 cell violations, while the non-premixed fuel simulation produced 273 cell violations. The resulting flame solution and entropy inequality violations are shown in Fig. 16. The hot region of entropy violations is significantly reduced when comparing Fig. 16 with Fig. 14. There is once again a cold region downstream with violations.

Table XI. Modified Inlet Boundary Conditions

Parameter	Fuel	Co-Flow
Velocity Mag. [m/s]	2.90	0.40
Static Temp. [K]	300	300
Mass Fraction		
CH_4	0.1527	0.0000
O_2	**0.0000**	0.2295
CO_2	0.0004	0.0005
CO	0.0000	0.0000
H_2O	0.0066	0.0078
N_2	**0.8403**	0.7491

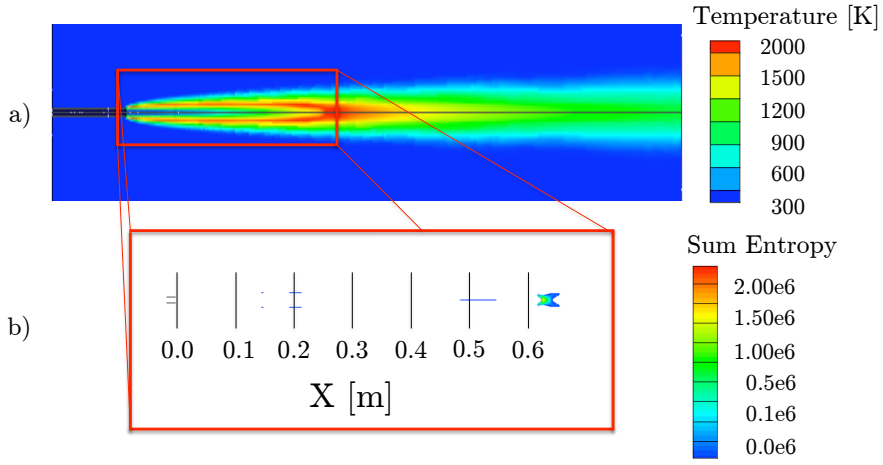

Figure 16. Two-step methane combustion mechanism non-premixed case: a) temperature contour plot, b) entropy inequality violations, sum of entropy terms that is positive.

6.2.4 Premixed and Non-Premixed Simulation Comparisons

The premixed and non-premixed fuel cases are compared at 25 mm downstream of the fuel tube. The temperature for both simulations is examined, and each entropy term is compared. Additionally, the solutions are compared by examining the absolute difference in temperature and methane mass fraction contours.

The original premixed two-step methane combustion mechanism simulation has a noticeable plateau where the temperature limiter is in effect, while the modified non-premixed simulation has more of a parabolic shape like the experimental data. The region on Fig. 17 where the premixed and non-premixed lines intersect is where the temperature limiter effects the non-premixed simulation. This region gives a since of how much smaller of an area the limiter is effecting the solution, compared to the large plateau region of the original solution.

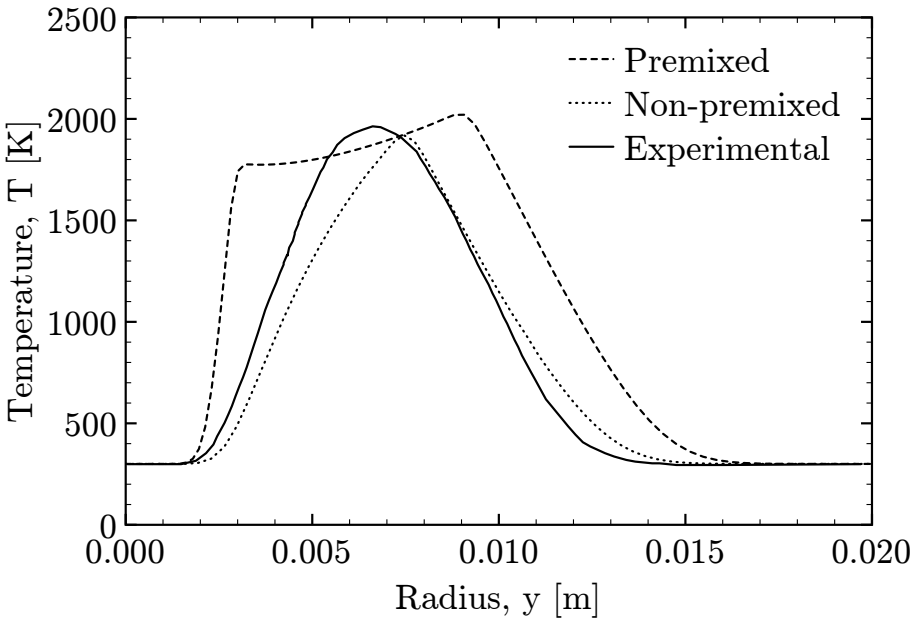

Figure 17. Temperature vs. radius at 25 mm downstream for the premixed and non-premixed simulations.

Each term in the entropy inequality is compared between the two solutions. Figures 18 - 21 are plots of the entropy inequality terms for both solutions at 25 mm downstream of the tube. Upon observation of these plots, the first, second and fourth terms of the inequality expression (4.1) stay negative. The third term is the cause of the entropy violations. This term takes into account the increase in entropy due to the chemical reactions, thus the reduced mechanism used has a direct effect on this term.

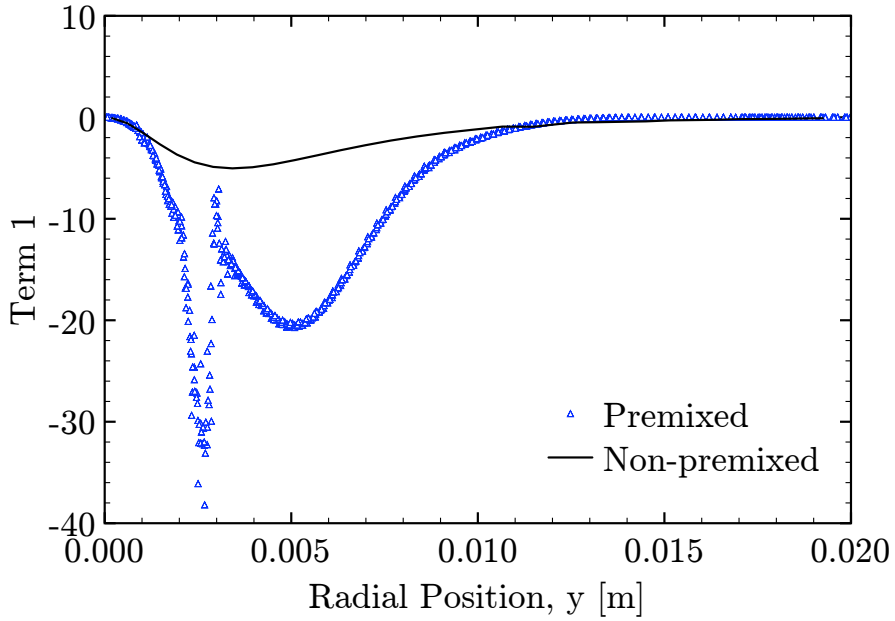

Figure 18. Term 1 vs. radius at 25 mm downstream for the premixed and non-premixed simulations.

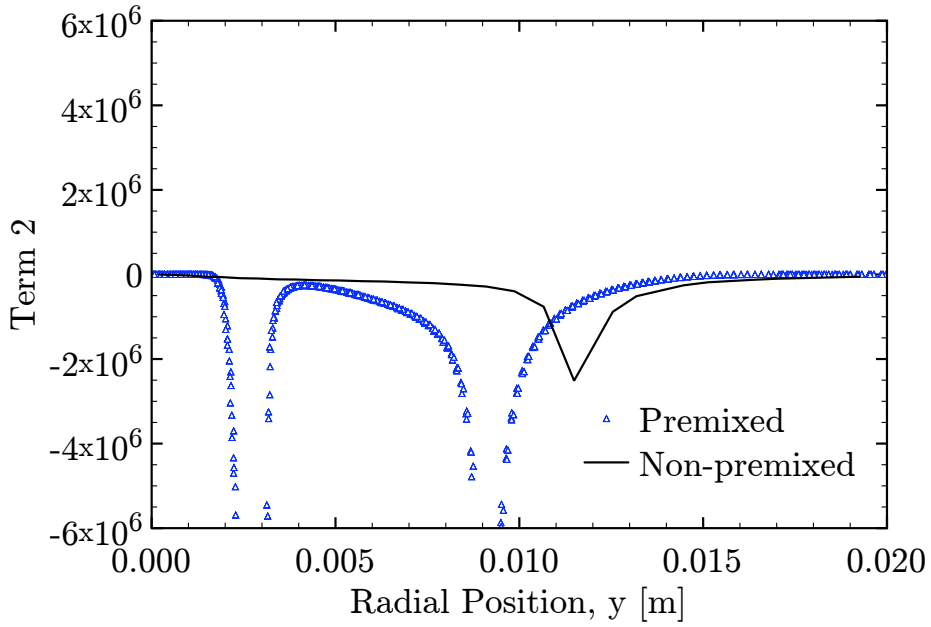

Figure 19. Term 2 vs. radius at 25 mm downstream for the premixed and non-premixed simulations.

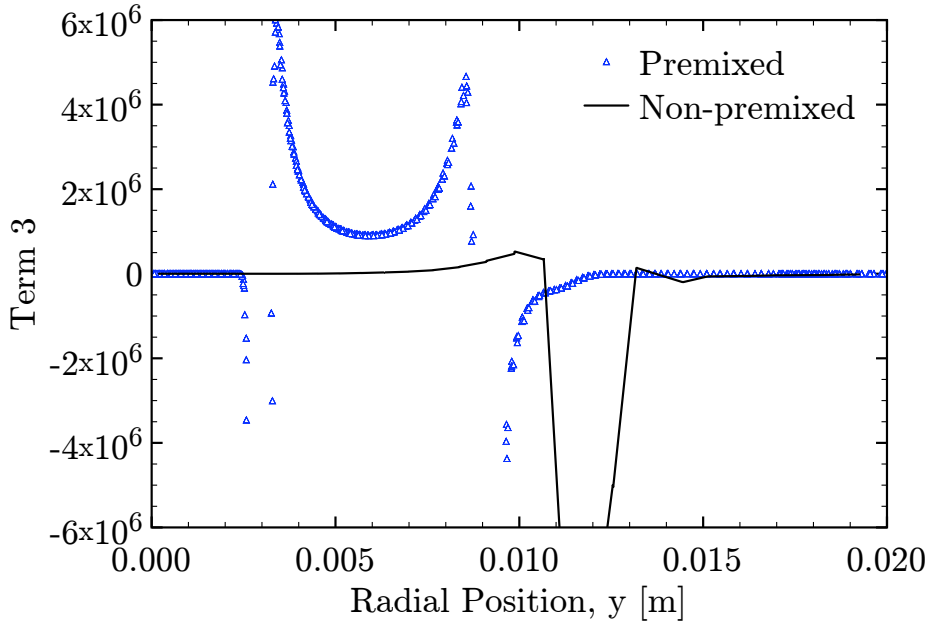

Figure 20. Term 3 vs. radius at 25 mm downstream for the premixed and non-premixed simulations.

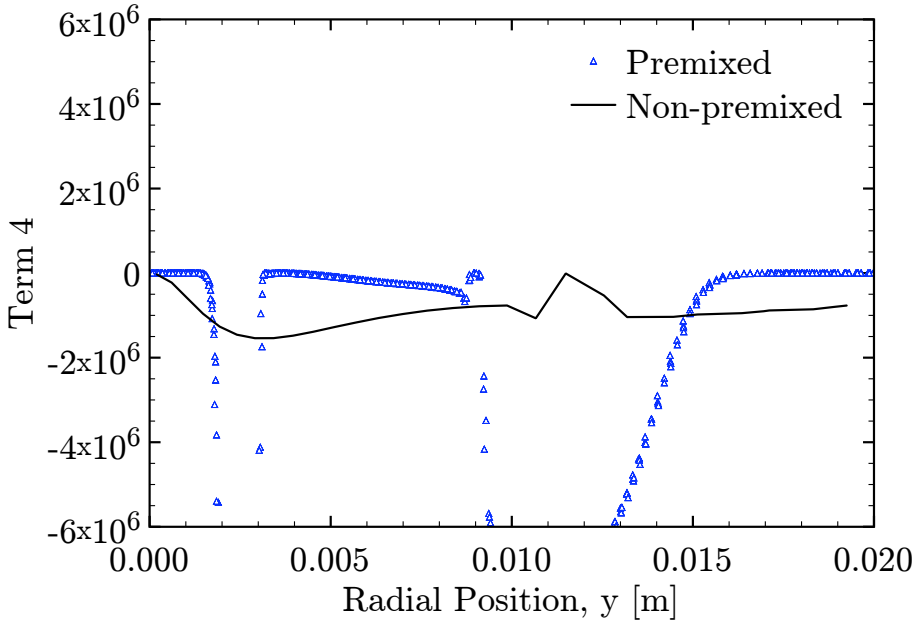

Figure 21. Term 4 vs. radius at 25 mm downstream for the premixed and non-premixed simulations.

Figure 22 is a plot of the sum of the four entropy inequality terms for both the premixed and non-premixed two-step methane combustion mechanism solutions. This plot indicates that the two-step methane combustion mechanism violates the second law of thermodynamics for both solutions, but the area experiencing the violations decreases significantly with the modified boundary condition.

Figure 23 displays the absolute differences in temperature and methane mass fraction contours. The differences between the premixed and non-premixed solutions reaches a maximum along the axisymmetric boundary. The maximum temperature difference is near the adiabatic flame temperature. This arises because the two simulations predict slightly different ignition points in the flow. The non-premixed case must mix longer with the co-flow than the premixed case to have ignition. This is because the premixed case already contains some oxygen in the fuel. This phenomena causes the ignition point to be farther downstream for the non-premixed case. Thus, when the premixed fuel has a high temperature due to ignition, the non-premixed case still predicts a temperature around 300 K. The high temperature difference near the tube along the axisymmetric boundary indicates this discrepancy. The methane mass fraction contour plot also shows a maximum difference along the axisymmetric boundary. The premixed solution predicts the extinction of methane before the non-premixed case.

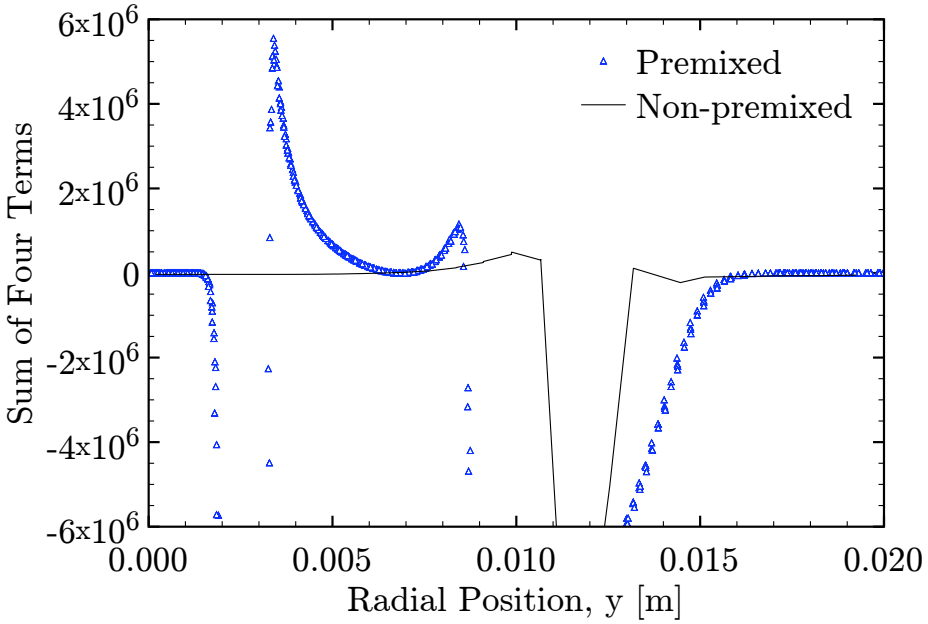

Figure 22. Entropy sum vs. radius at 25 mm downstream for the premixed and non-premixed simulations.

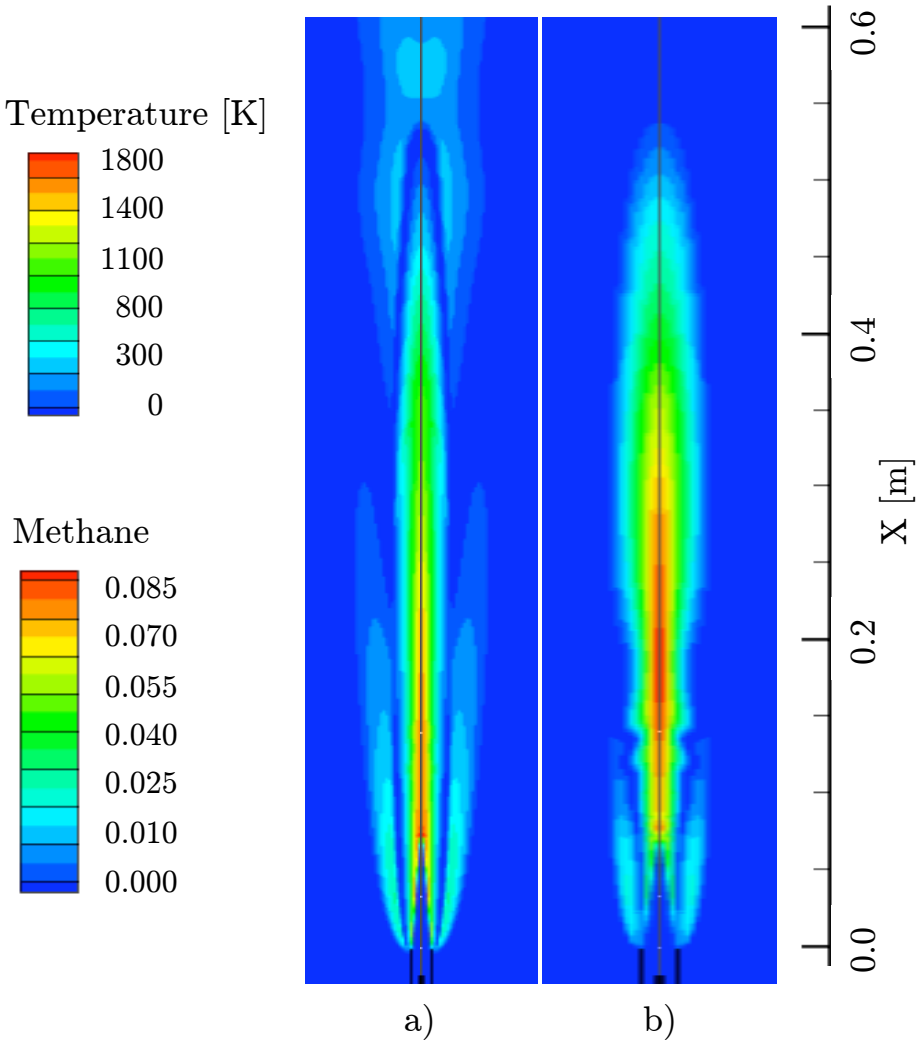

Figure 23. Two-step premixed and non-premixed comparison: a) absolute difference in temperature contour, b) absolute difference in methane mass fraction contour.

6.3 Numerical Simulation with Three-Step Mechanism

The results of the three-step methane combustion mechanism numerical simulation are presented in this section. A grid convergence study is presented, similar to the grid convergence study with the two-step methane combustion mechanism. The three-step methane combustion mechanism results are compared with the two-step methane combustion mechanism results with the modified boundary conditions.

In order to simulate the laminar methane-air flame with the three-step methane combustion mechanism the concentration of the fuel is modified by replacing the oxygen with nitrogen. The original boundary condition was causing the mixture to combust inside the fuel tube. Combustion inside the tube is not physical, because the mixture is too fuel rich to combust without mixing with the oxygen outside the tube. The modified inlet boundary conditions were shown in Table XI in the previous section.

A new grid convergence study was conducted for the three-step methane combustion mechanism with the modified boundary conditions. The same grids were used for this study as were used for the two-step methane combustion mechanism grid convergence study. The results of this study are plotted in Figs. 24 - 29, along with the experimental results from Flame A. The three-step methane combustion mechanism simulates the non-premixed problem, but matches the experimental measurements from the premixed Flame A well.

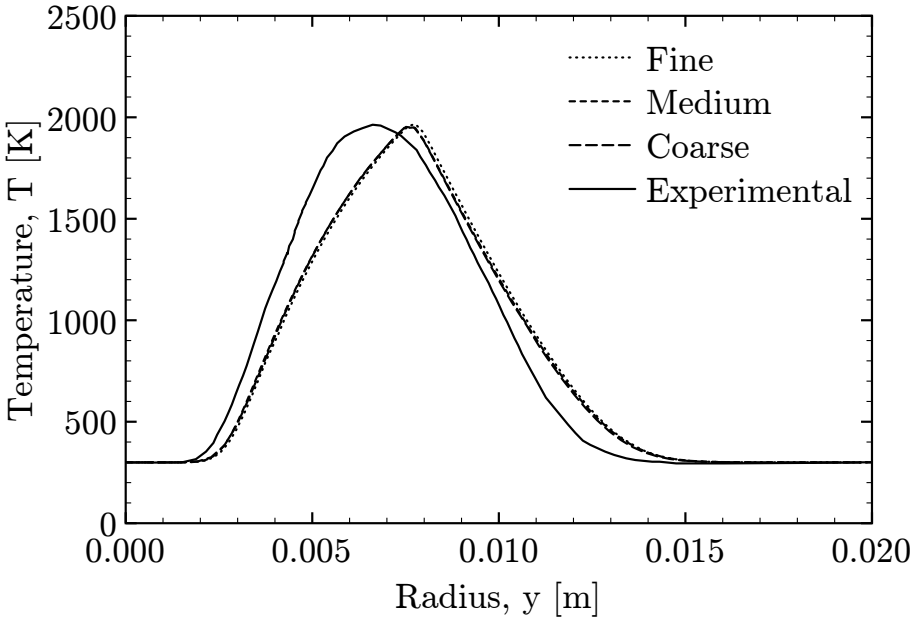

Figure 24. Temperature vs. radius at 25 mm downstream from the burner for the three-step methane combustion mechanism simulation.

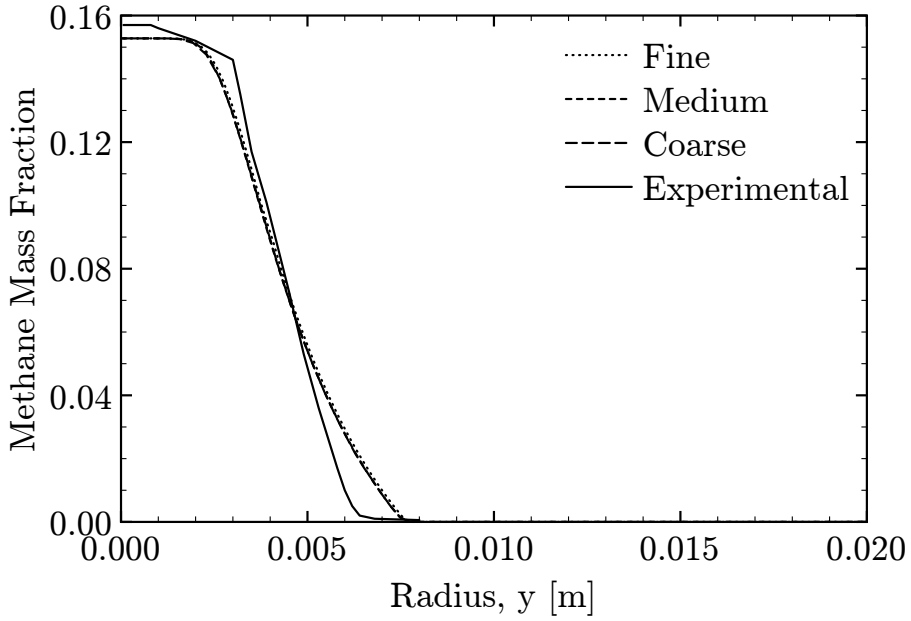

Figure 25. Methane mass fraction vs. radius at 25 mm downstream from the burner for the three-step methane combustion mechanism simulation.

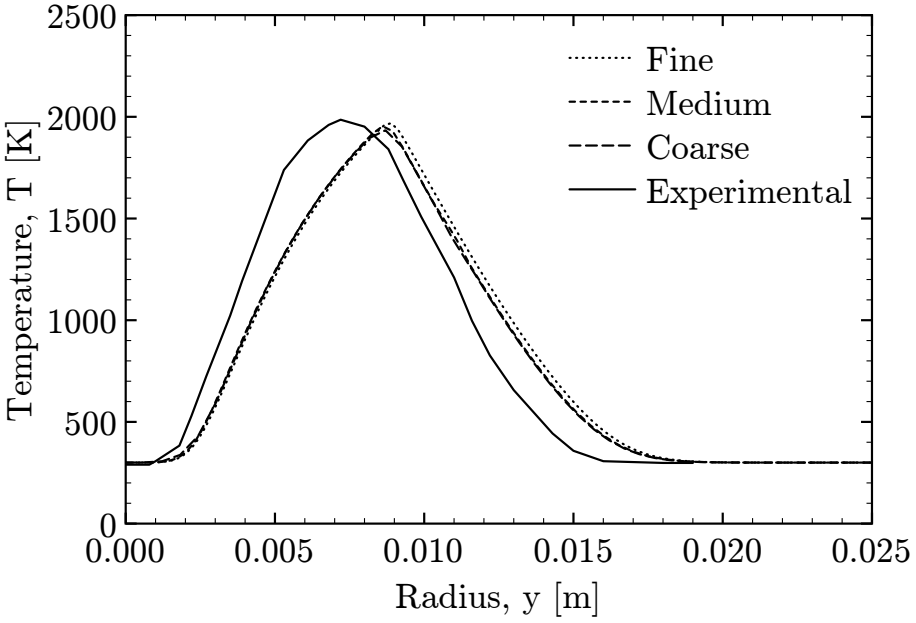

Figure 26. Temperature vs. radius at 50 mm downstream from the burner for the three-step methane combustion mechanism simulation.

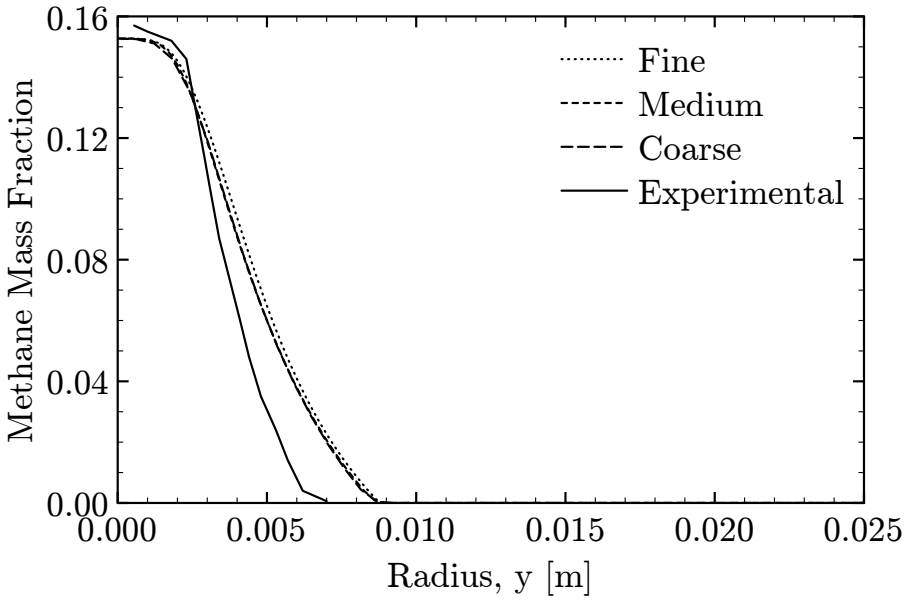

Figure 27. Methane mass fraction vs. radius at 50 mm downstream from the burner for the three-step methane combustion mechanism simulation.

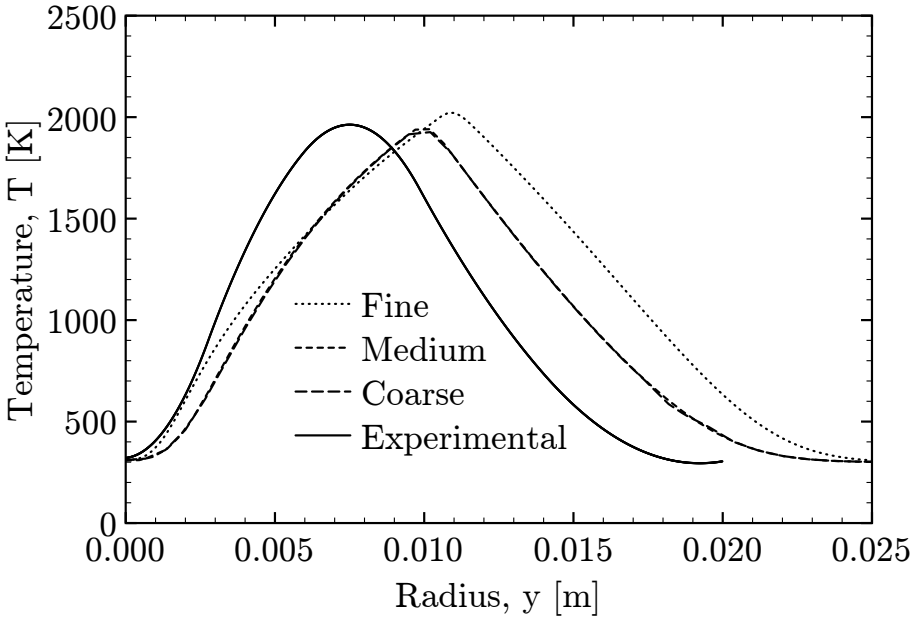

Figure 28. Temperature vs. radius at 100 mm downstream from the burner for the three-step methane combustion mechanism simulation.

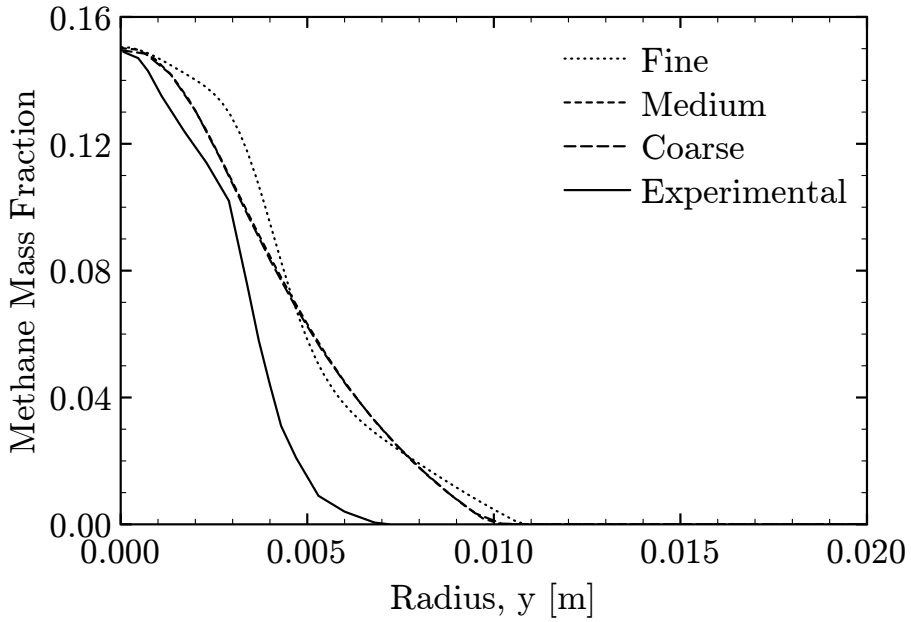

Figure 29. Methane mass fraction vs. radius at 100 mm downstream from the burner for the three-step methane combustion mechanism simulation.

6.4 Two- and Three-Step Mechanism Solution Comparisons

The two- and three-step methane combustion mechanism numerical simulations are compared by examining the temperature and methane mass fraction at 25, 50 and 100 mm downstream from the fuel tube. The results at these axial locations are plotted with the values from the Flame A experiment. The two- and three-step methane combustion mechanism solutions are also compared by examining the absolute differences in temperature and methane mass fraction throughout the domain.

Figures 30 - 35 show a comparison of the two- and three-step methane combustion mechanism solutions at each location downstream of the tube. The experimental data from Flame A are included on these figures for reference. Ironically, both mechanisms with the modified inlet boundary conditions match the experimental data better than the two-step methane combustion mechanism with the original boundary conditions, shown in Figs. 8 - 13.

Figures 30 - 35 show that the simulations are predicting a wider flame than the experimental data indicates. This is evident from the temperature profile; the peak is farther out radially and the temperature returns to 300 K farther away from the centerline than the experimental data. Once the fuel exits the tube, both the premixed and non-premixed problems turn are diffusion flames. In the pre-mixed fuel case, there is not enough oxygen in the fuel to combust, so the fuel must mix with the ambient air outside before combustion can occur. Likewise, for the non-premixed case the fuel must mix with the outside air. One should expect the non-premixed flame to be wider than the pre-mixed flame. The pre-mixed fuel must mix with less air to find enough oxygen to combust than the non-premixed, because oxygen is already present in the mixture. The non-premixed fuel must mix with more of the outside air, resulting in a wider mixing area before ignition. The results from the simulations

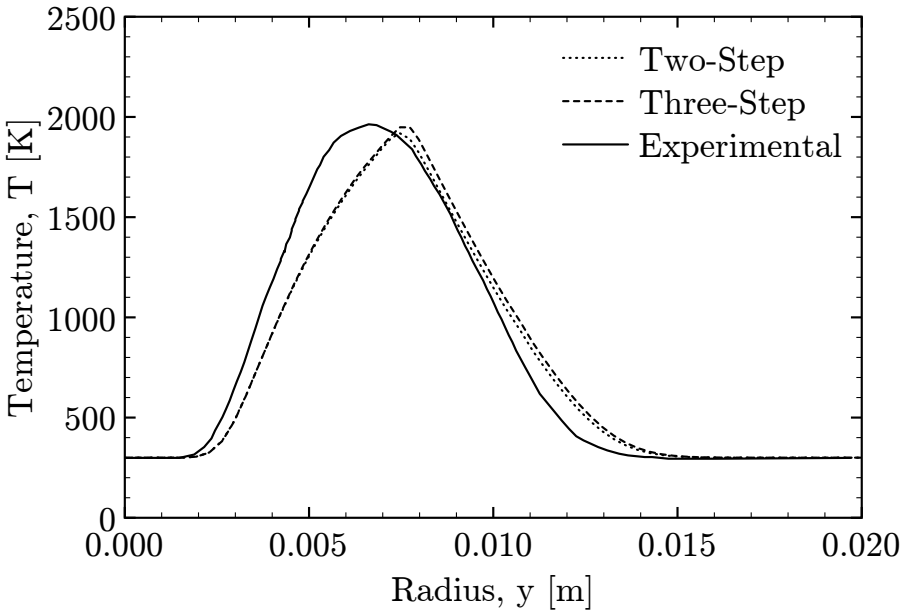

Figure 30. Temperature vs. radius at 25 mm downstream from the burner for the two- and three-step methane combustion mechanism simulation with non-premixed fuel.

support this theory.

The two simulations are compared by examining the normalized difference in the temperature and the absolute difference in the methane mass fraction throughout the domain. This yields a 19% maximum difference in temperature between the two simulations, which is equivalent to a difference of 386 K. The maximmum difference in methane mass fraction was 0.018. The differences in these two distributions are plotted in Fig. 36. The maximum differences are occurring at the axisymmetric boundary. The temperature contour indicates the maximum difference is occurring at the end of the flame downstream from the tube. The methane mass fraction plot however, shows that the methane mass fraction is predicted similarly for both simulations.

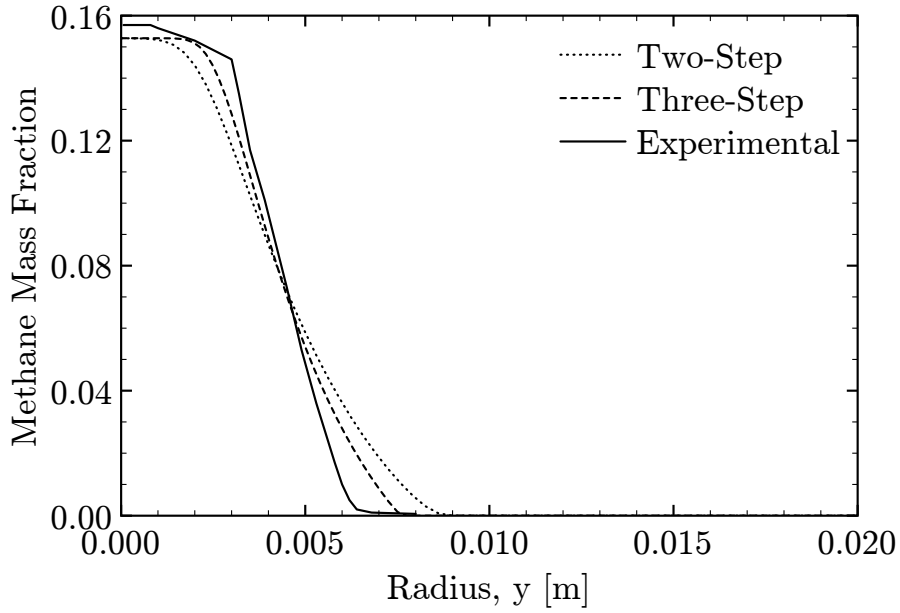

Figure 31. Methane mass fraction vs. radius at 25 mm downstream from the burner for the two- and three-step methane combustion mechanism simulation with non-premixed fuel.

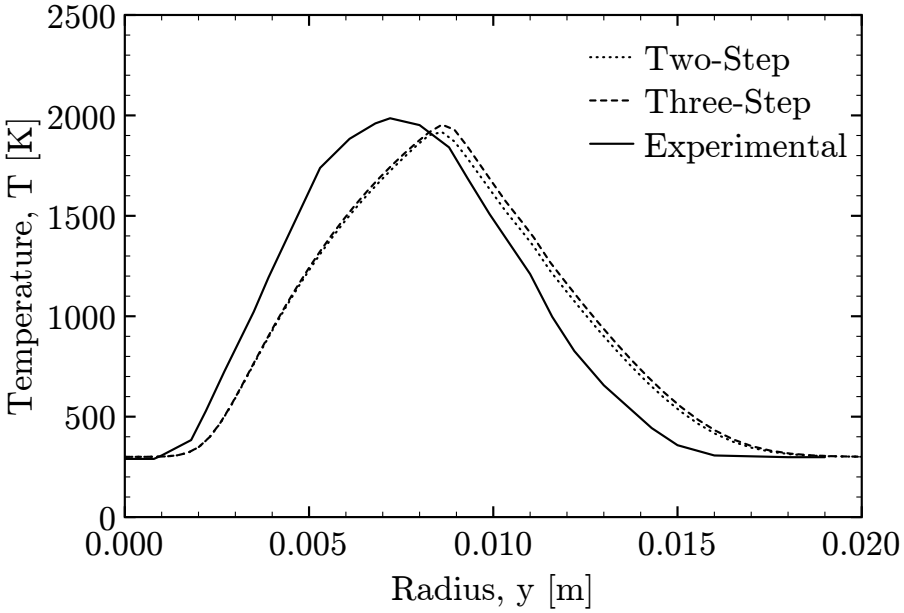

Figure 32. Temperature vs. radius at 50 mm downstream from the burner for the two- and three-step methane combustion mechanism simulation with non-premixed fuel.

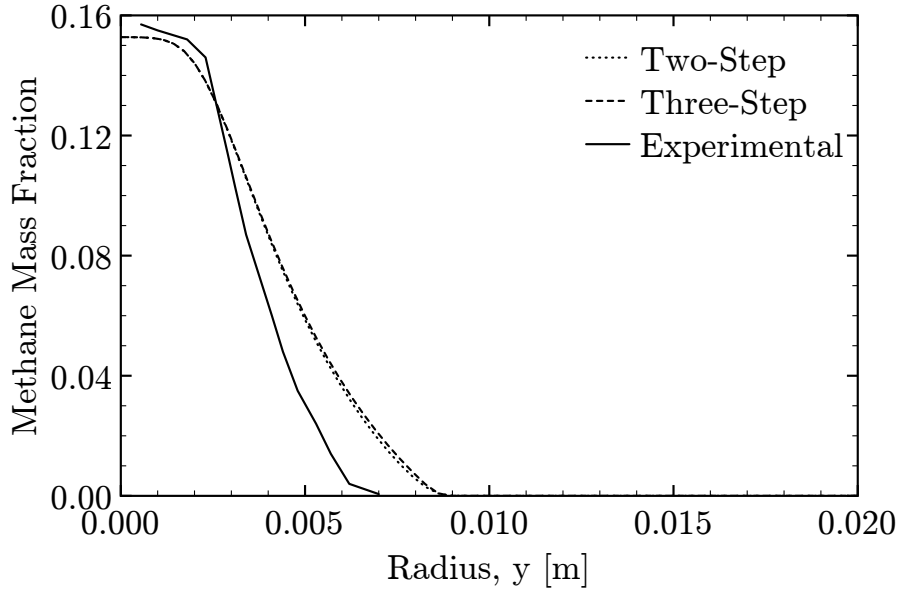

Figure 33. Methane mass fraction vs. radius at 50 mm downstream from the burner for the two- and three-step methane combustion mechanism simulation with non-premixed fuel.

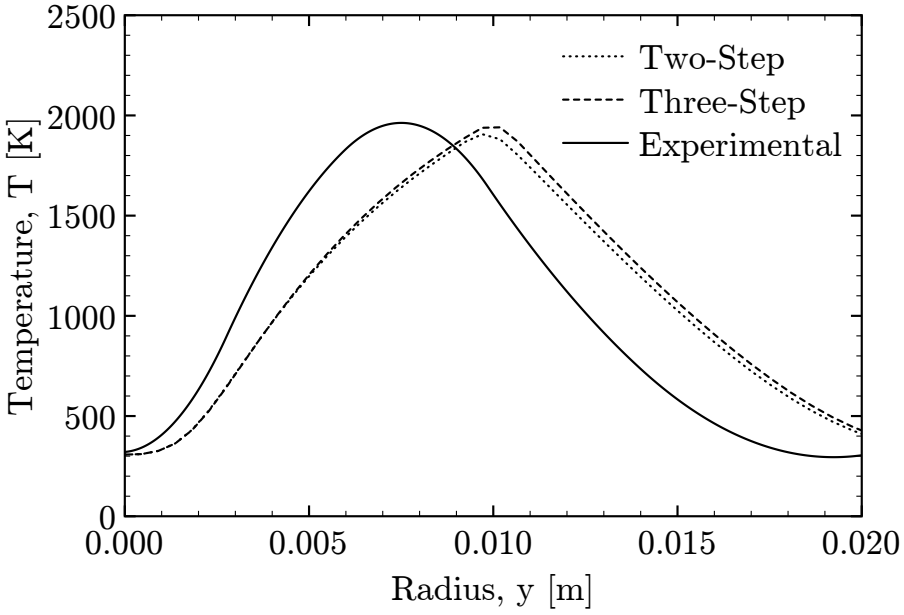

Figure 34. Temperature vs. radius at 100 mm downstream from the burner for the two- and three-step methane combustion mechanism simulation with non-premixed fuel.

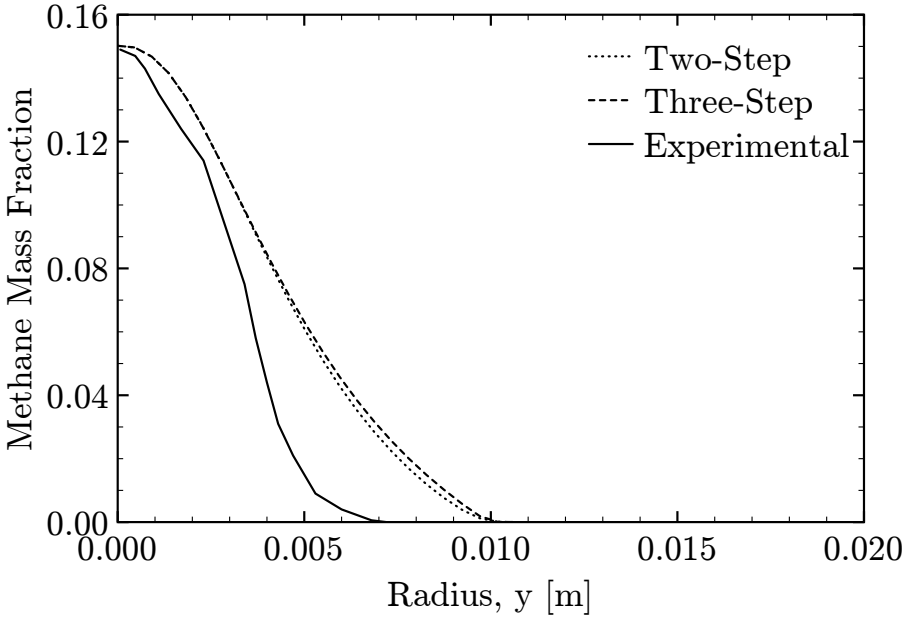

Figure 35. Methane mass fraction vs. radius at 100 mm downstream from the burner for the two- and three-step methane combustion mechanism simulation with non-premixed fuel.

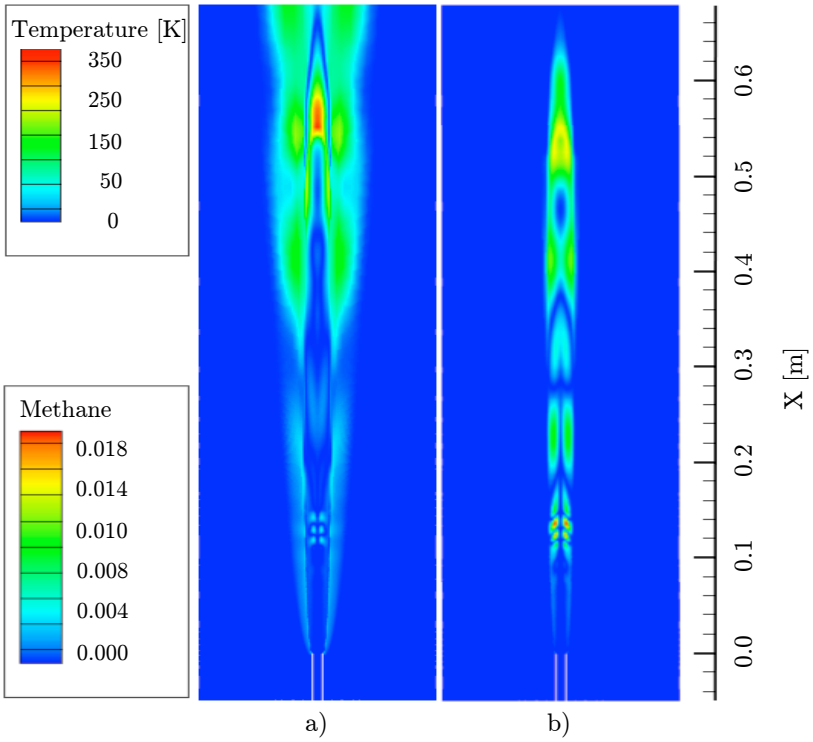

Figure 36. Two- and three-step mechanism non-premixed solution comparison: a) absolute difference in temperature contour, b) absolute difference in methane mass fraction contour.

The two-step methane combustion mechanism solution yielded 273 cells that violated the entropy inequality, while the three-step methane combustion mechanism simulation did not produce any cells that violated the entropy inequality. The three-step mechanism simulation also did not require a temperature limiter like the two-step mechanism simulation required. The temperature limiter in FLUENT was investigated, and a correlation was found between the limiter and violations of the entropy inequality [45, pp. 12-13]. The temperature limiter was in effect much less in the simulation with the modified boundary condition than in the simulation with the original conditions, as discussed earlier in the chapter.

6.5 Two-Step Mechanism Modifications/Development

Modifications are made to the two-step methane combustion mechanism introduced by Westbrook and Dryer. The concentrations of the five major species in the detailed reaction simulation are matched to develop the new Arrhenius parameters. The concentrations come from running Cantera with the GRI-3.0 mechanism. The procedure is discussed in detail and the limitations of this approach are emphasized.

6.5.1 Curve-Fitting Procedure

The two-step methane combustion mechanism from Westbrook and Dryer was developed by matching the flame speed at an equivalence ratio of one, and extrapolating to other equivalence ratios. A different approach is to match the structure of the flame. The structure of a one dimensional laminar flame consists of the concentrations before and after the flame front. This can be illustrated graphically by plotting the concentrations of each of the five major species and the temperature versus distance. Figure 37 shows the concentrations and temperature for the one-dimensional flame

calculation in Cantera. The objective is to vary the parameters in the Arrhenius

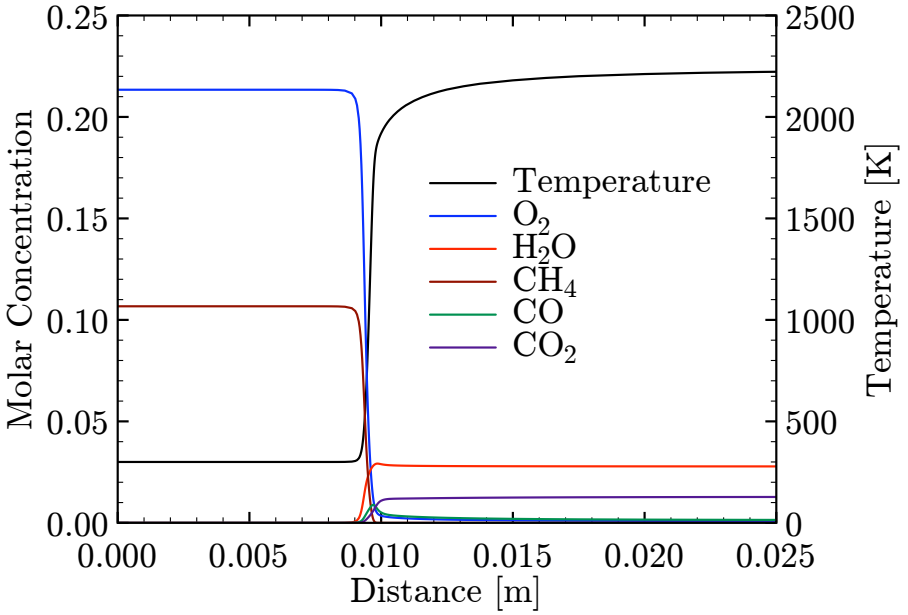

Figure 37. Molar concentrations of the five major species in methane-air combustion and temperature versus distance for a one dimensional laminar flame.

rates to match the change in the concentrations in Figure 37. The reaction equations are revisited for clarity. The Arrhenius rates for the two-step methane reaction mechanism are

$$k_1 = A_1 T^{\beta_1} \exp \frac{-E_1}{RT}$$
$$k_{2f} = A_{2f} T^{\beta_{2f}} \exp \frac{-E_{2f}}{RT}$$
$$k_{2b} = A_{2b} T^{\beta_{2b}} \exp \frac{-E_{2b}}{RT}$$

where T is temperature, R is the universal gas constant, and A, β, and E are the Arrhenius parameters. The Arrhenius rates determine the rate of progress of each

reaction. For the two-step mechanism the rates of progress are expressed as

$$\omega_1 = k_1[\mathrm{CH_4}][\mathrm{O_2}]^{1.5}$$

$$\omega_{2f} = k_{2f}[\mathrm{CO}][\mathrm{O_2}]^{0.5}$$

$$\omega_{2b} = k_{2b}[\mathrm{CO_2}]$$

where ω is the rate of progress and [s] represents the concentration of species s. The exponents of the concentrations are set to the stoichiometric coefficients. Generally, for detailed reaction mechanisms the stoichiometric coefficients are used for the reaction exponents. Westbrook and Dryer varied the reaction exponents to match flame speed. For this development, the exponents are set and all three Arrhenius parameters are varied to match the concentrations from Cantera. The rates of progress determine the rate of production/destruction for each species. For the two-step methane combustion mechanism the rates are written as

$$\dot{w}_{\mathrm{CH_4}} = -\omega_1$$

$$\dot{w}_{\mathrm{O_2}} = -1.5\ \omega_1 - 0.5\ \omega_{2f} + 0.5\ \omega_{2b}$$

$$\dot{w}_{\mathrm{CO}} = \omega_1 - \omega_{2f} + \omega_{2b}$$

$$\dot{w}_{\mathrm{H_2O}} = 2\ \omega_1$$

$$\dot{w}_{\mathrm{CO_2}} = \omega_{2f} - \omega_{2b}$$

where $\dot{w}_i$ is the rate of production/destruction of species i. The rates of progress are multiplied by the stoichiometric coefficients for each species, with a negative sign for a species in the reactants and a positive sign for a species in the products. The negative stands for a species consumed by the reaction, while a positive sign represents a species produced by the reaction. The only unknowns in the rate of production/destruction

of each species are the Arrhenius rates, k_1, k_{2f} and k_{2b}. Each of these rates have three parameters, A, β, and E, giving a total of nine parameters that can be set to match the change in concentrations from Cantera. A nonlinear Gauss-Newton least squares algorithm is used to solve for the parameters that best match the data from Cantera. An example of this method is given for the first reaction. The methane and water concentrations are only effected by the first reaction. Thus, the three parameters in the first reaction are used to match the methane and water concentrations. The algorithm begins with an initial guess, from which the rates of production/destruction are computed. Then a jacobian matrix is computed. This matrix is made up of the derivatives of the production rates, written for the methane production rate as

$$J_{i,j} = \frac{\mathrm{d}\dot{w}_{\mathrm{CH_4},i}}{\mathrm{d}y_j}$$

where y_j are the Arrhenius parameters, A, β and E. The i index represents the x location from the Cantera data. The jacobian matrix was constructed to match the methane concentration as

$$J_{i,1} = \frac{\dot{w}_{\mathrm{CH_4},i}}{A_1}$$

$$J_{i,2} = \dot{w}_{\mathrm{CH_4},i} \ln T_i$$

$$J_{i,3} = \frac{-\dot{w}_{\mathrm{CH_4},i}}{RT_i}$$

which forms a matrix of the number of equations by three. The right hand side of the system is composed of a residual defined as the exact solution from Cantera minus the approximated solution. The approximated solution is solved using a simple Taylor series expansion. The expansion is rearranged to form

$$[\mathrm{CH_4}]_{i,approx} = [\mathrm{CH_4}]_{i-1} + (x_i - x_{i-1})\dot{w}_{\mathrm{CH_4},i}.$$

With this approximate methane concentration the residual is defined as

$$r_i = [\mathrm{CH_4}]_i - [\mathrm{CH_4}]_{i,approx}.$$

The transpose of J is pre-multiplied by the system of equations, the same as the traditional least squares technique. This leads to a system of equations with three equations and three unknowns. The system is written as

$$\underline{\underline{J}}^T \underline{\underline{J}} \vec{y}_s = \underline{\underline{J}}^T \vec{r}.$$

The solution y_s, is then added to the initial guess, and the iterative process starts over. A relaxation factor is recommended. This method diverged almost immediately without a strict relaxation factor. The relaxation factor is applied by

$$\vec{y} = \vec{y} + \gamma \vec{y}_s$$

where γ is the relaxation factor. The downside to this approach is the initial guess must be close to the correct answer. If the initial guess is bad this method may diverge or converge towards a solution that is wrong. In order to get the initial guess a shotgun technique was used. For this technique a max and min value was chosen for each variable, and an evenly spaced grid was laid out between these values. Every possible combination of the values for each parameter on the grid were used to calculate the residual. The combination that produces the minimum residual was used as the initial guess for the nonlinear least squares method. The result for matching the methane concentration is shown in Fig. 38, along with the result from the Westbrook and Dryer mechanism and the exact solution from Cantera. The reaction mechanism produced from matching the methane concentration is referred to as the Mech 1 mechanism. Figure 39 shows the resulting water concentration from matching the methane concentration. The water concentration in the Mech 1 mechanism predicts

a much larger increase than the exact solution from Cantera.

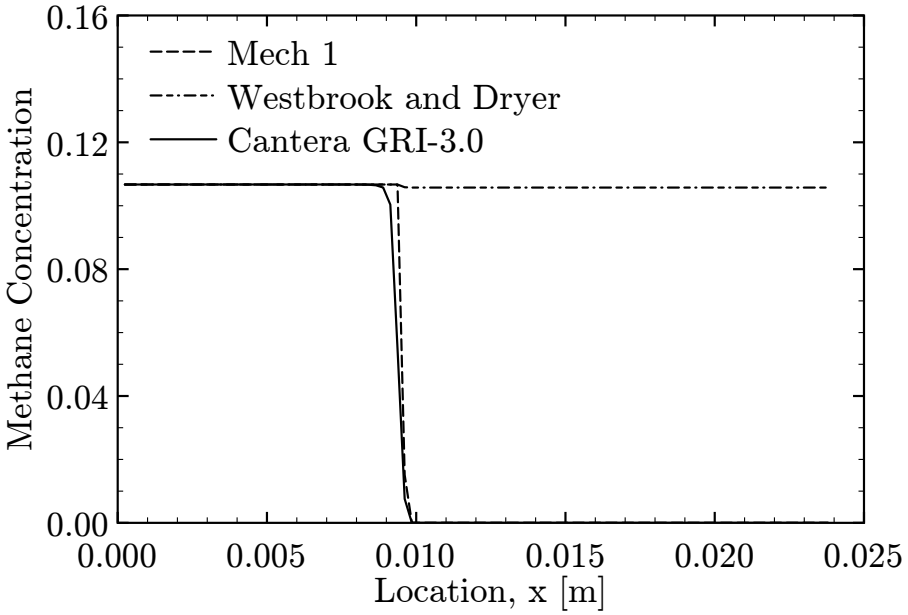

Figure 38. Methane concentration vs. distance for the exact Cantera solution, the Mech 1 solution, and Westbrook and Dryer's two-step mechanism.

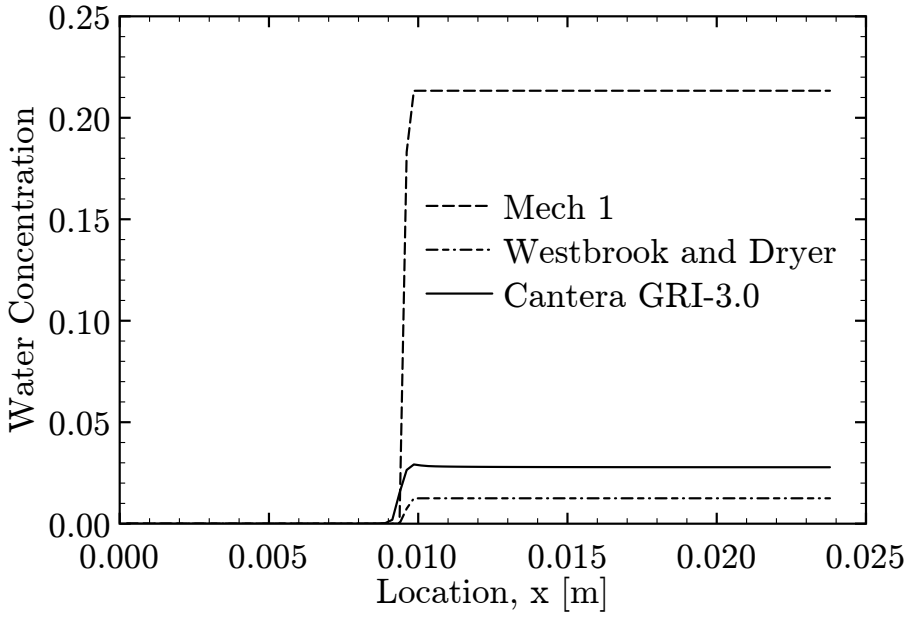

Figure 39. Water concentration vs. distance for the exact Cantera solution, the Mech 1 solution, and Westbrook and Dryer's two-step mechanism.

The Mech 1 mechanism predicts a much larger increase in the water concentration than the exact solution from Cantera. This prediction should be expected upon inspecting the reaction. The first reaction in the two-step mechanism is

$$CH_4 + 1.5\ O_2 \rightarrow CO + 2\ H_2O.$$

This reaction states that for every mole of CH_4 consumed, two moles of H_2O are produced. Therefore, the decrease in the methane concentration in Fig. 38 is equal to half of the increase in the water concentration in Fig. 39. The alternative is to match the water concentration with the first Arrhenius expression, which leads to Figs. 40 - 41. Once again, the decrease in the methane is about half the increase in the water. This mechanism, Mech 2, predicts a much smaller decrease in the methane concentration than the exact solution from Cantera. The two-step methane combustion mechanism from Westbrook and Dryer does not predict the consumption of methane well. The methane concentration only decreases slightly before leveling off after the flame front. The water concentration however, is predicted much better by the two-step methane combustion mechanism from Westbrook and Dryer.

The second reaction, both forward and backward, is used to match the oxygen concentration. The Arrhenius parameters are calculated using the same algorithm described with the first reaction. The only difference is the nonlinear least squares technique solves for six unknowns, instead of three. The six unknowns are the Arrhenius parameters A, β, and E for both the forward and reverse rates for reaction two. Figures 42 - 44 show the concentrations predicted for O_2, CO, and CO_2. The parameters for the second reaction are used for both the Mech 1 and Mech 2 mechanisms. The two-step mechanism from Westbrook and Dryer does not match the concentrations of O_2, CO, and CO_2, as can be seen in Figs. 42 - 44.

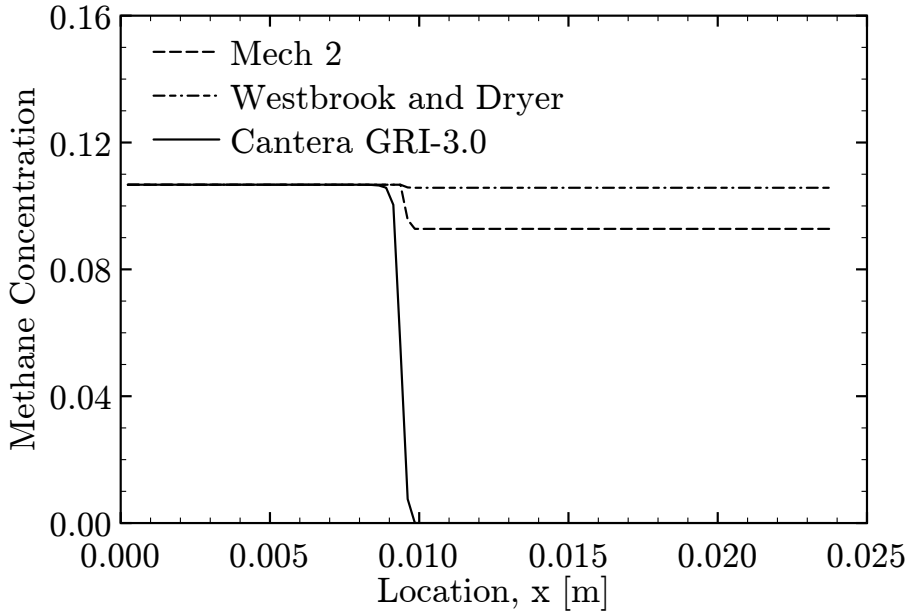

Figure 40. Methane concentration vs. distance for the exact Cantera solution, the Mech 2 solution, and Westbrook and Dryer's two-step mechanism.

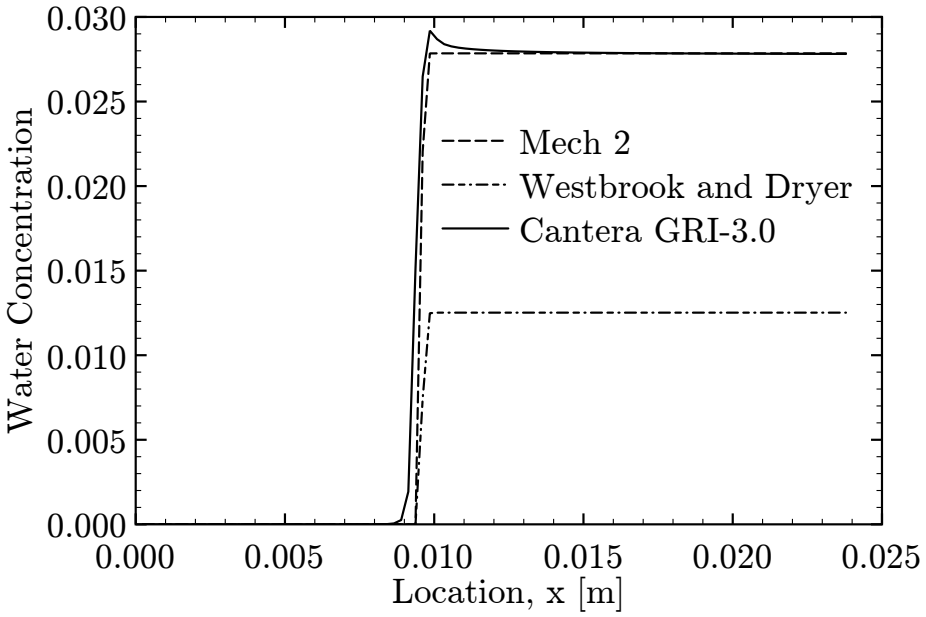

Figure 41. Water concentration vs. distance for the exact Cantera solution, the Mech 2 solution, and Westbrook and Dryer's two-step mechanism.

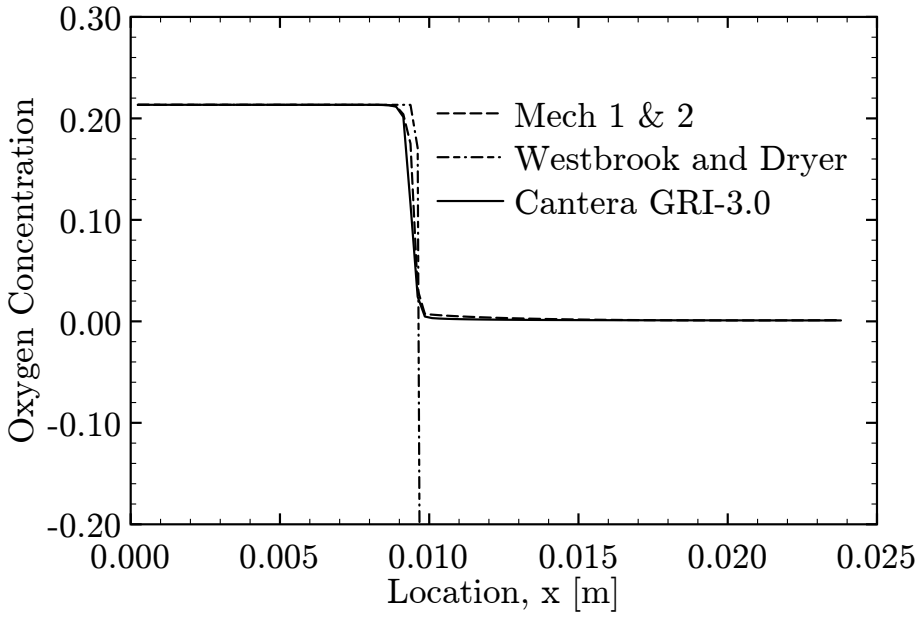

Figure 42. Oxygen concentration vs. distance for the exact Cantera solution, the Mech 1 and 2 solutions, and Westbrook and Dryer's two-step mechanism.

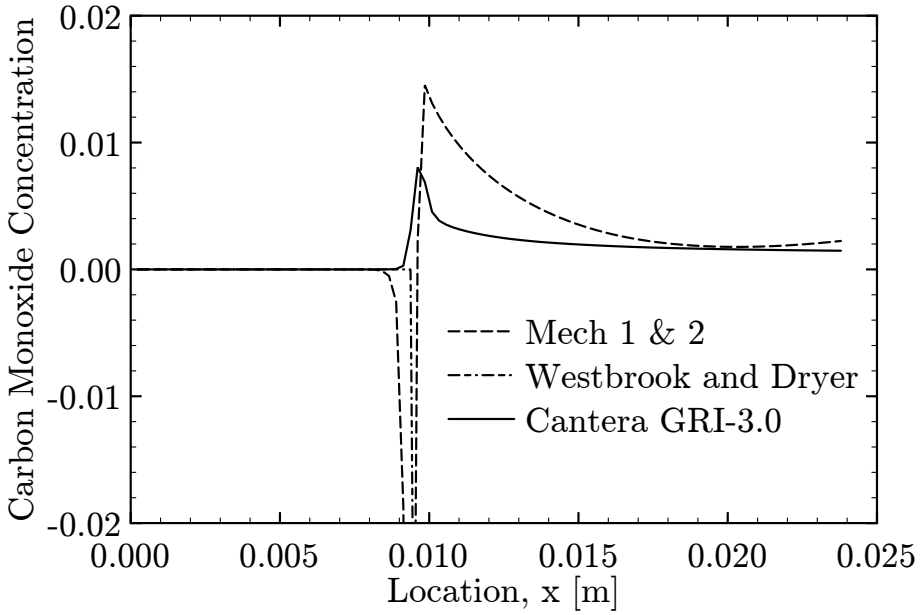

Figure 43. Carbon monoxide concentration vs. distance for the exact Cantera solution, the Mech 1 and 2 solutions, and Westbrook and Dryer's two-step mechanism.

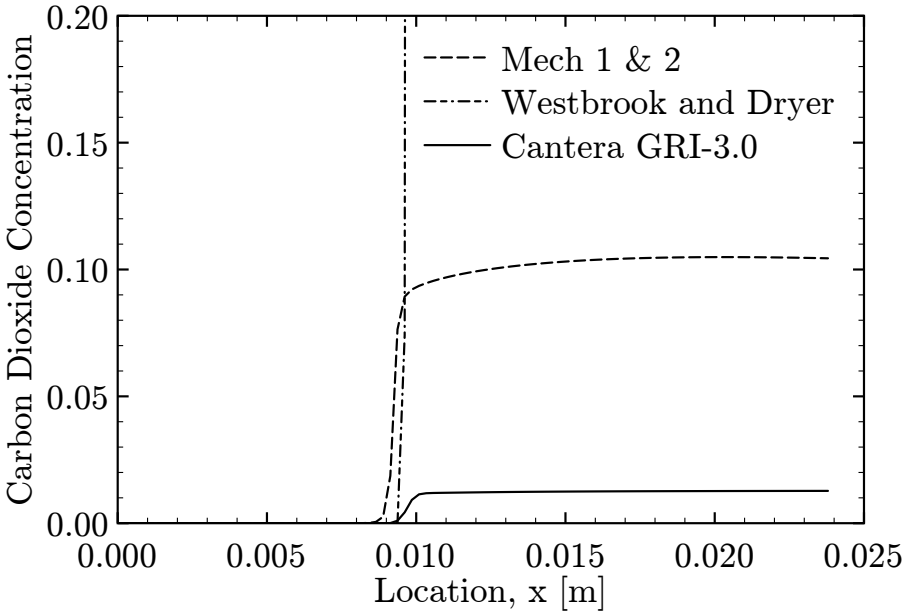

Figure 44. Carbon dioxide concentration vs. distance for the exact Cantera solution, the Mech 1 and 2 solutions, and Westbrook and Dryer's two-step mechanism.

6.5.2 Mech 1 and Mech 2 Methane Combustion Mechanism Results

The Arrhenius parameters for the both the first and second reactions of the Mech 1 mechanism are shown in Table XII. The parameters for the Mech 2 mechanism are in Table XIII. The only differences between these mechanisms are the Arrhenius parameters used in the first reaction. The Mech 1 mechanism contains the parameters in the first reaction used to match the methane concentration, and the Mech 2 mechanism contains the parameters used to match the water concentration.

Table XII. Mech 1 Methane Combustion Mechanism

Reaction	A	β	E
1	3.2926×10^8	2.2414	2.2888×10^8
2_f	6.8573×10^6	-0.6022	-9.0211×10^4
2_b	1.4286×10^9	2.8571	7.1429×10^8

Arrhenius parameters for the Mech 1 mechanism, units of E are in J/kmol.

Table XIII. Mech 2 Methane Combustion Mechanism

Reaction	A	β	E
1	4.8355×10^8	2.3077	2.5117×10^8
2_f	6.8573×10^6	-0.6022	-9.0211×10^4
2_b	1.4286×10^9	2.8571	7.1429×10^8

Arrhenius parameters for the Mech 2 mechanism, units of E are in J/kmol.

Figures 45 and 46 are plots of the temperature contours from the flames produced by the Mech 1 and Mech 2 mechanisms, respectively. Both simulations were conducted in FLUENT using the Soret thermal diffusion coefficient in (6.1).

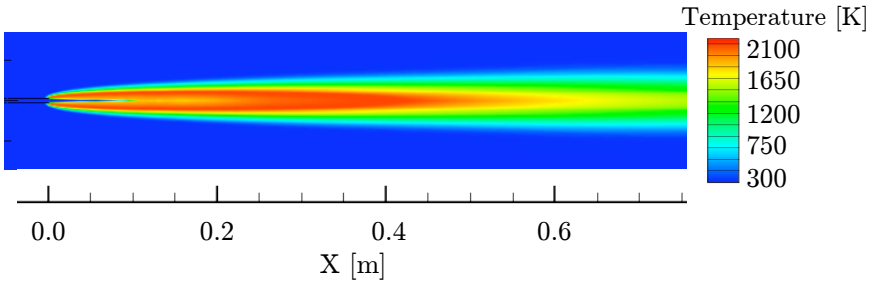

Figure 45. Contour plot of temperature for the laminar methane-air flame produced by the Mech 1 mechanism.

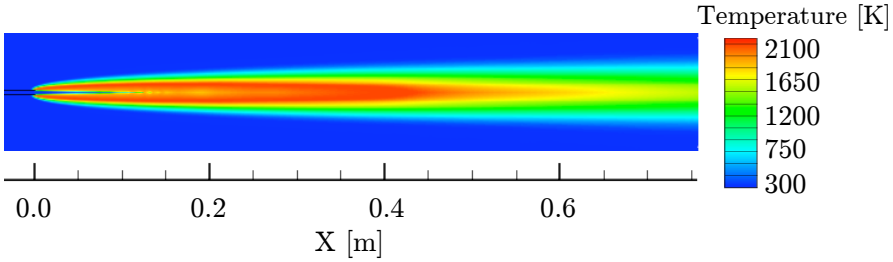

Figure 46. Contour plot of temperature for the laminar methane-air flame produced by the Mech 2 mechanism.

The solutions produced by the Mech 1 and Mech 2 methane combustion mechanisms are compared by examining the absolute differences in temperature and methane mass fraction throughout the domain. The new mechanism solutions are compared against the solution from Westbrook and Dryer's two-step methane combustion mechanism, and compared against each other. Figure 47 shows the contours for the differences in temperature and methane mass fraction for the Mech 1 and Westbrook and Dryer mechanisms. Figure 48 shows the contours for the differences in temperature and methane mass fraction for the Mech 2 and Westbrook and Dryer mechanisms, on the same scales as Fig. 47. The maximum differences are similar, but the Mech 2 mechanism has a wider region of differences than the Mech 1 mechanism. Figure 49 shows the contour plots of the differences for temperature and methane mass fraction for the Mech 1 and Mech 2 mechanisms, also on the same scale as Figs. 47 and 48. The maximum temperature difference between Mech 1 and Mech 2 is 1350 K, while the maximum temperature difference between the new mechanisms and the Westbrook and Dryer mechanism is over 1700 K. The Mech 2 mechanism produces differences further downstream with the Westbrook and Dryer mechanism, than the Mech 1 mechanism. Discrepancies such as this should be expected in the region where reactions are taking place, because the Mech 1 and Mech 2 mechanisms were designed to match different flame structures. After the reactions have taken place, the solutions downstream from the reaction zone become very similar. The hot reaction region is where the entropy violations occur with the Mech 1 mechanism.

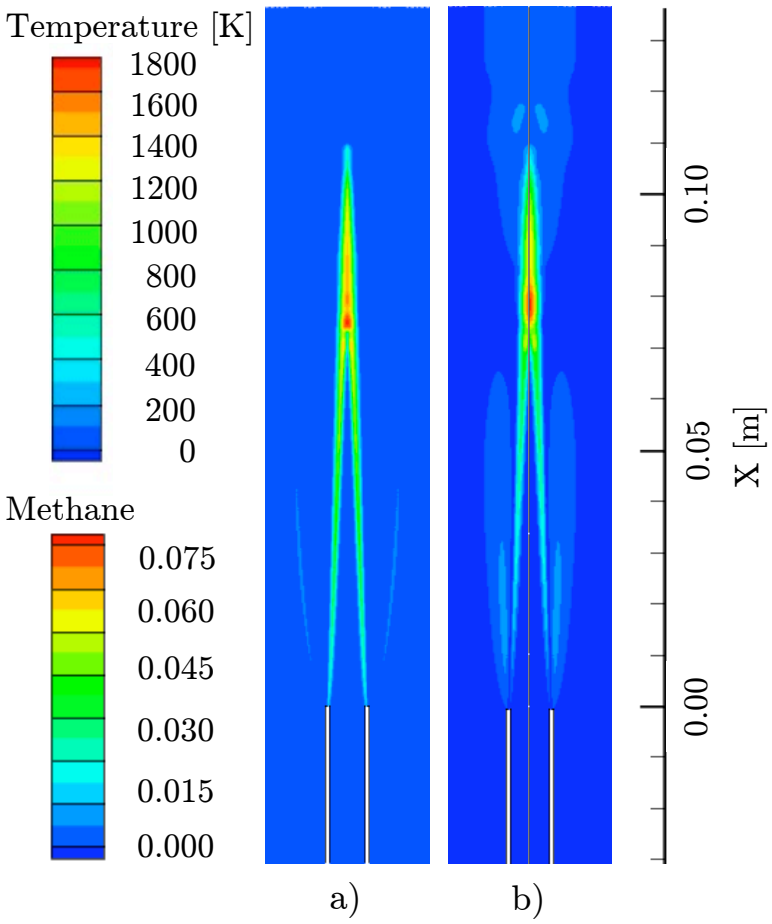

Figure 47. Mech 1 and Westbrook and Dryer solution comparison: a) absolute difference in temperature contour, b) absolute difference in methane mass fraction contour.

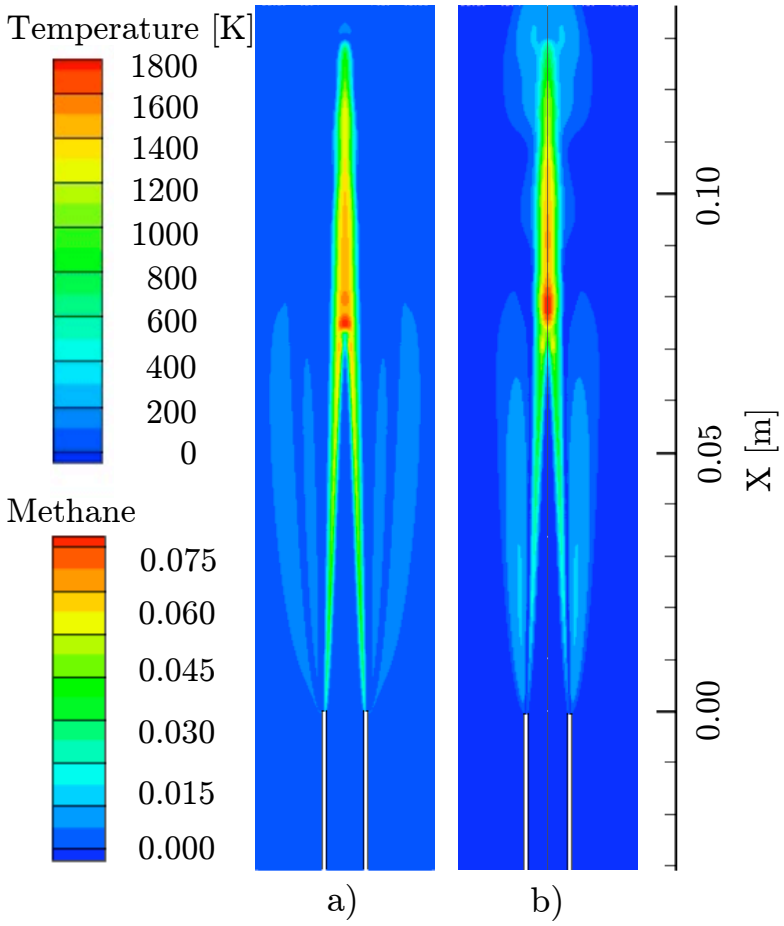

Figure 48. Mech 2 and Westbrook and Dryer solution comparison: a) absolute difference in temperature contour, b) absolute difference in methane mass fraction contour.

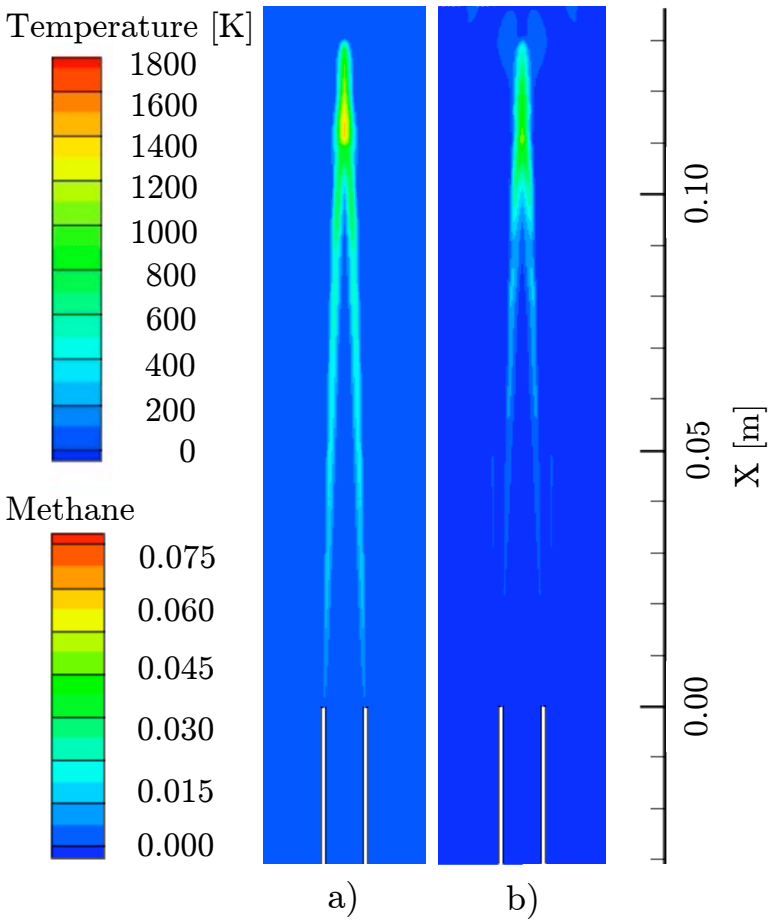

Figure 49. Mech 1 and Mech 2 solution comparison: a) absolute difference in temperature contour, b) absolute difference in methane mass fraction contour.

The results at 25, 50 and 100 mm downstream from the tube for the new mechanisms are compared with the results from Westbrook and Dryer's two-step methane combustion mechanism and the experimental data in Figs. 50-55. The temperature plots, Figs. 50, 52 and 54, show that the new mechanisms predict narrower profiles than the Westbrook and Dryer mechanism. The narrower profiles are closer to the experimental data. The Mech 2 mechanism predicts a flame width that is closer to the experimental data than the Mech 1 mechanism. The methane mass fraction plots, Figs. 51, 53 and 55, indicate that the new mechanisms predict a methane profile that is closer to the experimental data than the Westbrook and Dryer mechanism. The new mechanisms predict very similar methane mass fraction plots at each location.

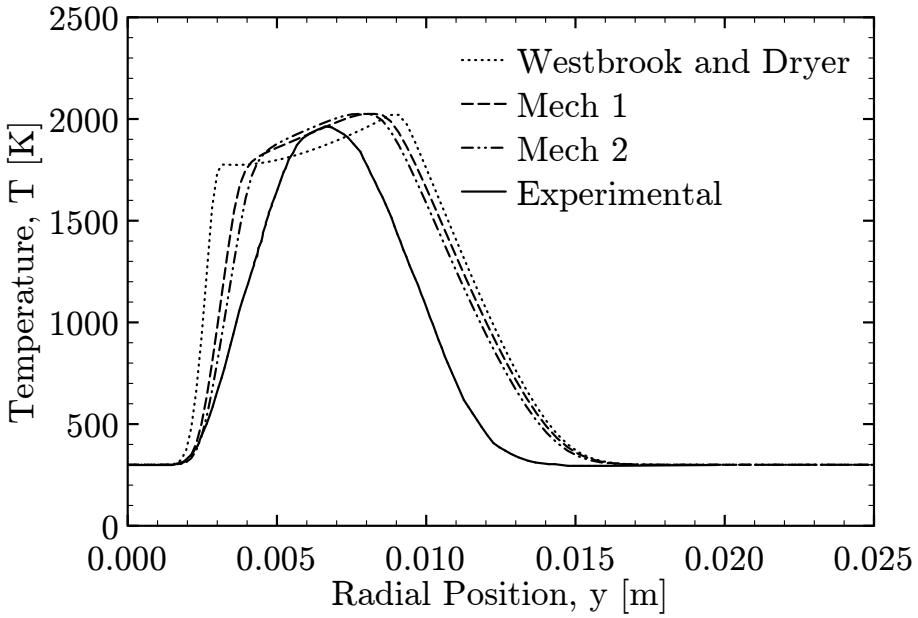

Figure 50. Temperature vs. radius: Mech 1, Mech 2 and Westbrook and Dryer methane combustion mechanism solutions at 25 mm downstream from the tube.

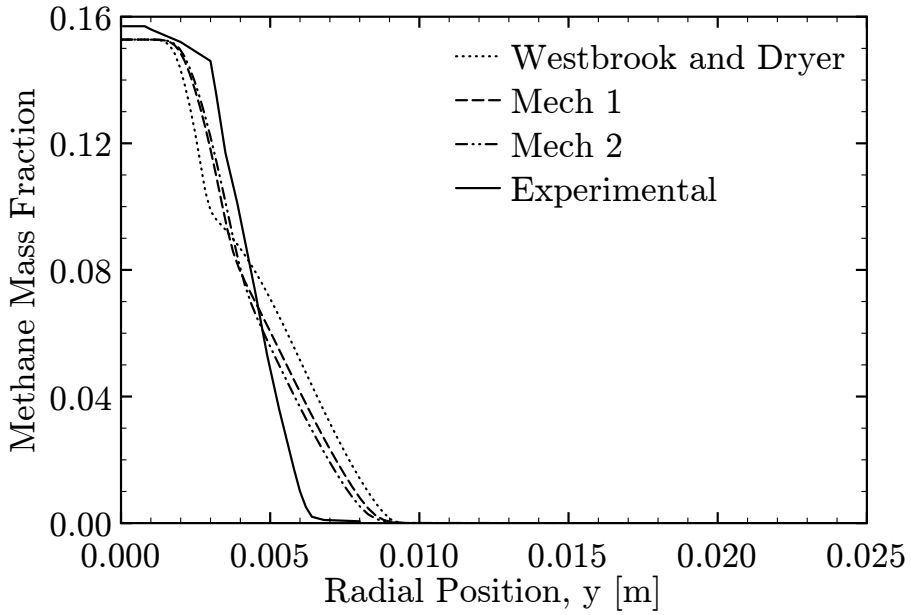

Figure 51. Methane mass fraction vs. radius: Mech 1, Mech 2 and Westbrook and Dryer methane combustion mechanism solutions at 25 mm downstream from the tube.

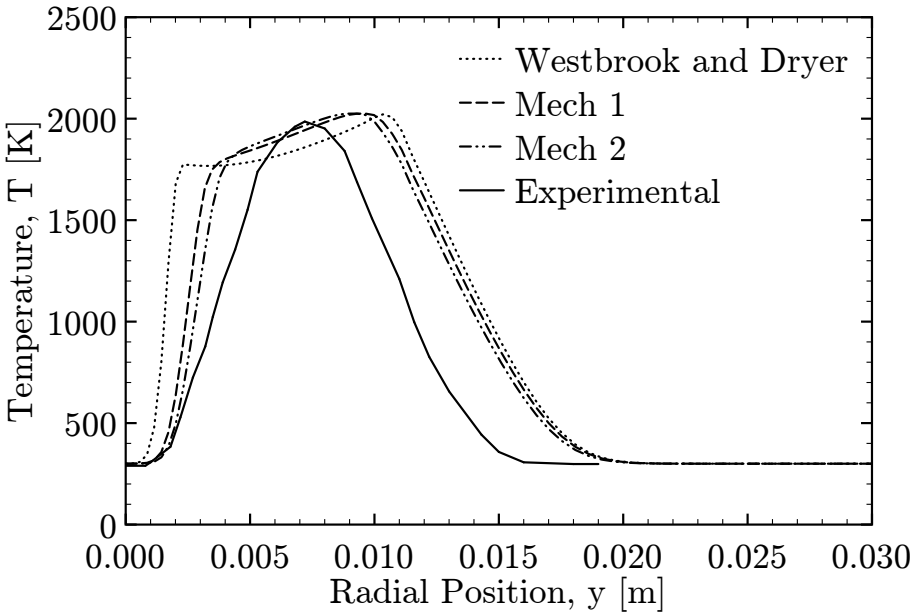

Figure 52. Temperature vs. radius: Mech 1, Mech 2 and Westbrook and Dryer methane combustion mechanism solutions at 50 mm downstream from the tube.

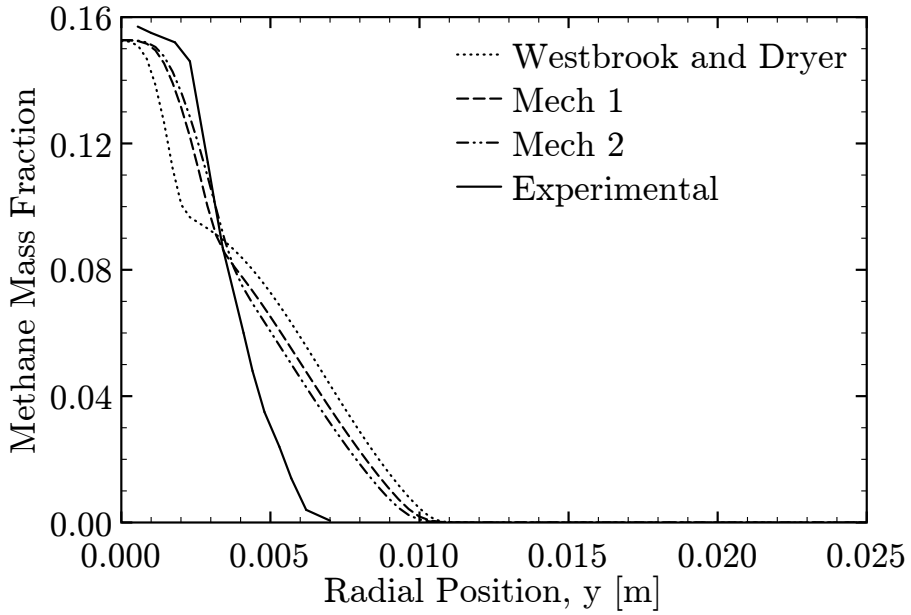

Figure 53. Methane mass fraction vs. radius: Mech 1, Mech 2 and Westbrook and Dryer methane combustion mechanism solutions at 25 mm downstream from the tube.

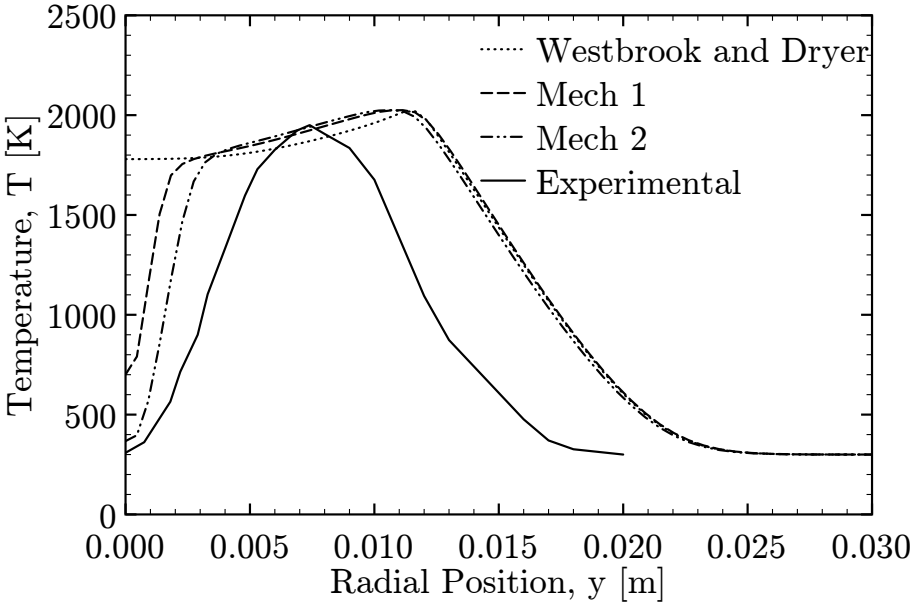

Figure 54. Temperature vs. radius: Mech 1, Mech 2 and Westbrook and Dryer methane combustion mechanism solutions at 100 mm downstream from the tube.

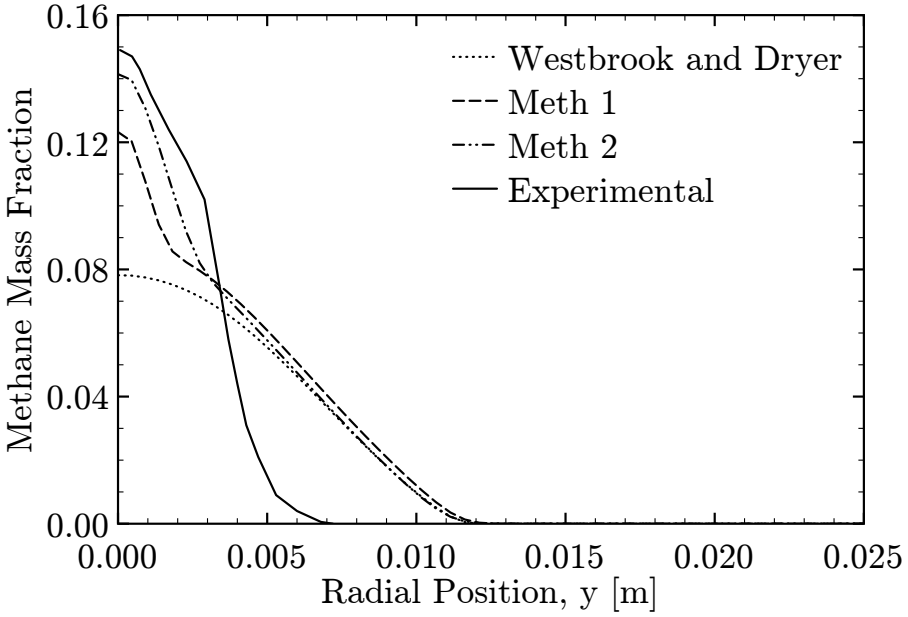

Figure 55. Methane mass fraction vs. radius: Mech 1, Mech 2 and Westbrook and Dryer methane combustion mechanism solutions at 25 mm downstream from the tube.

6.5.3 Entropy Inequality Violations

The entropy inequality violations encountered with the new mechanisms are compared with the results from the Westbrook and Dryer two-step methance combustion mechanism. Each term in the entropy inequality (4.1) are examined at 25 mm downstream from the tube. The effect of the 2025 K temperature limiter is also examined.

The Mech 2 mechanism predicted temperature profiles closer to the experimental data than the Mech 1 mechanism, additionally, the Mech 1 mechanism had nine cells that violated the entropy inequality, while the Mech 2 mechanism had no violations. Figures 56 - 59 are plots of the four terms in the entropy inequality at 25 mm downstream from the tube for both the new mechanism solutions, and the two-step mechanism solution of Westbrook and Dryer. The difference between these three mechanisms is shown in Fig. 58. The Westbrook and Dryer mechanism has a positive term three in Fig. 58, while the new mechanisms produce a term that is negative. Term three leads to the entropy violations for the Westbrook and Dryer mechanism in this region of the flow. Figure 60 displays the sum of the four terms in the entropy inequality for the three mechanisms, Mech 1, Mech 2 and Westbrook and Dryer. For this region of the flow, both the new mechanisms are predicting no entropy inequality violations.

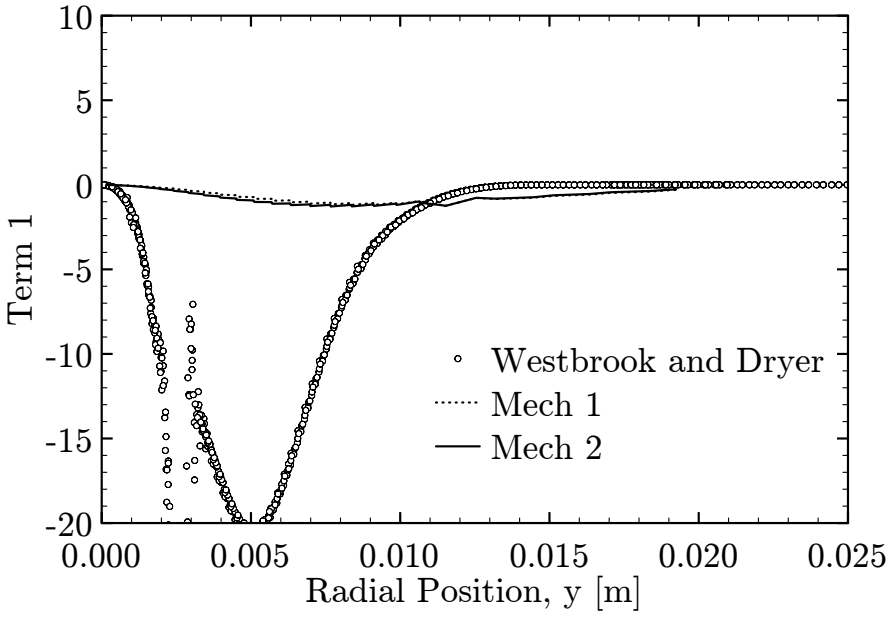

Figure 56. Term 1 vs. radius at 25 mm downstream for the Mech 1, Mech 2 and Westbrook and Dryer simulations.

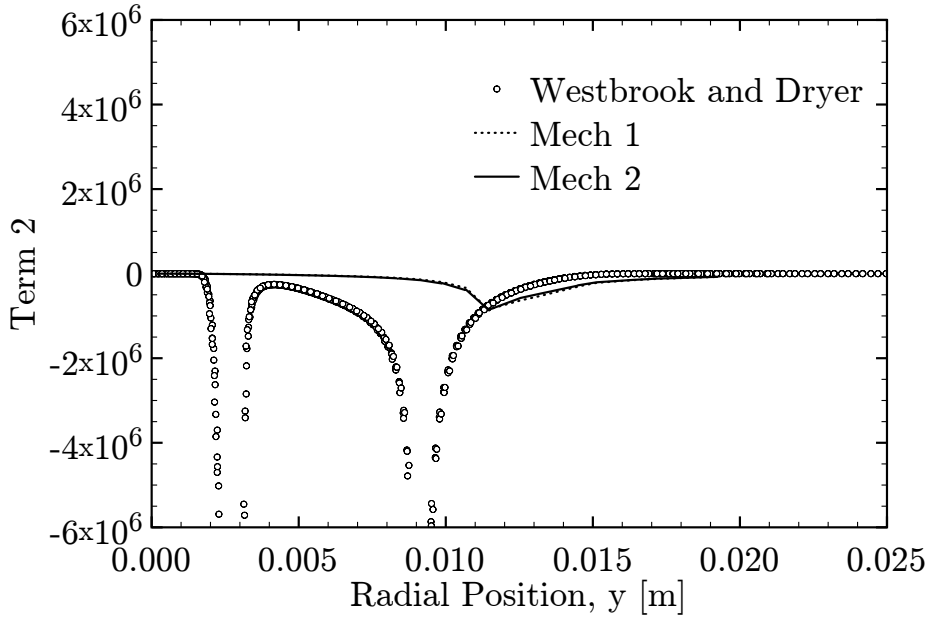

Figure 57. Term 2 vs. radius at 25 mm downstream for the Mech 1, Mech 2 and Westbrook and Dryer simulations.

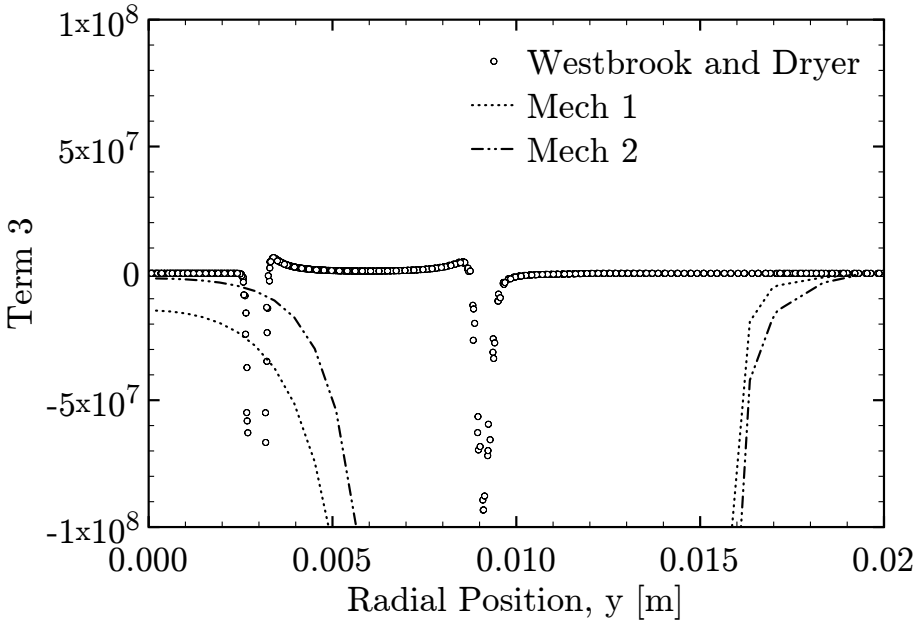

Figure 58. Term 3 vs. radius at 25 mm downstream for the Mech 1, Mech 2 and Westbrook and Dryer simulations.

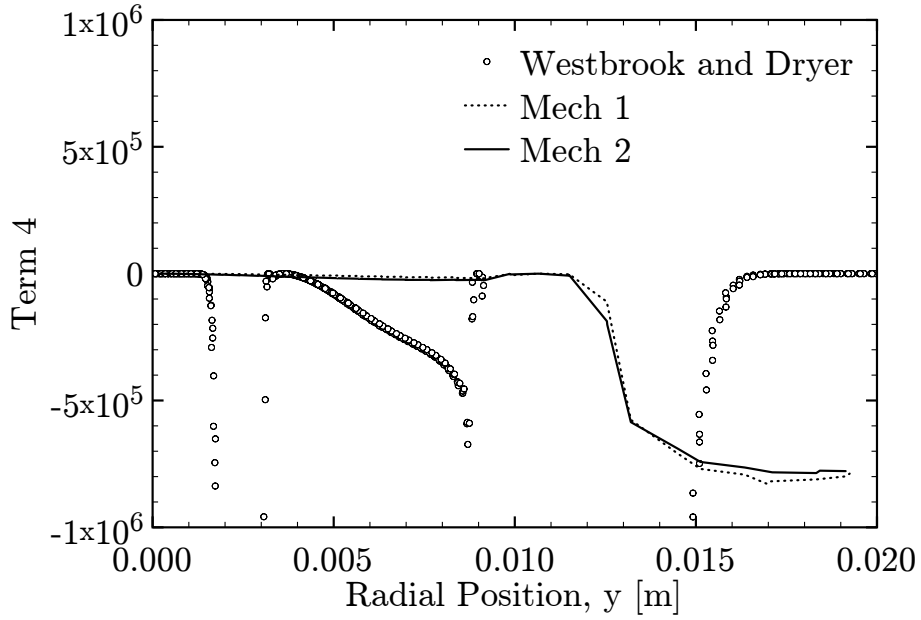

Figure 59. Term 4 vs. radius at 25 mm downstream for the Mech 1, Mech 2 and Westbrook and Dryer simulations.

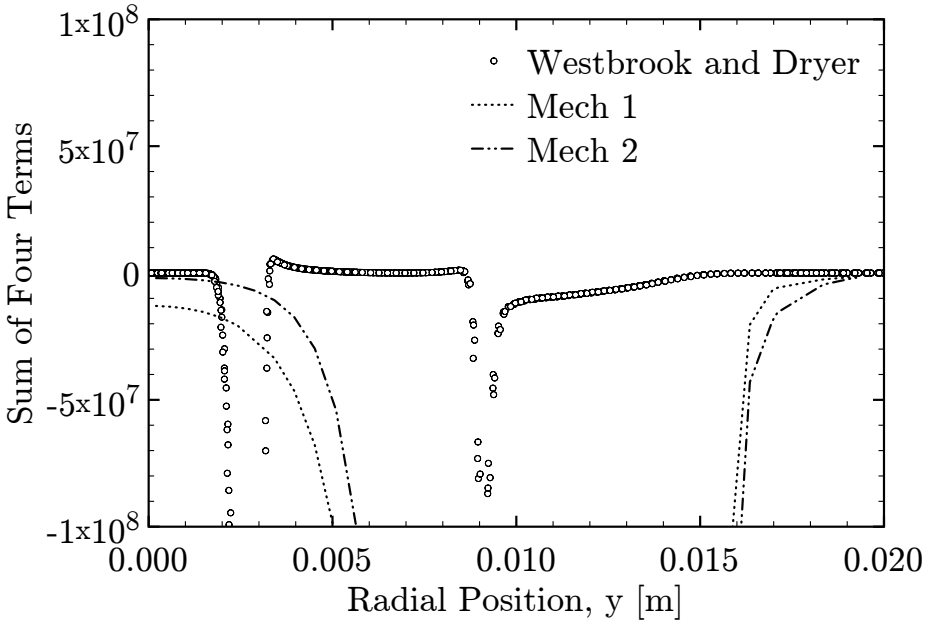

Figure 60. Entropy sum vs. radius at 25 mm downstream for the Mech 1, Mech 2 and Westbrook and Dryer simulations.

The number of violations for the two-step mechanism simulation is significantly reduced using the new mehanism parameters for the Arrhenius rates. The number of violations for Westbrook and Dryer's two-step methane combustion mechanism was 22,016, while the Mech 1 mechanism simulation yielded 9 entropy inequality violating cells and the Mech 2 mechanism did not produce any cell violations. Figure 61 shows the locations of the cells that have the temperature limited to 2025 K, and the cells where the Mech 1 mechanism solution has entropy inequality violations. The cells that have temperature limited for each solution are slightly different. The Mech 1 and

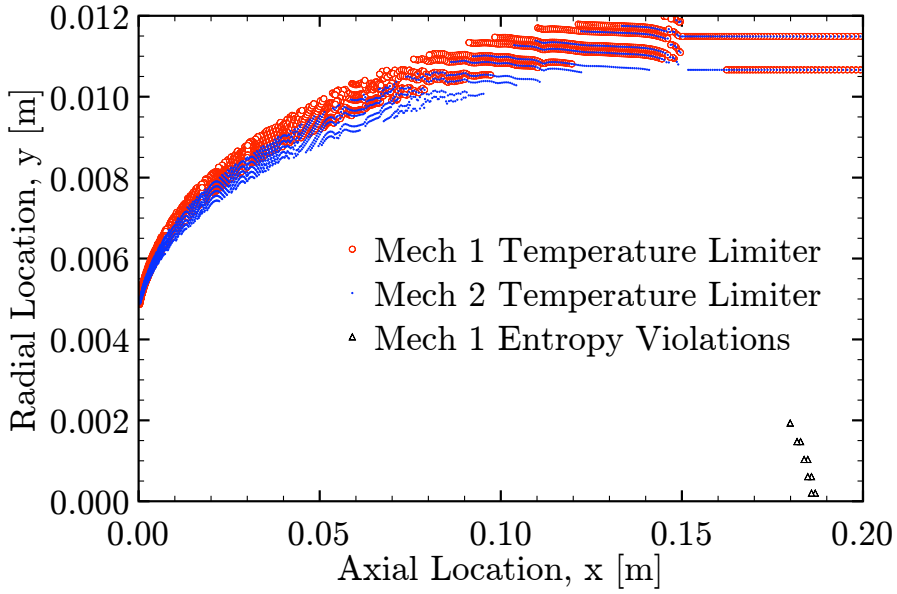

Figure 61. Numerical domain: Cells where the temperature limiter is applied and cells with entropy inequality violations for the new mechanisms. Mech 2 has no entropy inequality violations.

Mech 2 mechanisms both predict a laminar methane-air flame that is closer to the experimental data than the two-step methane combustion mechanism of Westbrook and Dryer.

CHAPTER VII

CONCLUSIONS

A laminar methane-air flame has been simulated in FLUENT to compare the numerical results to experimental data. A two-step methane combustion mechanism developed by Westbrook and Dryer was used to simulate the flame initially. This mechanism produced unsatisfactory results. The profiles of temperature and methane mass fraction at 25, 50 and 100 mm downstream from the fuel tube did not match well the experimental data, and the solution had 22,016 cells that violated the entropy inequality. An effort was made to reduce the entropy violations and predict a flame that matches the experimental data more closely.

The detailed mechanism (84 reactions, 26 species) from Westbrook and Dryer was found to predict accurate flame speeds. The flame speed data reported by Westbrook and Dryer was compared against experimental data and flame speed results from the GRI-3.0 mechanism (325 reactions, 53 species). The flame speeds from Westbrook and Dryer's detailed mechanism match the experimental values and the GRI-3.0 flame speed values well. Therefore, the reduced reaction mechanisms developed by Westbrook and Dryer should predict accurate flame speed values.

A sensitivity analysis was conducted to determine which Arrhenius parameters have the largest effect on the flame speed. The flame speed was most sensitive to variations in the reaction exponents. It has been shown, however, that setting the reaction exponents to the stoichiometric coefficients of the reaction is both a necessary and sufficient condition to satisfying the entropy inequality [45, pp. 2-4]. Consequently, the procedure developed in this thesis varied the Arrhenius parameters A, β and E, instead of the reaction exponents. The reaction exponents were set to the

stoichiometric coefficients of the reaction to ensure the entropy inequality is satisfied.

An effort was made to find ways to reduce the number of entropy inequality violations in the numerical solution. An investigation into the effect of the Soret thermal diffusion coefficient on the two-step methane combustion mechanism simulation indicated that the coefficient helps reduce the number of violations. With the Soret thermal diffusion coefficient turned off the solution produced 23,280 cells that violated the entropy inequality, and with the Soret thermal diffusion coefficient turned on the solution produced 22,016 violating cells. The decrease in entropy inequality violations indicates that the effect of the Soret thermal diffusion coefficient reduces the entropy inequality violations.

A two-step methane combustion mechanism was developed that satisfied locally the second law of thermodynamics and better predicts the flame than existing two-step mechanisms. The two-step methane combustion mechanism used the stoichiometric coefficients as the reaction exponents. The Arrhenius parameters, A, β and E were determined by matching the concentrations computed using the detailed GRI-3.0 mechanism. This method led to two reduced methane combustion mechanisms: Mech 1 and Mech 2. Both mechanisms produced solutions that matched the experimental data more closely than the two-step methane combustion mechanism of Westbrook and Dryer. Additionally, both mechanisms produced solutions with significantly less entropy inequality violations than the Westbrook and Dryer mechanism. The Mech 1 methane combustion mechanism produced 9 violating cells and the Mech 2 methane combustion mechanism did not produce any entropy inequality violations.

The method used to develop the new mechanisms can be applied to any set of reactions. In this work the method is applied to a two-step methane combustion mechanism, but this method can be applied to mechanisms with more species and reactions. As more species and reactions are added to the mechanisms, the matching

of concentrations will improve. Theoretically, if all the reactions and species in the GRI-3.0 mechanism are used in this method, the concentrations will be matched exactly. This method can be used to develop reduced combustion mechanisms until a desired tradeoff between accuracy and computational time is reached.

REFERENCES

[1] C. K. Westbrook, F. L. Dryer, Simplified Reaction Mechanisms for the Oxidation of Hydrocarbon Fuels in Flames, Combustion Science and Technology 27 (1981) 31–43.

[2] C. K. Westbrook, F. L. Dryer, A Comprehensive Mechanism for the Oxidation of Methanol, Combustion Science and Technology 20 (1979) 125–140.

[3] P. J. Stopford, Recent applications of cfd modeling in the power generation and combustion industries, Applied Mathematical Modeling 26 (2002) 351–374.

[4] J. M. Beer, Combustion tehnology developments in power gerneration in response to environmental challenges, Progress in Energy and Combustion Science 26 (2000) 301–327.

[5] D. L. Smoot, A decade of combustion research, Prog. Energy Combust. Sci. 23 (1997) 203–232.

[6] S. M. Correa, Power generation and aeropropulsion gas turbines: From combustion science to combustion technology, Twenty-Seventh Symposium (International) on Combustion/The Combustion Institute (1998) 1793–1807.

[7] J. Bibby, Morpheus project, http://morpheuslander.jsc.nasa.gov/, 2012.

[8] C. Pearson, Hostage to oil, http://greenecon.net/hostage-to-oil/energy_economics.html, 2007.

[9] G. P. Smith, D. M. Golden, M. Frenklach, N. W. Moriarty, B. Eitenner et. al., Gri-mech 3.0, http://www.me.berkeley.edu/gri_mech/, 2011.

[10] K. Seshadari, J. Gottgens, The Computation of Stretched Laminar Methane-Air Diffusion Flames Using a Reduced Four-Step Meachanism, Lecture Notes in Physics 384 (1991) 111–136.

[11] K. Seshadri, X. S. Bai, H. Pitsch, N. Peters, Asymptotic Analysis of the Structure of Moderately Rich Methane-Air Flames, Combustion and Flame 113 (1998) 589–602.

[12] K. Seshadri, X. S. Bai, H. Pitsch, Asymptotic Structure of Rich Methane-Air Flames, Combustion and Flame 127 (2002) 2265–2277.

[13] N. Peters, F. A. Williams, The Asymptotic Structure of Stoichiometric Methane-Air Flames, Combustion and Flame 68 (1987) 185–207.

[14] M. D. Smooke (Ed.), Reduced Kinetic Mechanisms and Asymptotic Approximations for Methane-Air Flames, Springer-Verlag, 1991.

[15] M. Bui-Pham, K. Seshadari, F. A. Williams, The Asymptotic Structure of Premixed Methane-Air Flames with Slow CO Oxidation, Combustion and Flame 89 (1992) 343–362.

[16] R. W. Bilger, S. H. Starner, R. J. Kee, On Reduced Mechanisms for Methane-Air Combustion in Nonpremixed Flames, Combustion and Flame 80 (1990) 135–149.

[17] C. K. Westbrook, F. L. Dryer, Prediction of Laminar Flame Properties of Methanol–Air Mixtures, Combustion and Flame 37 (1980) 171–192.

[18] FLUENT 6.1 User's Guide, FLUENT Inc., http://jullio.pe.kr/fluent6.1/help/html/ug/mainpre.htm, 2003.

[19] K. K. Y. Kuo, Principles of Combustion, John Wiley and Sons, New York, 1986.

[20] R. C. Reid, J. M. Prausnitz, B. E. Poling, The Properties of Gases and Liquids, 4th Ed., McGraw-Hill Inc., New York, 1987.

[21] R. A. Svehla, NASA Technical Report R-132, Technical Report, Lewis Research Center, Cleveland, OH, 1962.

[22] A. Burcat, B. McBride, 1997 Ideal Gas Thermodynamic Data for Combustion and Air-Pollution Use, Technical Report, Technion Israel Institute of Technology, Aerospace Engineering Report, TAE 804, 1997.

[23] M. W. Chase, J. L. Curnutt, R. A. Downey, S. A. N., E. A. Valenzuela, S. A. N., Janaf thermochemical tables, 1982 supplement, Journal of Physical and Chemical Reference Data 11 (1982) 695–941.

[24] H. J. Merk, The macroscopic equations for simultaneous heat and mass transfer in isotropic, continuous and closed systems, Appl. Sci. Res. 8 (1958) 73–99.

[25] CHEMKIN Collection Release 3.6, Reaction Design, http://www.dipic.unipd.it/faculty/canu/files/Comb/Docs/chemkinCK.pdf, 2000.

[26] C. M. Lund, HCT - A General Computer Program for Calculating Time-Dependent Phenomena Involving One-Deimensional Hydrodynamics, Transport, and Detailed Chemical Kinetics, UCRL-52504, Technical Report, Lawrence Livermore Laboratory, Livermore, California, 1978.

[27] M. W. Chase, J. L. Curnutt, A. T. Hu, H. Prophet, A. N. Syverud, C. Walker, Janaf thermochemical tables, 1974 supplement, Journal of Physical and Chemical Reference Data 3 (1974) 311–329.

[28] C. Developers, Cantera: Chemical kinetics, therodynamics, transport processes, http://cantera.github.com/docs/sphinx/html/index.html, 2012.

[29] J. C. Slattery, Advanced Transport Phenomena, Cambridge University Press, Cambridge, UK, 1999.

[30] S. B. Chambers, Investigation of Combustive Flows and Dynamic Meshing in Computational Fluid Dynamics, Master's thesis, Texas A&M University, 2004.

[31] J. M. Smith, H. C. Van Ness, Introduction to Chemical Engineering Thermodynamics, McGraw-Hill Inc., New York, 1987.

[32] N. Peters, Reducing mechanisms, volume 384 of *Lecture Notes in Physics*, Springer Berlin / Heidelberg, pp. 48–67. 10.1007/BFb0035365.

[33] N. Peters, R. J. Kee, The Computation of Stretched Laminar Methane-Air Diffusion Flames Using a Reduced Four-Step Meachanism, Combustion and Flame 68 (1987) 17–29.

[34] N. Peters, Turbulent Combustion, Cambridge University Press, 2004.

[35] A. K. T. Hassan, M. I., G. M. Faeth, Measured and Predicted Properties of Laminar Premixed Methane/Air Flames at Various Pressures, Combustion and Flame 115 (1998) 539–550.

[36] K. T. Aung, L.-K. Tseng, M. A. Ismail, G. M. Faeth, Response to Comment by S. C. Taylor and D. B. Smith on "Laminar Burning Velocities and Markstein Numbers of Hydrocarbon/Air Flames", Combustion and Flame 102 (1995) 526–530.

[37] A. Van Maaren, L. P. de Goey, Stretch and the Adiabatic Burning Velocity of Methane-and Propane-Air Flames, Combustion Science and Technology 102 (1994) 309–314.

[38] S. R. Clarke, A., P. Beckwith, Measuring the laminar burning velocity of methane/diluent/air mixtures within a constant-volume combustion bomb in a micro-gravity environment, Journal of the Institue of Energy 68 (1995) 130–136.

[39] M. A. S. D. B. Haniff, M. S., A. Williams, The burning velocities of methane and SNG mixtures in air, Journal of the Institue of Energy 62 (1989) 229–236.

[40] C. M. Vagelopoulos, F. N. Egolfopoulos, Direct Experimental Determination of Laminar Flame Speeds, Twenty-Seventh Symposium (International) on Combustion/The Combustion Institute (1998) 513–519.

[41] V. C. M. Egolfopoulos, F. N., C. K. Law, Further Considerations on the Determination of Laminar Flame Speeds with the Counterflow Twin-Flame Technique, Twenty-Fifth Symposium (International) on Combustion/The Combustion Institute (1994) 1341–1347.

[42] C. P. Egolfopoulos, F. N., C. K. Law, Laminar Flame Speeds of Methane-Air Mixtures Under Reduced and Elevated Pressures, Combustion and Flame 76 (1989) 375–391.

[43] I. Yamaoka, H. Tsuji, Determination of burning velocity using couterflow flames, Twentieth Symposium (International) on Combustion/The Combustion Institute 20 (1985) 1883–1892.

[44] GAMBIT Modeling Guide, FLUENT Inc., http://202.118.250.111:8080/fluent /Gambit13help/modelingguide/mgtoc.htm, 2000.

[45] J. C. Slattery, P. G. A. Cizmas, A. N. Karpetis, S. B. Chambers, Role of differential entropy inequality in chemically reacting flows, Chemical Engineering Science 66 (2011) 5236–5243.

APPENDIX A

HCT FILES

An input file from HCT is briefly described and the process for calculating the flame speed from HCT output is discussed. For a more detailed explanation of the HCT files, refer to [26].

The input file contains the array lists, which is where the species needed for the simulation is specified. HCT has an extensive list of hundreds of species. To find the species needed for the simulation a "shotgun" approached is used to find which numbers correspond to what species. The number zones is specified with nzones., and the number of zones clustered around the temperature gradient is controlled with nzxcess. To initialize the grid, the array c is used. This array stores the concentrations of the N species in the first N elements, followed by temperature, Δr and velocity. The pressures for the system is specified with pr0 and prbr. The parameter prbr, is the pressure at the right boundary, and pr0 is the initial pressure of the system, used to scale c such that the pressure is constant. The thermal and molecular diffusion coefficients are defined with dzero and dczero, respectively. These constants are used in the power law dependence defined in chapter II. To initiate combustion, a source term is defined using sorxmax, sorsprd and sorpcc. These variables are defined and the methodology is explaind in [26]. This source term initiates combustion in the first zone, and the flame from propagates downstream. The time step is constantly evolving in HCT. Initially, the time step is defined with dt, and the max and min timestep is also defined with dtmax and dtmin, respectively. The maximum number of iterations is set with mxcycle, and a convergence criterion is set with cnvg.

The reactions for the simulation can be set by the user in the input file. The number of reactions is set with nreact. To defined the reaction an array, irs, is defined

with the species contained within the reaction, and an array, xnp, is defined for the stoichiometric coefficients. The species used in the Arrhenius reaction rate are defined with array isp, and the reaction exponents of these species is set with xlp. Finally the parameters, A, β and E are defined with frc, frp and frx. An example is shown in Table XIV for the first reaction in the two-step mechanism. An example of the indices are, irs(reaction,species) and frc(reaction).

$$CH_4 + 1.5O_2 \rightleftharpoons CO + 2H_2O$$

Table XIV. HCT Reaction Input

irs(1,1) = 64 (CH_4)	xnp(1,1) = 1
irs(1,2) = 16 (O_2)	xnp(1,2) = 1.5
irs(1,3) = 48 (CO)	xnp(1,3) = -1
irs(1,4) = 24 (H_2O)	xnp(1,4) = -2
isp(1,1) = 64 (CH_4)	xlp(1,1) = 0.7
isp(1,2) = 16 (O_2)	xlp(1,2) = 0.8
frc(1) = 5.012e11	
frp(1) = 0.0	
frx(1) = 48400 ([cal/mol])	

The input in Table XIV corresponds to an Arrhenius reation rate form of

$$k_f = 5.012e11\ T^{0.0}\ \exp\frac{48400}{RT}\ [\mathrm{CH_4}]^{0.7}\ [\mathrm{O_2}]^{0.8}.$$

An example input file is included below, for further explanation refer to the index in the HCT manual [26].

```
*namdump='dfile0'
lists=16 56 24 64 32 48
iflame=1
ircymx=1000
mxmz = 999
cnvg = 1.e-6
c=6(1.e-6) 300. 10.2 0.
c(1)=.190
c(4)=.095
c(5)=.715
pr0=10132.5
prbr=10132.5
*prmul=0.0
s0=1.
s1=0.
xsprd=.04
nzones=75
xmax=10.0
dczero=1.92e-6
dzero=9.26e-6
sorxmax=0.
sorsprd=.01
sorpcc=1500.
tig=1.3e-4
iprint=100 0 100 100 100 100
lste4=1(1)75
itimer=1
eta2=.15
delymn=300.
euler=1.
euler2=-1.
rzflag=1.
itermx=20
rdelcmx=.1
dt=1.e-5
dtmax=1.
timemx=10.
dtmin=1.e-20
mxcycle=50000
nzxcess=50
nreact=3
itz1mx=200
rdelw2=0.005
******* Reactions
******* Reaction 1 CH4 + 1.5O2 - CO + 2H2O
irs(1,1)=64
irs(1,2)=16
irs(1,3)=48
irs(1,4)=24
xnp(1,1)=1.
xnp(1,2)=1.5
xnp(1,3)=-1.
```

```
xnp(1,4)=-2.
isp(1,1)=64
isp(1,2)=16
*isp(1,3)=48
*isp(1,4)=24
xlp(1,1)=0.7
xlp(1,2)=0.8
*xlp(1,3)=1.
*xlp(1,4)=2.
frc(1)=5.012e11
frp(1)=0.
frx(1)=47800
******* Reaction 2f CO + 0.5O2 - CO2 + (ZERO)H2O
irs(2,1)=48
irs(2,2)=16
irs(2,3)=56
xnp(2,1)=1.
xnp(2,2)=0.5.
xnp(2,3)=-1.
isp(2,1)=48
isp(2,2)=16
isp(2,3)=24
xlp(2,1)=1.
xlp(2,2)=0.25
xlp(2,3)=0.5
frc(2)=2.239e12
frp(2)=0.
frx(2)=40630
******* Reaction 2b CO2 - CO + 0.5O2
irs(3,1)=56
irs(3,2)=16
irs(3,3)=48
xnp(3,1)=1.
xnp(3,2)=-0.5.
xnp(3,3)=-1.
isp(3,1)=56
*isp(3,2)=16
*isp(3,3)=48
xlp(3,1)=1.
*xlp(3,2)=0.5
*xlp(3,3)=1.
frc(3)=5.e8.
frp(3)=0.
frx(3)=40630
$
```

The flame speed is calculated from the output data from HCT. The frequency at which the data is output, is specified with iprint in the input file. This array allows the user to specify the iterations which data will be written to an output file. The flag iflame must be set to one for the code to output the position of the flame. A couple portions of the output file from HCT is included for the discussion.

```
                                        hct output                              vers.95r     01/03/08

cycle=      2350 avgiter=  4.22E+00 ircytot=    0 irzftot=    0 njcbtot=  186 time=  3.2263E-02 dt=  2.18E-05
```

```
species limiting dt-   1 zone- 12
slowest converging species-   8 zone-  9
 flame ( 1500.) position is zone        15 at  8.486E+00
 flame ( 2000.) position is zone        13 at  8.414E+00


  jd     r         dr      ctot     rho       t        u      press    edotr    edotc    edotd   p*dv/dx   vsound


   1 0.0000E+00 1.76E+00 4.99E-07 1.38E-05  2436.05  0.00E+00  1.01E+05  7.89E-28 -2.13E+05  1.11E+03  4.15E+04  9.55E+04
   2 1.7599E+00 1.62E+00 5.13E-07 1.42E-05  2368.92 -7.24E-01  1.01E+05  2.94E-18  9.38E+04  1.23E+02 -1.79E+04  9.43E+04
   3 3.3785E+00 1.38E+00 5.21E-07 1.44E-05  2332.92 -4.37E-01  1.01E+05  5.60E-11  1.44E+05 -7.84E+02 -2.75E+04  9.36E+04
   4 4.7596E+00 1.10E+00 5.21E-07 1.44E-05  2329.59 -6.06E-02  1.01E+05  1.50E-05  1.95E+04 -4.16E+02 -3.46E+03  9.35E+04
   5 5.8575E+00 8.23E-01 5.22E-07 1.44E-05  2329.24 -2.30E-02  1.01E+05  1.44E-01 -3.01E+03  3.71E+01  7.40E+02  9.35E+04
   6 6.6810E+00 5.91E-01 5.22E-07 1.44E-05  2328.78 -2.91E-02  1.01E+05  1.18E+02  1.57E+03  5.87E+01 -1.86E+01  9.35E+04
   7 7.2720E+00 4.11E-01 5.22E-07 1.44E-05  2328.51 -2.90E-02  1.01E+05  1.48E+04 -3.84E+04  1.68E+02  5.51E+03  9.35E+04
   8 7.6829E+00 2.79E-01 5.22E-07 1.44E-05  2327.74 -5.14E-02  1.01E+05  4.29E+05 -2.67E+05 -2.49E+02 -2.34E+04  9.35E+04
   9 7.9622E+00 1.87E-01 5.22E-07 1.44E-05  2325.33  1.33E-02  1.01E+05  4.58E+06 -2.71E+06 -1.28E+02 -3.25E+05  9.35E+04
  10 8.1493E+00 1.24E-01 5.25E-07 1.45E-05  2315.18  6.15E-01  1.01E+05  3.40E+07 -2.24E+07  5.95E+03 -2.09E+06  9.33E+04
  11 8.2734E+00 8.20E-02 5.34E-07 1.47E-05  2277.12  3.18E+00  1.01E+05  2.03E+08 -1.46E+08 -9.40E+04 -1.07E+07  9.25E+04
  12 8.3554E+00 5.52E-02 5.63E-07 1.55E-05  2159.53  1.19E+01  1.01E+05  6.88E+08 -4.99E+08 -1.71E+06 -3.72E+07  9.02E+04
  13 8.4106E+00 4.08E-02 6.34E-07 1.75E-05  1915.99  3.22E+01  1.01E+05  7.10E+08 -3.72E+08 -6.72E+06 -6.88E+07  8.52E+04
  14 8.4514E+00 3.51E-02 7.45E-07 2.05E-05  1630.39  6.00E+01  1.01E+05  2.05E+08  1.74E+08 -9.61E+06 -7.78E+07  7.89E+04
  15 8.4865E+00 3.44E-02 8.87E-07 2.44E-05  1369.06  8.71E+01  1.01E+05  2.40E+07  3.21E+08 -7.75E+06 -7.24E+07  7.26E+04
  16 8.5209E+00 3.70E-02 1.08E-06 2.96E-05  1130.11  1.12E+02  1.01E+05  1.01E+06  2.89E+08 -4.94E+06 -6.34E+07  6.63E+04
  17 8.5579E+00 4.28E-02 1.35E-06 3.70E-05   902.44  1.35E+02  1.01E+05  7.74E+03  2.30E+08 -2.41E+06 -5.31E+07  5.96E+04
  18 8.6006E+00 5.33E-02 1.78E-06 4.91E-05   681.46  1.57E+02  1.01E+05  2.25E+00  1.66E+08 -5.87E+05 -4.10E+07  5.23E+04
  19 8.6540E+00 7.19E-02 2.54E-06 7.01E-05   477.97  1.79E+02  1.01E+05  1.09E-06  1.01E+08  1.21E+05 -2.68E+07  4.43E+04
  20 8.7259E+00 1.01E-01 3.53E-06 9.73E-05   344.41  1.98E+02  1.01E+05  5.05E-15  3.53E+07  9.20E+04 -1.01E+07  3.81E+04
  21 8.8273E+00 1.42E-01 3.95E-06 1.09E-04   307.59  2.08E+02  1.01E+05  1.29E-18  4.47E+06  1.66E+04 -1.32E+06  3.62E+04
  22 8.9691E+00 1.91E-01 4.03E-06 1.11E-04   301.32  2.10E+02  1.01E+05  2.58E-19  3.93E+05  2.13E+03 -1.12E+05  3.58E+04
  23 9.1597E+00 2.43E-01 4.05E-06 1.12E-04   300.32  2.10E+02  1.01E+05  1.98E-19  3.70E+04  1.45E+02 -9.64E+03  3.58E+04
  24 9.4023E+00 2.88E-01 4.05E-06 1.12E-04   300.16  2.10E+02  1.01E+05  1.90E-19  3.51E+03 -4.80E+00 -1.15E+03  3.58E+04
  25 9.6900E+00 3.15E-01 4.05E-06 1.12E-04   300.11  2.10E+02  1.01E+05  1.87E-19  1.21E+03 -2.86E+00 -5.14E+02  3.58E+04

                                     total energy production rate 9.69E+07-7.35E-09-1.28E+06-2.12E+07

 total mass=  2.733937E-04 total internal energy= -1.633040E+06

 subroutine  sec/call  sec/cycle


   diffun    7.70E-05  2.84E-04
   difped    2.14E-04  1.14E-04
   solbtl    1.82E-04  7.67E-04
   decbtl    1.68E-03  8.94E-04
   rezone    2.84E-05  2.84E-05
   ckcnvg    3.37E-05  1.42E-04
   remap     2.85E-05  2.85E-05
 ncycle=      2350  time= 3.226E-02  dt= 2.179E-05  temp(2)= 2.436E+03  pres(2)= 1.010E+05
 ncycle=      2351  time= 3.228E-02  dt= 2.179E-05  temp(2)= 2.436E+03  pres(2)= 1.010E+05
 ncycle=      2352  time= 3.231E-02  dt= 2.179E-05  temp(2)= 2.436E+03  pres(2)= 1.010E+05
 ncycle=      2353  time= 3.233E-02  dt= 2.179E-05  temp(2)= 2.436E+03  pres(2)= 1.010E+05
 ncycle=      2354  time= 3.235E-02  dt= 2.179E-05  temp(2)= 2.436E+03  pres(2)= 1.010E+05
 ncycle=      2355  time= 3.237E-02  dt= 2.179E-05  temp(2)= 2.436E+03  pres(2)= 1.010E+05
 ncycle=      2356  time= 3.239E-02  dt= 2.178E-05  temp(2)= 2.436E+03  pres(2)= 1.010E+05
 ncycle=      2357  time= 3.242E-02  dt= 2.178E-05  temp(2)= 2.436E+03  pres(2)= 1.010E+05
 ncycle=      2358  time= 3.244E-02  dt= 2.179E-05  temp(2)= 2.436E+03  pres(2)= 1.010E+05
 ncycle=      2359  time= 3.246E-02  dt= 2.179E-05  temp(2)= 2.436E+03  pres(2)= 1.010E+05


                                              hct output                                vers.95r     01/03/08


cycle=      2360 avgiter=  4.28E+00 ircytot=    0 irzftot=    0 njcbtot=  193 time=  3.2481E-02 dt=  2.18E-05


species limiting dt-   1 zone- 12
slowest converging species-   1 zone-  1
 flame ( 1500.) position is zone        15 at  8.539E+00
 flame ( 2000.) position is zone        13 at  8.467E+00


  jd     r         dr      ctot     rho       t        u      press    edotr    edotc    edotd   p*dv/dx   vsound


   1 0.0000E+00 1.77E+00 4.99E-07 1.38E-05  2435.73  0.00E+00  1.01E+05  2.58E-28 -2.11E+05  1.11E+03  3.90E+04  9.55E+04
   2 1.7652E+00 1.62E+00 5.13E-07 1.42E-05  2368.78 -6.82E-01  1.01E+05  1.20E-18  9.31E+04  1.20E+02 -1.97E+04  9.43E+04
   3 3.3895E+00 1.39E+00 5.21E-07 1.44E-05  2332.90 -3.65E-01  1.01E+05  2.75E-11  1.42E+05 -7.78E+02 -2.90E+04  9.36E+04
   4 4.7768E+00 1.10E+00 5.21E-07 1.44E-05  2329.58  3.39E-02  1.01E+05  8.53E-06  1.92E+04 -4.09E+02 -4.95E+03  9.35E+04
   5 5.8811E+00 8.30E-01 5.22E-07 1.44E-05  2329.22  8.80E-02  1.01E+05  9.26E-02 -2.89E+03  3.76E+01 -8.71E+02  9.35E+04
   6 6.7107E+00 5.96E-01 5.22E-07 1.44E-05  2328.76  9.52E-02  1.01E+05  8.39E+01 -2.36E+02  6.40E+01 -1.29E+03  9.35E+04
   7 7.3071E+00 4.15E-01 5.22E-07 1.44E-05  2328.43  1.03E-01  1.01E+05  1.17E+04 -3.61E+04  2.14E+02  3.86E+03  9.35E+04
   8 7.7224E+00 2.83E-01 5.22E-07 1.44E-05  2327.64  8.69E-02  1.01E+05  3.74E+05 -2.27E+05 -3.07E+02 -2.27E+04  9.35E+04
   9 8.0053E+00 1.90E-01 5.22E-07 1.44E-05  2325.46  1.51E-01  1.01E+05  4.18E+06 -2.46E+06 -3.35E+02 -2.99E+05  9.35E+04
  10 8.1950E+00 1.26E-01 5.25E-07 1.45E-05  2316.01  7.12E-01  1.01E+05  3.12E+07 -2.05E+07  6.05E+03 -1.93E+06  9.33E+04
```

```
11 8.3211E+00 8.34E-02 5.33E-07 1.47E-05  2280.20  3.12E+00  1.01E+05  1.88E+08 -1.35E+08 -7.56E+04 -9.98E+06  9.26E+04
12 8.4044E+00 5.61E-02 5.60E-07 1.55E-05  2168.31  1.14E+01  1.01E+05  6.63E+08 -4.82E+08 -1.54E+06 -3.55E+07  9.04E+04
13 8.4606E+00 4.12E-02 6.29E-07 1.73E-05  1930.87  3.11E+01  1.01E+05  7.34E+08 -4.02E+08 -6.43E+06 -6.76E+07  8.55E+04
14 8.5018E+00 3.52E-02 7.38E-07 2.03E-05  1645.47  5.87E+01  1.01E+05  2.25E+08  1.55E+08 -9.62E+06 -7.79E+07  7.92E+04
15 8.5370E+00 3.43E-02 8.78E-07 2.42E-05  1383.17  8.58E+01  1.01E+05  2.78E+07  3.20E+08 -7.91E+06 -7.28E+07  7.29E+04
16 8.5712E+00 3.66E-02 1.06E-06 2.92E-05  1143.82  1.10E+02  1.01E+05  1.26E+06  2.92E+08 -5.10E+06 -6.39E+07  6.67E+04
17 8.6079E+00 4.22E-02 1.33E-06 3.65E-05   916.32  1.34E+02  1.01E+05  1.12E+04  2.34E+08 -2.55E+06 -5.38E+07  6.00E+04
18 8.6500E+00 5.23E-02 1.75E-06 4.81E-05   695.59  1.56E+02  1.01E+05  4.46E+00  1.71E+08 -6.74E+05 -4.19E+07  5.28E+04
19 8.7023E+00 6.99E-02 2.47E-06 6.82E-05   490.93  1.78E+02  1.01E+05  3.98E-06  1.05E+08  1.08E+05 -2.79E+07  4.49E+04
20 8.7723E+00 9.82E-02 3.47E-06 9.56E-05   350.55  1.97E+02  1.01E+05  1.69E-14  3.95E+07  1.01E+05 -1.13E+07  3.84E+04
21 8.8705E+00 1.37E-01 3.93E-06 1.09E-04   309.03  2.08E+02  1.01E+05  1.86E-18  5.40E+06  1.97E+04 -1.60E+06  3.63E+04
22 9.0075E+00 1.84E-01 4.03E-06 1.11E-04   301.60  2.10E+02  1.01E+05  2.77E-19  5.00E+05  2.60E+03 -1.45E+05  3.59E+04
23 9.1915E+00 2.34E-01 4.04E-06 1.12E-04   300.38  2.10E+02  1.01E+05  2.01E-19  4.85E+04  1.91E+02 -1.36E+04  3.58E+04
24 9.4251E+00 2.77E-01 4.05E-06 1.12E-04   300.17  2.11E+02  1.01E+05  1.91E-19  4.86E+03 -5.41E+00 -2.13E+03  3.58E+04
25 9.7020E+00 3.03E-01 4.05E-06 1.12E-04   300.11  2.11E+02  1.01E+05  1.88E-19  1.53E+03 -3.88E+00 -9.44E+02  3.58E+04
```

The bold quantities in the output above are used for the flame speed calculation. To compute the speed in the lab reference frame, simply divide the change in position by the change in time, written as

$$v_{lr} = \frac{x_{fl2} - x_{fl1}}{t_2 - t_1}.$$

Once the lab reference frame speed is found, simply subtract the velocity reported in the last zone.

$$flsp = v_{lr} - v_{lastzone}$$

From the output file above, the flame speed is computed to be 33.12 cm/sec.

APPENDIX B

CANTERA CODE

The code used to calculated the flame speed in Cantera using the Gri-Mech 3.0 mechanism is included here. The code is written in Python, and the demo came with the installation of Cantera. The composition can be modified to change the equivalence ratio. This was the procedure for computing the flame speed versus equivalence ratio plot, Fig. 4. The code sets up a grid for the one dimensional laminar flame, and uses the multicomponent transport model. The output from the code shows the iteration process and concludes by outputting the flame speed.

```
#
# ADIABATIC_FLAME - A freely-propagating, premixed methane/air flat
#          flame with multicomponent transport properties
#
from Cantera import *
from Cantera.OneD import *
from Cantera.OneD.FreeFlame import FreeFlame

###############################################################
#
# parameter values
#
p          =   OneAtm               # pressure
tin        =   300.0                # unburned gas temperature
mdot       =   0.04                 # kg/m^2/s

comp       =  'CH4:1, O2:2, N2:7.52'  # premixed gas composition

initial_grid = [0.0, 0.001, 0.01, 0.02, 0.029, 0.03] # m

tol_ss    = [1.0e-5, 1.0e-9]        # [rtol atol] for steady-state
                                    # problem
tol_ts    = [1.0e-5, 1.0e-9]        # [rtol atol] for time stepping

loglevel  = 1                       # amount of diagnostic output (0
                                    # to 5)

refine_grid = 1                     # 1 to enable refinement, 0 to
                                    # disable


gas = GRI30('Mix')
#gas = importPhase('gri30.cti','gri30')
gas.addTransportModel('Multi')

# set its state to that of the unburned gas
gas.setState_TPX(tin, p, comp)

f = FreeFlame(gas = gas, grid = initial_grid, tfix = 600.0)
```

```
# set the upstream properties
f.inlet.set(mole_fractions = comp, temperature = tin)

f.set(tol = tol_ss, tol_time = tol_ts)
f.showSolution()

f.set(energy = 'off')
f.setRefineCriteria(ratio = 10.0, slope = 1, curve = 1)
f.setMaxJacAge(50, 50)
f.setTimeStep(1.0e-5, [2, 5, 10, 20, 50])

f.solve(loglevel, refine_grid)
f.save('ch4_adiabatic.xml','no_energy',
       'solution with the energy equation disabled')

f.set(energy = 'on')
f.setRefineCriteria(ratio = 3.0, slope = 0.1, curve = 0.2)
f.solve(loglevel, refine_grid)
f.save('ch4_adiabatic.xml','energy',
       'solution with the energy equation enabled')
print 'mixture-averaged flamespeed = ',f.u()[0]

gas.switchTransportModel('Multi')
f.flame.setTransportModel(gas)
f.solve(loglevel, refine_grid)
f.save('ch4_adiabatic.xml','energy_multi',
       'solution with the energy equation enabled and multicomponent transport')

# write the velocity, temperature, density, and mole fractions to a CSV file
z = f.flame.grid()
T = f.T()
u = f.u()
V = f.V()
fcsv = open('adiabatic_flame.csv','w')
writeCSV(fcsv, ['z (m)', 'u (m/s)', 'V (1/s)', 'T (K)', 'rho (kg/m3)']
         + list(gas.speciesNames()))
for n in range(f.flame.nPoints()):
    f.setGasState(n)
    writeCSV(fcsv, [z[n],  u[n], V[n], T[n], gas.density()]
             +list(gas.moleFractions()))
fcsv.close()

print 'solution saved to adiabatic_flame.csv'
print 'multicomponent flamespeed = ',u[0]
f.showStats()

print f.netProductionRates()
```

A sample of the output for this code.

```
>>>>>>>>>>>>>>>>>>>>>>>>>>>>>>>> burner <<<<<<<<<<<<<<<<<<<<<<<<<<<<<<<<

    Mass Flux:            0 kg/m^2/s
    Temperature:        300 K
    Mass Fractions:
                     O2      0.2201
                    CH4     0.05519
                     N2      0.7247



>>>>>>>>>>>>>>>>>>>>>>>>>>>>>>>> flame <<<<<<<<<<<<<<<<<<<<<<<<<<<<<<<<

    Pressure:   1.013e+05 Pa

---------------------------------------------------------------------------
```

z	u	V	T	lambda	H2
0	0	0	0	0	0
0.001	0	0	0	0	0
0.01	0	0	0	0	0
0.02	0	0	0	0	0
0.029	0	0	0	0	0
0.03	0	0	0	0	0

z	H	O	O2	OH	H2O
0	0	0	0	0	0
0.001	0	0	0	0	0
0.01	0	0	0	0	0
0.02	0	0	0	0	0
0.029	0	0	0	0	0
0.03	0	0	0	0	0

z	HO2	H2O2	C	CH	CH2
0	0	0	0	0	0
0.001	0	0	0	0	0
0.01	0	0	0	0	0
0.02	0	0	0	0	0
0.029	0	0	0	0	0
0.03	0	0	0	0	0

z	CH2(S)	CH3	CH4	CO	CO2
0	0	0	0	0	0
0.001	0	0	0	0	0
0.01	0	0	0	0	0
0.02	0	0	0	0	0
0.029	0	0	0	0	0
0.03	0	0	0	0	0

z	HCO	CH2O	CH2OH	CH3O	CH3OH
0	0	0	0	0	0
0.001	0	0	0	0	0
0.01	0	0	0	0	0
0.02	0	0	0	0	0
0.029	0	0	0	0	0
0.03	0	0	0	0	0

z	C2H	C2H2	C2H3	C2H4	C2H5
0	0	0	0	0	0
0.001	0	0	0	0	0
0.01	0	0	0	0	0
0.02	0	0	0	0	0
0.029	0	0	0	0	0
0.03	0	0	0	0	0

z	C2H6	HCCO	CH2CO	HCCOH	N
0	0	0	0	0	0
0.001	0	0	0	0	0
0.01	0	0	0	0	0
0.02	0	0	0	0	0
0.029	0	0	0	0	0
0.03	0	0	0	0	0

z	NH	NH2	NH3	NNH	NO
0	0	0	0	0	0
0.001	0	0	0	0	0
0.01	0	0	0	0	0
0.02	0	0	0	0	0
0.029	0	0	0	0	0
0.03	0	0	0	0	0

z	NO2	N2O	HNO	CN	HCN
0	0	0	0	0	0
0.001	0	0	0	0	0
0.01	0	0	0	0	0
0.02	0	0	0	0	0
0.029	0	0	0	0	0

```
       0.03           0           0           0           0           0

----------------------------------------------------------------------------
         z         H2CN        HCNN        HCNO        HOCN        HNCO
----------------------------------------------------------------------------
         0           0           0           0           0           0
     0.001           0           0           0           0           0
      0.01           0           0           0           0           0
      0.02           0           0           0           0           0
     0.029           0           0           0           0           0
      0.03           0           0           0           0           0

----------------------------------------------------------------------------
         z          NCO          N2          AR        C3H7        C3H8
----------------------------------------------------------------------------
         0           0           0           0           0           0
     0.001           0           0           0           0           0
      0.01           0           0           0           0           0
      0.02           0           0           0           0           0
     0.029           0           0           0           0           0
      0.03           0           0           0           0           0

----------------------------------------------------------------------------
         z       CH2CHO      CH3CHO
----------------------------------------------------------------------------
         0           0           0
     0.001           0           0
      0.01           0           0
      0.02           0           0
     0.029           0           0
      0.03           0           0


>>>>>>>>>>>>>>>>>>>>>>>>>>>>>>>> outlet <<<<<<<<<<<<<<<<<<<<<<<<<<<<<<<<

----------------------------------------------------------------------------
         z    outlet dummy
----------------------------------------------------------------------------
         0           0
T in between 300 and 620.921
............................................................................

Attempt Newton solution of steady-state problem...    failure.

............................................................................
Take 2 timesteps     1.125e-05      1.533
............................................................................

Attempt Newton solution of steady-state problem...    failure.

............................................................................
Take 5 timesteps     4.271e-05        1.5
............................................................................

Attempt Newton solution of steady-state problem...    failure.

............................................................................
Take 10 timesteps      0.001232      0.347
............................................................................

Attempt Newton solution of steady-state problem...    success.

Problem solved on [7] point grid(s).

############################################################################
Refining grid in flame.
    New points inserted after grid points 1 3
    to resolve point 1 point 3
............................................................................

Attempt Newton solution of steady-state problem...    success.

Problem solved on [9] point grid(s).

no new points needed in flame
Solution saved to file ch4_adiabatic.xml as solution no_energy_18.
............................................................................

Attempt Newton solution of steady-state problem...    failure.

............................................................................
Take 2 timesteps      2.25e-05      5.706
............................................................................

Attempt Newton solution of steady-state problem...    failure.
```

```
.....................................................................
Take 5 timesteps     8.543e-05      5.547
.....................................................................

Attempt Newton solution of steady-state problem...    failure.

.....................................................................
Take 10 timesteps      0.002463      4.628
.....................................................................

Attempt Newton solution of steady-state problem...    success.

Problem solved on [9] point grid(s).

#########################################################################
Refining grid in flame.
    New points inserted after grid points 1 2 3 4 5 6
    to resolve C2H2 C2H4 C2H5 C2H6 C3H8 CH CH2 CH2(S) CH2CO CH2O CH2OH CH3 CH3CHO CH3O CH3OH CH4 CO CO2 H H2 H2O
     H2O2 HCN HCNO HCO HNCO HNO HO2 HOCN N N2O NCO NH2 NH3 NO NO2 O O2 OH T point 1 point 2 point 4 point 6 u
.....................................................................

Attempt Newton solution of steady-state problem...    failure.

.....................................................................
Take 2 timesteps     2.165e-05      5.784
.....................................................................

Attempt Newton solution of steady-state problem...    failure.

.....................................................................
Take 5 timesteps      8.22e-05      5.275
.....................................................................

Attempt Newton solution of steady-state problem...    failure.

.....................................................................
Take 10 timesteps     9.258e-06      6.442
.....................................................................

Attempt Newton solution of steady-state problem...    success.

Problem solved on [15] point grid(s).

#########################################################################
Refining grid in flame.
    New points inserted after grid points 3 4 5 6 7 8 9 11 12
    to resolve C C2H2 C2H4 C2H5 C2H6 C3H8 CH CH2 CH2(S) CH2CHO CH2CO CH2O CH2OH CH3 CH3CHO CH3O CH3OH CH4 CO CO2 H
    H2 H2O H2O2 HCCO HCN HCNO HCO HNCO HO2 N N2O NCO NH2 NH3 NO NO2 O O2 OH T point 12 point 4 point 7 u
.....................................................................

Attempt Newton solution of steady-state problem...    failure.

.....................................................................
Take 2 timesteps     1.041e-05      6.193
.....................................................................

Attempt Newton solution of steady-state problem...    failure.

.....................................................................
Take 5 timesteps     3.954e-05      5.503
.....................................................................

Attempt Newton solution of steady-state problem...    failure.

.....................................................................
Take 10 timesteps     8.907e-06      6.212
.....................................................................

Attempt Newton solution of steady-state problem...    success.

Problem solved on [24] point grid(s).

#########################################################################
Refining grid in flame.
    New points inserted after grid points 4 5 6 7 8 9 10 11 12 13
    to resolve C C2H2 C2H3 C2H4 C2H5 C2H6 C3H7 C3H8 CH CH2 CH2(S) CH2CHO CH2CO CH2O CH2OH CH3 CH3CHO CH3O CH3OH
    CH4 CO CO2 H H2 H2O H2O2 HCCO HCCOH HCN HCNO HCO HNCO HO2 N N2O NCO NO NO2 O O2 OH T point 11 point 6 u
.....................................................................

Attempt Newton solution of steady-state problem...    failure.

.....................................................................
Take 2 timesteps     1.002e-05      6.381
.....................................................................

Attempt Newton solution of steady-state problem...    failure.
```

```
.....................................................................
Take 5 timesteps     1.902e-05      6.426
.....................................................................

Attempt Newton solution of steady-state problem...    failure.

.....................................................................
Take 10 timesteps     6.856e-05      5.702
.....................................................................

Attempt Newton solution of steady-state problem...    success.

Problem solved on [34] point grid(s).

#####################################################################
Refining grid in flame.
    New points inserted after grid points 7 8 9 10 11 12 13 14 15 16 17 18 19 20 21
    to resolve C C2H C2H2 C2H3 C2H4 C2H5 C2H6 C3H7 C3H8 CH CH2 CH2(S) CH2CHO CH2CO CH2O CH2OH CH3 CH3CHO CH3O
    CH3OH CH4 CO CO2 H H2 H2O H2O2 HCCO HCCOH HCN HCNO HCO HNCO HO2 N N2O NCO NH3 NO NO2 O O2 OH T point 18 point 9 u
.....................................................................

Attempt Newton solution of steady-state problem...    failure.

.....................................................................
Take 2 timesteps     3.857e-05      6.464
.....................................................................

Attempt Newton solution of steady-state problem...    failure.

.....................................................................
Take 5 timesteps     3.661e-05      6.227
.....................................................................

Attempt Newton solution of steady-state problem...    failure.

.....................................................................
Take 10 timesteps     6.597e-05      6.064
.....................................................................

Attempt Newton solution of steady-state problem...    failure.

.....................................................................
Take 20 timesteps       0.07312      1.657
.....................................................................

Attempt Newton solution of steady-state problem...    success.

Problem solved on [49] point grid(s).

#####################################################################
Refining grid in flame.
    New points inserted after grid points 11 12 13 14 15 16 17 18 19 20 21 22 23 24 25 26 27 29 30 31
    to resolve C C2H C2H2 C2H3 C2H4 C2H5 C2H6 C3H7 C3H8 CH CH2 CH2(S) CH2CHO CH2CO CH2O CH2OH CH3 CH3CHO CH3O
    CH3OH CH4 CO H H2 H2O H2O2 HCCO HCCOH HCN HCNO HCO HNCO HO2 N NCO NO2 O OH T point 12 point 29 u
.....................................................................

Attempt Newton solution of steady-state problem...    success.

Problem solved on [69] point grid(s).

#####################################################################
Refining grid in flame.
    New points inserted after grid points 12 13 14 15 16 18 19 20 21 22 23 24 25 26 27 28 29 30 31 32 33 34 35 36 37 38 39 40 46 47
    to resolve C C2H C2H2 C2H3 C2H4 C2H5 C2H6 C3H7 C3H8 CH CH2 CH2(S) CH2CHO CH2CO CH2O CH2OH CH3 CH3CHO CH3O
    CH3OH CH4 H H2 H2O H2O2 HCCO HCCOH HCO HO2 NO2 O point 14 point 46
.....................................................................

Attempt Newton solution of steady-state problem...    success.

Problem solved on [99] point grid(s).

#####################################################################
Refining grid in flame.
    New points inserted after grid points 14 15 16 17 22 41 42 43 44 45 46 47 48 49 50 51 52 54 55
    to resolve C C2H3 C2H5 C2H6 C3H8 CH CH2 CH2CHO CH2O CH3O CH3OH H2O2 HO2 NO2 point 17
.....................................................................

Attempt Newton solution of steady-state problem...    success.

Problem solved on [118] point grid(s).

#####################################################################
Refining grid in flame.
    New points inserted after grid points 17 18 19 20 21 45 70
    to resolve C2H3 C3H8 CH2O CH3O CH3OH H2O2 HO2 NO2 point 21
.....................................................................
```

```
Attempt Newton solution of steady-state problem...    success.

Problem solved on [125] point grid(s).

################################################################################
Refining grid in flame.
    New points inserted after grid points 23 24 25 26
    to resolve CH3O
................................................................................

Attempt Newton solution of steady-state problem...    success.

Problem solved on [129] point grid(s).

no new points needed in flame
Solution saved to file ch4_adiabatic.xml as solution energy_10.
mixture-averaged flamespeed =  0.382110961502
................................................................................

Attempt Newton solution of steady-state problem...    failure.

................................................................................
Take 2 timesteps     3.516e-07      5.713
................................................................................

Attempt Newton solution of steady-state problem...    failure.

................................................................................
Take 5 timesteps     1.669e-07      5.671
................................................................................

Attempt Newton solution of steady-state problem...    success.

Problem solved on [129] point grid(s).

no new points needed in flame
Solution saved to file ch4_adiabatic.xml as solution energy_multi_9.
solution saved to adiabatic_flame.csv
multicomponent flamespeed =  0.386887308628

Statistics:

 Grid   Functions   Time      Jacobians   Time
    9     370       0.1766        9       0.2925
   11      70       0.0455        2       0.0907
   11     722       0.4999       11       0.5135
   17     992       1.2196       26       2.2466
   26    1274       2.5922       20       2.9329
   36     882       2.5941       13       2.7890
   51    1262       5.4696       24       7.6754
   71      42       0.2573        1       0.4593
  101      22       0.1935        1       0.6794
  120      16       0.1680        1       0.8235
  127      14       0.1559        1       0.8827
  131      12       0.1381        1       0.9131
  131     441     140.0337       20      18.5154
```

VITA

Nathan Harlan Jones was born in Baytown, Texas, and spent his childhood in Dayton, Texas. He attended Texas A&M University where he completed his Bachelor of Science degree in Aerospace Engineering in 2010. He went on to attend graduate school at A&M and earned his Master of Science degree in Aerospace Engineering in 2012. After graduation Nathan began working in the propulsion group for Navair at Patuxent River. He can be reached via email at njones1719@gmail.com, or by mail at 3141 TAMU, College Station, TX, 77843-3141.

The typist for this thesis was Nathan Harlan Jones.